Study of Heavy Ion Beam Interaction with High Energy Laser Produced Plasmas

Schwerionen-Wechselwirkung mit Hochenergielaser-erzeugten Plasmen
Zur Erlangung des Grades eines Doktors der Naturwissenschaften (Dr. rer. nat.)
genehmigte Dissertation von M.Phil.-Phys. Muhammad Imran aus Hafizabad (Pakistan)
Februar 2011 — Darmstadt — D 17

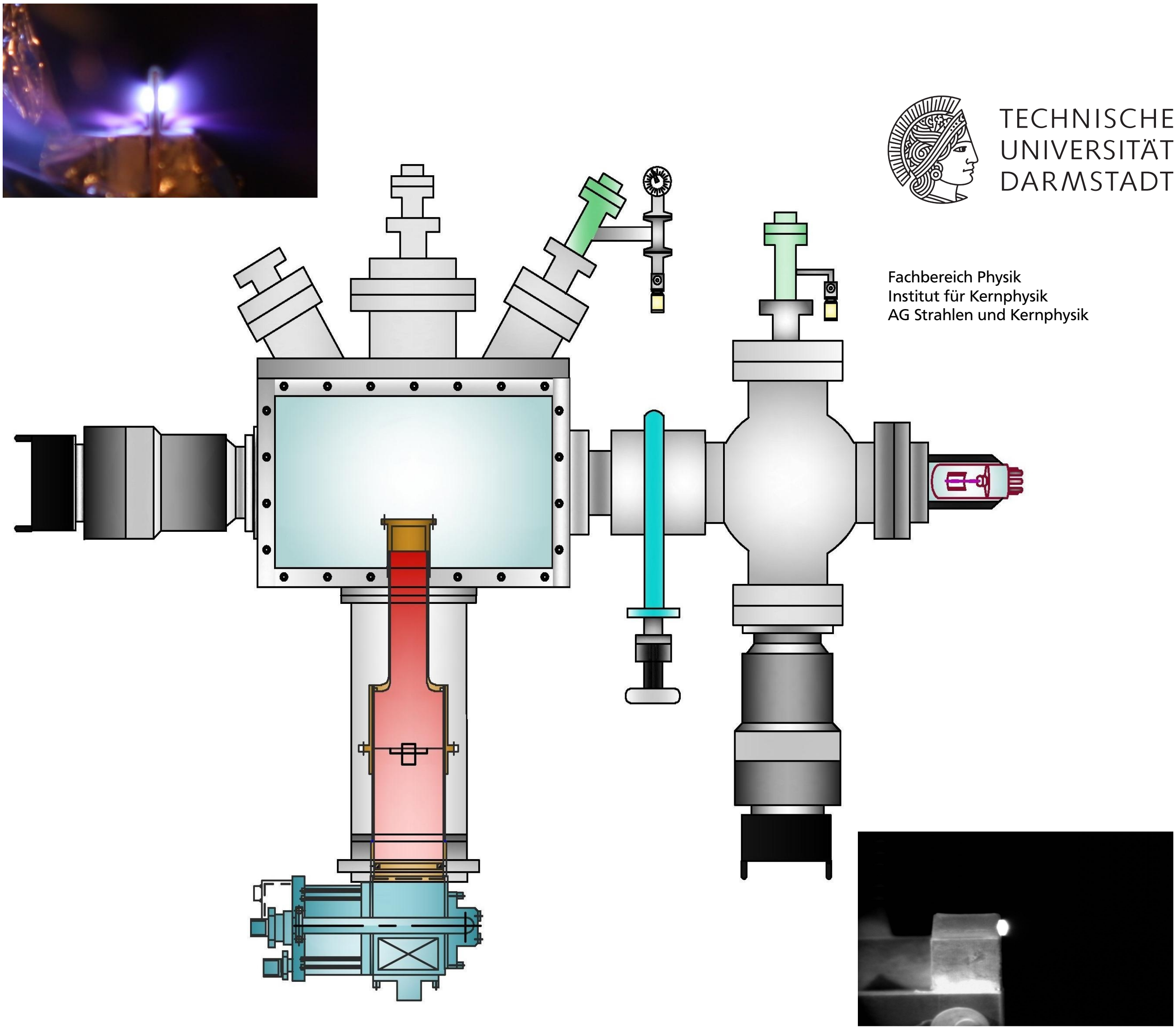

TECHNISCHE
UNIVERSITÄT
DARMSTADT

Fachbereich Physik
Institut für Kernphysik
AG Strahlen und Kernphysik

Study of Heavy Ion Beam Interaction with High Energy Laser Produced Plasmas
Schwerionen-Wechselwirkung mit Hochenergielaser-erzeugten Plasmen

Genehmigte Dissertation von M.Phil.-Phys. Muhammad Imran aus Hafizabad (Pakistan)

1. Gutachten: Prof. Dr. Dr. h.c./RUS Dieter H. H. Hoffmann
2. Gutachten: Prof. Dr. Norbert Pietralla

Tag der Einreichung: 10.12.2010
Tag der Prüfung: 18.02.2011

Darmstadt — D 17

Zusammenfassung

Tieftemperatur-Festkörper-Targets aus Edelgasen sowie Stickstoff und Deuterium wurden für die Messung des Energieverlustes schwerer Ionen in dichten, lasererzeugten Plasmen entwickelt. Frei-stehende Targets einer Dicke von 1 cm bis 1 mm und ebene Folien-Targets der Dicke von einigen Hundert Mikrometer wurde produziert, wobei austauschbare, aus einer gewissen Entfernung kontrollierbare Zuchtkammern eingesetzt wurden. Die Geometrie der Targets wird dabei durch die Geometrie der Zuchtkammern bestimmt. Darüber hinaus wurde bei der Konstruktion von transportierbaren kryogenen Systemen mitgewirkt, die zur Herstellung von Edelgas-, Stickstoff- und Deuteriumkristallen eingesetzt werden.

Die ersten Laserplasmaexperimente wurden durchgeführt, indem frei stehende kubische Stickstofftargets mit dem *nhelix*-Laser bestrahlt wurden. Mittels Interferometrie wurden Elektronendichten der Größenordnung von 10^{19} cm^{-3} festgestellt. Weitere Experimente wurden mit dünnen Deuterium-Folien durchgeführt. Die Targetfolien wurden von zwei Seiten aus bestrahlt, von einer mit dem *nhelix*- und von der anderem mit dem PHELIX-Laser-System. Der Ionenstrahl vom UNILAC wurde zur Untersuchung der Wechselwirkung herangezogen. Für das Deuteriumplasma und das Stickstoffplasma wurden ähnliche Elektronendichten festgestellt. Die Resultate der Experimente tragen dazu bei, dass in Zukunft am Z6 Strahl-Plasma-Wechselwirkungsexperimente mit Tieftemperatur-Targets durchgeführt werden können.

Bei den Experimenten befördern die Projektile des Ionenstrahls mittels Coulomb-Wechselwirkung Impuls und Energie zu den Targetteilchen. Damit hängt der Energieverlust der Projektile auch von der Ionisationsenergie der Targets ab. Die Ionisationsenergie von Targetteilchen in Plasmen ist von Temperatur und Dichte des Plasmas abhängig. Mit zunehmender Plasmadichte und/oder -temperatur nimmt die Ionisationsenergie ab. Dieses Verhalten wurde bereits von verschiedenen Autoren theoretisch nachgewiesen. Die entsprechend abgeleiteten theoretischen Formeln beschreiben die Variationen der Ionisationsenergie aber noch recht ungenau. Deshalb wird in der vorliegenden Arbeit versucht, zu einer genaueren Berechnung der Erniedrigung der Ionisationsenergie wasserstoffähnlicher Bindungszustände in dichten Plasmen beizutragen.

Dazu wird eine Jacobi-Padé-Approximation von Ebeling, Bornath und Kraeft für die Verschiebungen der Energieniveaus wasserstoffähnlichen Kohlenstoffs ausgewertet. Die relativen Shifts der verschiedenen Energieniveaus des fünffach geladenen Kohlenstoffions sind dabei durch die Differenz zwischen Coulomb- und Debye-Potential und durch die kinetische Energie der Teilchen bestimmt. Die Verschiebung der Energieniveaus infolge der kinetischen Energie wird im Impulsraum beschrieben, so dass neunfache Integrale im Phasenraum zu berechnen sind. Frühere quantenphysikalische Berechnungen der Energieverschiebungen wurden nur für Energieniveaus mit der Nebenquantenzahl null durchgeführt. Hier wird detailliert dargestellt, wie man diese Rechnungen für beliebige Nebenquantenzahlen erweitern kann. Diese Herangehensweise ist auch für in Zukunft verbesserte Padé-Approximationen einsetzbar. Die numerischen Resultate für die relativen Verschiebungen der Energieniveaus der fünffach geladenen Kohlenstoffionen werden als Funktion des Mott-Parameters des Plasmas dargestellt. Die Abhängigkeit der Verschiebungen von den Haupt- und Nebenquantenzahlen wird diskutiert.

Abstract

Cryogenic solid-state targets of rare gases as well as nitrogen and deuterium have been developed for the measurements of the energy loss of heavy ions in dense, laser produced plasmas. Free-standing targets with a thickness of 1 cm to 1 mm and planar foil-supported targets with a thickness of few hundred of microns have been produced using interchangeable, remotely controlled target growing chambers. The geometry of the targets is determined by the geometry of the growing chamber. In addition to this, work has been contributed to the construction of the portable cryogenic system used for growing the rare gas, nitrogen and deuterium crystals.

The first laser plasma experiments were performed by irradiating free standing cubic nitrogen targets with the *nhelix* laser. Interferometric measurements revealed the electron density of the order of $10^{19}\,\mathrm{cm}^{-3}$. Additional experiments have been performed with thin foil-supported deuterium targets. The target foil was irradiated from both sides using the *nhelix* and PHELIX laser systems while the ion beam from UNILAC was used to study the interaction. The electron density values obtained for deuterium plasmas are similar to those for nitrogen plasmas. The outcome of these experiments paves the way to realize beam-plasma interaction experiments at Z6, employing cryogenic targets.

The projectiles of an ion beam transfer momentum and energy to the target particles by Coulomb interactions. The energy loss of the projectiles is therefore also dependent on the ionization energy of the targets. In plasmas the ionization energy of the target particles is determined by its temperature and density. With increasing plasma temperatures and pressures, one obtains a lowering of the ionization energy. This fact has already been established by several authors, however up to now the resulting approximations were too rough. Thus in the present work it is attempted to contribute to a more careful recalculation of the lowering of the ionization energy of dense hydrogen-like bound states.

For this purpose the Jacobi-Padé approximation of relative energy level shifts is applied. There the relative energy level shift of the five-fold ionized carbon is determined by the difference between Coulomb and Debye potential and by the kinetic energy of the particles. The shift caused by the kinetic energy has to be found considering the momentum space of the particles, so that nine-fold integrals in phase space have to be calculated. Quantum physically, former numerical calculations for the energy shift were only performed for particle states with zero angular momentum quantum numbers. Presently, a detailed, to a large extent analytical analysis of the shift caused by kinetic energy is given for any angular momentum quantum number enabling also an improved analysis of in future developed Jacobi-Padé formulae. The relative energy shifts of the bound-states of the five-fold ionized carbon are numerically obtained as function of the Mott parameter of the plasma. Dependencies of the shifts on main quantum numbers and orbital angular momentum quantum numbers are also discussed.

Contents

List of Figures

List of Tables

1 Introduction

The environment we live in, the Earth and everything on it, the Sun and all the stars are made from the familiar and pervasive baryonic matter. The natural elements range all the way from hydrogen to the heaviest plutonium such that almost all their mass resides in the baryons, the electron being negligible in comparison [1]. Most of the matter in the universe, however, occurs predominantly in the form of dark matter or dark energy whose nature remains a mystery [2]. The baryonic matter comprises only 4 per cent of the total mass of the universe and this matter is mainly found in the plasma state. A plasma may be defined as a conglomeration of ions, free electrons and - depending on the degree of ionization - neutral atoms, with their own respective densities, temperatures and velocities. The interior of stars, interstellar and interplanetary space even the interior of planets exist in the form of plasmas. Extremes of temperature and pressure that exist e.g. inside the stars are a subject of high energy density (HED) science. Matter exists in the form of dense strongly coupled plasmas where the long-range Coulomb force is the factor that determines the statistical properties of such states [3].

Compression and heating of matter to high energy density states are enabled by modern laser and particle beam systems. High-power laser systems, for instance, prevail laboratory investigations of extreme states of matter, with major applications in stellar astrophysics [4] and fusion energy research [5]. Highly energetic, well focused intense particle beams offer a variety of schemes to study high energy density matter. The proposed **LA**boratory **PLA**netary **S**cience (LAPLAS) experimental scheme, for instance, is intended for studies of the low-entropy compression of a material such as frozen hydrogen or ice that is enclosed in a cylindrical shell of a high-Z material [6]. Moreover, ultrafast proton beam [7], X-ray [8] and shock wave heating [9] are amongst other established methods for volumetric heating. Such experiments require rapid and uniform deposition of energy throughout the material which certainly poses many challenges.

Heating of matter with intense ion beams requires a basic understanding of energy deposition processes of ions in matter [3]. During the heating process the material changes from solid to liquid and gas and eventually to dense ionized matter. However, when matter undergoes the transition to plasma or even to a dense strongly-coupled plasma there are only few experimental data to benchmark theoretical models. Since the interaction is mediated by the well known Coulomb force, collective phenomena of beam-target coupling lead to surprising results, for example, the high energy loss of ions in dense ionized matter.

Energy loss measurements date back to the pioneering works of Bohr [10], Bethe [11] and Bloch [12]. The interaction of charged particles with cold matter is well known, however the interaction of charged particles with ionized matter is not yet fully understood. The accelerator facilities as well as two high energy laser systems at the GSI Helmholtzzentrum für Schwerionenforschung GmbH (GSI) Darmstadt are well suited for beam-plasma, and beam-matter interaction experiments [13]. Several experiments have been conducted for energy loss measurements during the last two decades. Recent measurements involving laser-generated carbon plasmas [14] have covered huge parameter ranges in density and temperature. Indirectly heated hohlraum targets have also been used to avoid detrimental effects like gradients in plasma density and temperature. Cryogenic targets of rare gas as well as thin films of deuterium have also been recently developed and manipulated at the Z6 experimental area where the first beam plasma experiments have been performed. The significant benefit of cryogenic solid targets is the generation of homogeneous hot dense plasmas of substances which under normal conditions exist in gaseous state. However their development is demanding, particularly in the case of hydrogen which freezes below 13 K. Part of the present work has been devoted to participate the development and commissioning of the cryogenic target system at the Z6 experimental area.

Considering the interaction of ion beams with matter, and in high-energy ion-beam experiments the interaction of the beams with the target material, the excitation of the target electrons and the ionization of the target matter are of large importance. The projectiles transfer momentum and energy to the target particles by Coulomb interaction. Thus, the energy loss of the projectile also depends on the ionization energy of the targets.

The ionization energy of a target particle, that means the work necessary to strip an electron from the target particle, depends on the density and temperature of the plasma. With increasing plasma temperature and pressure, one obtains a lowering of the ionization energy. This lowering was already intensively investigated by many authors [15, 16, 17, 18, 19, 20, 21, 22] using quantum physics and performing Jacobi-Padé approximations. The plasma considered was especially the hydrogen one, but some studies were also made for hydrogen-like systems consisting, for instance, of bound-states of one-fold ionized helium atoms and five-fold ionized carbon atoms [17]. Such matter made up of protons, alpha particles and ionized carbon plays an important role in astrophysics. In the present work it is attempted to estimate modifications of the energy shifts of hydrogen-like ions in carbon plasmas with densities of the order of $10^{27} - 10^{29}$ m^{-3} at a temperature of 10^5 K due to screening and quantum physical effects.

In chapter 2, theoretical fundamentals relevant to the experimental part will be described. The accelerator and lasers facilities at GSI as well as experimental setup for energy loss experiments will be discussed in chapter 3. Next, a brief description of the development of cryogenic targets will be given, which will be followed by experimental results and discussions. In chapter 6, basic ideas on the energy shifts in dense matter and the results of analytic and numeric calculations will be presented. Finally a brief outlook and possible improvements will be given.

2 Theoretical Background

In this chapter, the theoretical background relevant to the experiments carried out within the scope of the present thesis is described. For the experimental work involving laser-generated plasmas knowledge of both laser and plasma physics is necessary. Therefore starting from a few fundamental definitions of plasma phenomena and parameters, the interaction of high power lasers with matter leading to a plasma generation has been discussed. The most important and interesting features of laser produced plasmas result from laser-plasma interaction and therefore discussed in this chapter. Basics of beam-plasma interactions, particularly energy loss phenomena, are also a part of this chapter. Finally, a brief description of interferometry and fabrication of cryogenic targets is given.

2.1 Basic properties of plasma

At temperatures near or exceeding atomic ionization energies, atoms decompose into negatively charged electrons and positively charged ions. These charged particles are by no means free: in fact, they are strongly affected by each others electromagnetic fields. Nevertheless, because the charges are no longer bound, their assemblage becomes capable of collective motions of great vigour and complexity. Such an assemblage is termed a *plasma*.

There are several theoretical approaches to describe a plasma. A common approach is to treat the plasma as a mixture of electrons and ions, which possess their own densities, temperatures and velocities. In order to characterize a plasma several properties and parameters must be known. The following sections describe some key concepts about plasmas.

2.1.1 Quasi-neutrality

A plasma consists of charged particles (electrons, ions). Nevertheless, one may assume a plasma to be neutral since it maintains an almost perfect charge balance.

$$-q_e n_e = q_i n_i \pm \Delta \tag{2.1}$$

where Δ is tiny.
Therefore, it is ‘quasi-neutral’: to an outside observer there is no net charge.

2.1.2 Dynamical screening and the Debye length

A charged particle in a plasma does not interact merely with a few neighbours but with a large number of surrounding particles. The result is the collective behaviour of the particles in the plasma. The collective behaviour leads to physical effects such as the dynamical screening of the Coulomb potential. The Coulomb force has a finite range and there exists a modified Coulomb potential called the Debye potential,

$$\Phi(r) = \frac{q}{4\pi r} e^{-\frac{r}{r_D}} . \tag{2.2}$$

The screened field $\Phi(r)$ is of short range. The range of the potential is given by the screening radius r_D and is called the Debye radius.

$$r_D = \sqrt{\frac{k_B T}{4\pi n_e e^2}} . \tag{2.3}$$

For distances smaller than r_D, the screened potential is a Coulomb-like potential whereas for larger distances the potential decreases exponentially. This screening effect is an important and fundamental property of a many-particle system with Coulomb interactions.

2.1.3 Local thermodynamic equilibrium

Since an actual plasma does not exhibit a homogeneous distribution of its properties, for instance in temperature and density, equilibrium considerations can only be applied locally. For this reason the concept of Local Thermodynamic Equilibrium (LTE) was introduced. LTE requires that collision processes govern transitions and reactions in the plasma and that there is a micro-reversibility among the collision processes. In other words, an equilibrium of each collision process with its reverse process is required.

LTE requires further that local gradients of the plasma properties (temperature, density, heat conductivity etc.) are sufficiently small so that a given particle which diffuses from one location to another in plasma finds sufficient time to equilibrate i.e. the diffusion time should be of the same order of magnitude as the equilibrium time.

2.1.4 Plasma frequency

The plasma frequency arises as a basic consequence of the restoring Coulomb interaction between oppositely charged particles. If the free electrons in a plasma are displaced with respect to the ions, the space charge will lead to a restoring force. This force acts on electrons, as the ion mass is much larger than the electron mass, the ions can safely be assumed to be stationary, while the electron begin to oscillate with a characteristic frequency, the plasma frequency ω_p:

$$\omega_p = \sqrt{\frac{n_e e^2}{\varepsilon_0 m_e}} . \tag{2.4}$$

Here e is the electron charge, n_e- the free electron density and m_e- the electron mass. The plasma frequency is very important regarding laser-plasma interactions.

2.2 Laser produced plasmas

When a high-intensity laser pulse ($> 10^{10}\,\mathrm{Wcm^{-2}}$) strikes a solid target, a characteristic sequence of energy conversion processes leads to the production of a hot, dense plasma consisting of matter in an extreme state of high energy concentration [23]. The intensity threshold is dependent on the wavelength of the laser and the properties of the target material [24]. As a rule, the thresholds decrease with increasing laser wavelength and pulse duration [25, 26]. The photon energy of a laser is generally too low to ionize matter directly. Ionization occurs instead by collisions of fast electrons and by multi-photon and field ionization. The electron heating and subsequent thermal ionization can work only if few electrons in the region of laser intensity are present. It is most likely, that due to background radiation or impurity effects free electrons are there, however untill now there exits no precise answer to the question [27].

Laser plasmas mainly involve two stages for their generation. First, the laser interacts with solid matter and creates a plasma. Then the laser interacts with the newly created plasma for the remaining duration of the laser pulse. For laser pulses of nanosecond duration, a plasma layer is formed in front of the target in a time of the order of a few tens of ps, so that most of the laser energy is absorbed by this plasma which rapidly heats up and expands.

2.3 Laser-plasma interaction

In view of many important applications the generation of homogeneous high density and, at the same time, very hot plasmas is required. However, for an infrared laser, direct interaction of the laser beam with matter is possible only below a limiting density, the so-called critical density.
An expression for the critical density is given by [28]

$$n_c = \frac{\pi m_e c^2}{e^2}\frac{1}{\lambda_L^2} = \frac{1.1\times 10^{21}}{\lambda_L^2}\,\mathrm{cm}^{-3}. \tag{2.5}$$

It strongly depends upon the laser wavelength $\lambda_L(\,\mu\mathrm{m})$. The light can travel through the ablating plasma upto n_c, where laser frquency ω_L equals ω_p. For a wavelength of 1064 nm the critical density is $1.021\times 10^{21}\,\mathrm{cm}^{-3}$. Three different zones as shown in figure 2.1 can be defined to characterize laser induced plasmas.

The thin, hot area on the side of the hot laser is called corona. The density is just below the critical density and so the laser radiation can penetrate and heat this region. The corona has a high temperature and low density. The transfer of laser energy to the plasma in this area occurs mostly in the form of collisional absorption.

The critical surface divides the corona from the diffusion zone. On this surface the free electron density is so high that the laser light can no longer penetrate in the plasma . It is reflected at the critical surface. In the diffusion zone, the energy transport is done by diffusion of electrons

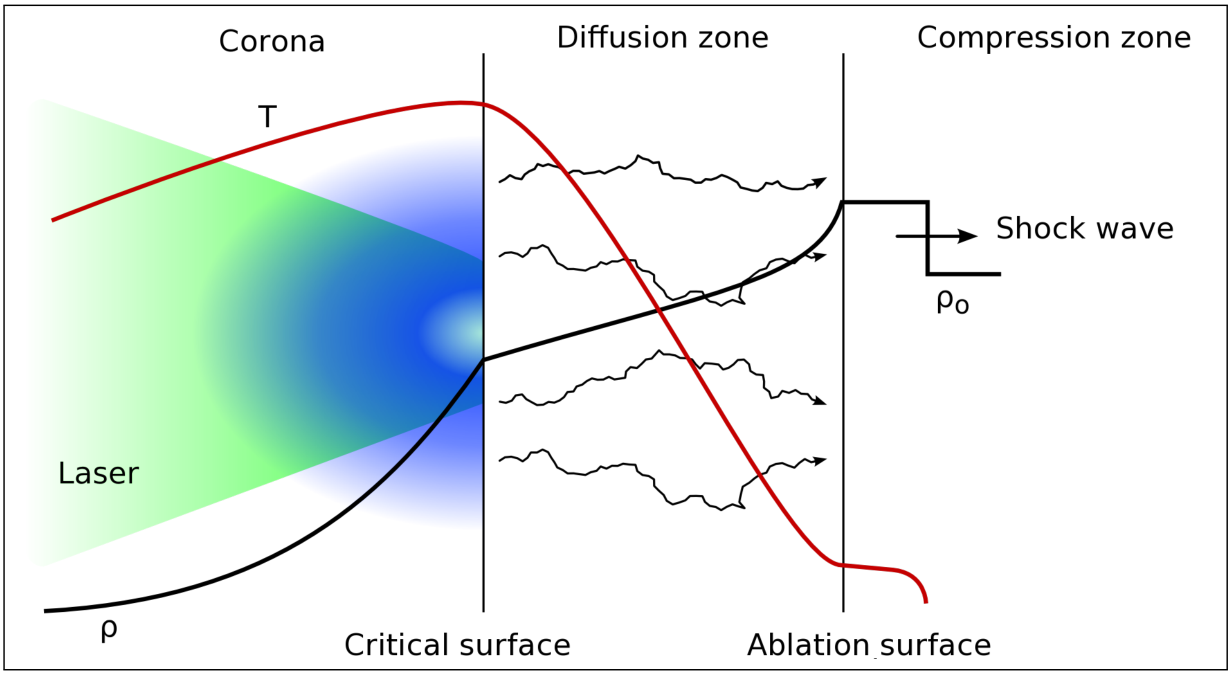

Figure 2.1: Schematic description of the characteristic regions of a laser produced plasma [29].

and radiation transport. In the case of LTE a thin plasma layer expands from the surface of the solid with the speed of sound c_S in the space

$$c_S = \sqrt{\frac{Zk_B T_e}{M_i}} \,. \tag{2.6}$$

Here Z is the ionization of the plasma, k_B is the Boltzmann constant, T_e is the electron temperature and M_i is the ion mass. The ablation at the solid surface generates a shock wave that runs in the solid. This area is therefore known as a compression zone.

2.4 Absorption of the laser energy in a plasma

The coupling of intense laser light with plasma is determined by several different processes. These processes range from collisional absorption to the excitation of numerous laser-driven instabilities. The absorption efficiency, the location of the energy deposition and character of heated-particle distribution functions depends on the mix of these coupling processes. In turn, the mix depends on the intensity, wavelength, pulse length and coherence properties of the incident laser light and on the size and composition of the plasma.

The intensity of the laser systems used for the present experiments ranges within 5×10^{11} Wcm^{-2} at a wavelength of 1064 nm (*nhelix*) as well as 1053 nm (PHELIX). The pulse duration is 10 ns FWHM (Full Width at Half Maximum). For such an intensity level of the lasers, primarily the collisional absorption and the resonance absorption are responsible for the energy transfer of light in a plasma.

2.4.1 Collisional absorption (inverse bremsstrahlung)

Collisional absorption or inverse bremsstrahlung is the optimum coupling mechanism for driving matter ablatively with laser beams. In this process, electrons oscillating in the electric field of the laser are randomly scattered by the ions. Coherent energy of oscillation is thereby converted into random thermal energy. The heating rate is simply the oscillatory energy times the electron-ion collision frequency which depends on ion density, electron temperature and ionization scale of the plasma.

$$\nu_{ei} = \frac{4\sqrt{2\pi}}{3} \frac{Z^2 e^4 n_i \ln\Lambda}{m_e^{1/2}(k_B T_e)^{3/2}} \tag{2.7}$$

where $\ln\Lambda$ is the Coulomb-logarithm for the electron ion collision. The coefficient of collisional absorption is given by

$$K_{IB} = \frac{\nu_{ei}}{c}\left(\frac{n_e}{n_c}\right)^2\left(1-\frac{n_e}{n_c}\right)^{-1/2} \quad \propto \quad \frac{Zn_e^2}{T_e^{3/2}}\left(1-\frac{n_e}{n_c}\right)^{-1/2} \tag{2.8}$$

This expression shows that inverse bremsstrahlung is efficient in high density and low temperature regions. The fraction of the laser energy absorbed through this mechanism during the propagation upto the critical density strongly depends on the electron density profile.

2.4.2 Plasma waves

Langmuir waves

Langmuir waves are electron density waves in which electrons oscillate about their equilibrium distribution. These are high-frequency waves close to the plasma frequency ω_p, such that the massive ions can be considered as a fixed neutralizing background. These waves only exist for phase velocities much larger than the electron thermal velocity, otherwise they are suppressed by *Landau damping* [30]. The dispersion relation is given by

$$\omega^2 = \omega_p^2\left(1 + 3k^2\lambda_D^2\right) \tag{2.9}$$

Ion-acoustic waves

A second important type of plasma waves are ion-acoustic waves. These are sound waves, which occur in plasma at frequency much below ω_p and involve ion motion. Actually the electrons can follow the ions in this mode, such that quasi-neutrality is preserved. The dispersion relation is given by

$$\omega = kc_s \tag{2.10}$$

where c_s is the ion-acoustic sound velocity.

2.4.3 Resonance absorption and parametric instabilities

As the electron temperature increases Coulomb collisions become less effective and, in the absence of conversion process other than collisional absorption, a plasma becomes highly transparent to the laser radiation when the electron density n_e is below its critical value n_c; in the opposite of the existence of an overdense layer, i.e. $n_e > n_c$ the laser plasma behaves highly reflecting. There is, however, another effective collisionless absorption process at oblique incidence of radiations which consists in the resonant conversion of laser light into an electron plasma wave of the same frequency ω.

Resonance absorption is a two wave process. For this conversion to take place a resonance condition for the frequencies as well as for the wavelengths must be fulfilled. Owing to very different values of the light and electron sound speeds at non relativistic temperatures, conversion take place only in a very restricted region around the critical point since both wave vectors become zero there. The electromagnetic field acts as a resonant driver for the electron plasma wave propagating down the density gradient and is dependent on the angle of incidence. In a plasma with linear density profile, the efficiency of the resonance absorption depends on a single parameter τ given by [23]

$$\tau = \left(\frac{\omega_0 L}{c}\right)^{1/3} \sin\theta \tag{2.11}$$

where L is the density scale length.

An obvious prerequisite is that the electric field of the laser pulse has a component along the density gradient of the plasma (in this case the laser pulse is said to be p-polarized), so that, in principle, resonance absorption cannot occur when the laser is normally incident on the target surface. In equation (2.11), when $\theta = 0$ ($\tau = 0$ for normal incidence), there is no resonance absorption. For $\theta \neq 0$ but $\omega_0 L/c$ too large, very little field tunnels to the critical density surface. Resonance absorption is then correspondingly very small. At some intermediate angle, dependent on $\omega_0 L/c$, there is optimum absorption $f_a \sim 0.5$ for $\tau = 0.8$ [31].

Another way of coupling electromagnetic and electrostatic waves is by non-linear three-wave coupling. These processes represent the so-called *parametric instabilities*. In contrast to the resonance absorption they may occur in uniform plasma but only at high laser intensities, when the oscillating energy of the electrons in the light field becomes comparable to their thermal energy.

2.5 Beam-plasma interactions

At GSI first beam-plasma interaction experiments clearly demonstrated the fact that ion stopping in a plasma environment exceeds the stopping in cold matter mainly because free electrons in a plasma can absorb ion energy more easily than a deeply bound electrons [32, 33]. Experiments with laser produced plasmas [34] have also confirmed this effect at higher plasma density and temperature. The projectiles transfer energy and momentum to the target particles through Coulomb scattering. We consider here a fully ionized projectile of nuclear charge Z_p, moving with the speed v_p encounters an electron at rest. The momentum change is given by

$$\Delta\vec{p} = e\,.\int_{-\infty}^{+\infty} \mathrm{d}t\vec{E}(t) = Z_p e^2 \int_{-\infty}^{+\infty} \mathrm{d}t\frac{\vec{r}(t)}{r(t)^3} = \frac{2Z_p e^2}{b v_p}\vec{e_y}\,. \tag{2.12}$$

and for the energy change

$$\Delta E(b) = \frac{(\Delta\vec{p})^2}{2m_e} = \frac{2Z_2^2 e^4}{m_e v_p^2}\frac{1}{b^2}\,. \tag{2.13}$$

Here e is the elementary charge, m_e is the electron mass, $\vec{E_t}$ is the electric field, $\vec{r}(t)$ is the distance vector, b is the impact parameter and $\vec{e_y}$ is the direction of the momentum transfer. Summation of all possible impact parameter leads to the differential energy loss (−dE/dx). In an interval [b; b + db] along the differential path dx, the ion interacts with $2\pi b\,\mathrm{d}b\mathrm{d}x\;Z_T n_T$ target electrons. Here n_T is the particle number density of target atoms and Z_T for the atomic number in the target. It follows from equations (2.12) and (2.13):

$$S(x) = -\frac{\mathrm{d}E}{\mathrm{d}x} = \frac{4\pi Z_p^2 Z_T e^4}{m_e v_p^2}\,n_T \int_0^{\infty} \frac{\mathrm{d}b}{b} \tag{2.14}$$

The integration cannot be solved as it diverges at boundary limits. Therefore, it is necessary to shrink the integration limits . It follows,

$$S(x) \approx \frac{4\pi Z_p^2 Z_T e^4}{m_e v_p^2}\,n_T.L \tag{2.15}$$

where

$$L = \ln\frac{b_{max}}{b_{min}} \tag{2.16}$$

is defined as the Coulomb-logarithm.

One possibility for the assessment of the Coulomb logarithm is to consider that the energy transfer between ion and electron has a maximum for central collisions. According to the classical theory this cannot be greater than $\Delta E_{max} = 2m_e v_p^2$. Setting this into equation (2.13) follows:

$$b_{min} = \frac{Z_p e^2}{m_e v_p^2} \tag{2.17}$$

The minimum energy transfer can be estimated from the mean ionization potential of the target $\bar{I}_0$ [35]. It must also be valid that $\bar{I}_0 > 2Z_p e^2/b$. The mean ionization potential is an average over all possible energy transfer, weighted by their transition probability. It follows:

$$b_{max} = \frac{2Z_p e^2}{\bar{I}_0} \tag{2.18}$$

According to this approach the well-known Bethe formula [11] for the Coulomb-logarithm is given by

$$\ln \frac{b_{max}}{b_{min}} = \ln \frac{2m_e v_p^2}{\bar{I}} \tag{2.19}$$

The considerations here are related to the cold matter without free charge carriers. For a plasma, however, free electrons can not be neglected. Therefore an additional term due to the contribution of free electrons is included in the Bethe formula. According to [35] one can estimate b_{min} by the uncertainty relation:

$$b_{min} = \frac{\hbar}{2m_e v_p} \tag{2.20}$$

If the interaction time $\tau = b/v_p$ is greater than the period of oscillation $1/\omega_p$ of a free electron, no energy is transferred, therefore

$$b_{max} = \frac{v_p}{\omega_p} \tag{2.21}$$

It follows from these considerations that the differential energy loss in the plasma satisfies

$$-\frac{\mathrm{d}E}{\mathrm{d}x} = \frac{16\pi a_0^2 E_H^2 Z_p^2}{m_e v_p^2} \left[\underbrace{\sum_{Z=0}^{Z_K} (Z_K - Z) n_Z \ln\left(\frac{2m_e v_p^2}{\bar{I}_Z}\right)}_{\textit{bound electrons contribution}} + \underbrace{n_e \ln\left(\frac{2m_e v_p^2}{\hbar\omega_P}\right)}_{\textit{free electrons contribution}} \right] \tag{2.22}$$

Here a_0 is the Bohr radius, E_H the Rydberg energy, Z_K the nuclear charge, n_Z the density of the Z-fold charged ions with atomic number Z_k and the free electron density n_e. $\bar{I}_Z$ is the average ionization potential of the target ions. Using a logarithmic interpolation between $\bar{I}_Z$ and the value for hydrogen-like ions one may calculate $\bar{I}_{Z_{k-1}} = Z_K^2 \bar{I}_H$:

$$\ln \bar{I}_Z = \ln \bar{I}_0 + \frac{Z}{Z_K - 1} \ln \frac{Z_K^2 \bar{I}_H}{\bar{I}_0} \tag{2.23}$$

The formula 2.22 provides a good description of the energy loss for fully ionized projectiles. It allows the calculation of the energy loss for light to medium ions with energies greater than 10 MeV/u. For smaller energy, the effect of shielding the projectile charge through electrons becomes important. A possible description can be given by an effective charge Z_{eff} [10]. The effective charge can be defined as [36]

$$Z_{eff} = \gamma Z_p \tag{2.24}$$

The constant of proportionality γ is given by

$$\gamma^2 = \frac{S(Z_p, Z_T, v_p)}{Z_p^2 S(1, Z_T, v_p)} \tag{2.25}$$

where $S(Z_p, Z_T, v_p)$ is the stopping cross section for an ion with atomic number Z_p penetrating at a speed v_p through a medium with atomic number Z_T. A further discussion on the charge transfer can be found in [37].

2.6 Interferometry

An interferometer can be used to determine the refractive index variation for transparent objects as well as plasmas below the critical density [38]. In this work, a Wollaston interferometer is used to measure the spatially resolved electron density at different instants of time during the plasma expansion. For this, a laser beam with a wavelength of 355 nm is used. Part of the laser beam propagates through the plasma while the other part moves through the vacuum. The portion of the light passing through the plasma experiences phase distortion due to the change in the refractive index of the plasma. This leads to a change in the interference pattern at the detector, from which the electron density can be calculated assuming cylindrical symmetry.

The interaction of electromagnetic radiation of the probe beam with the plasma is mainly determined by the free electron density. The laser radiations generate an electric field in the plasma, due to which free electrons start swinging. They re-emit the radiation, which overlaps with the incident interferometer radiation. The resulting wave propagates with a changed phase velocity $v_{ph} = c_0/N$ from the plasma. With the dispersion relation the refractive index N in a plasma is given by [39].

$$N = \sqrt{1 - \frac{\omega_p^2}{\omega_L^2}} \,. \tag{2.26}$$

Here $\omega_L = 2\pi c_0/\lambda_L$ is the probe laser beam frequency, while $\omega_p \propto \sqrt{n_e}$ is the plasma frequency. The refractive index N can also be written as function of the free electron density n_e and the critical density $n_{e,C}$

$$N = \sqrt{1 - \frac{n_e}{n_{e,c}}} \,. \tag{2.27}$$

For the wavelength of the interferometer light (355 nm) the critical density is 8.8×10^{21} cm^{-3}.

Abel inversion

Interferometry measures the average value of electron density along a chord through the plasma. A recurrent problem is then to deduce local values of the quantity under consideration from the available chordal measurements. However, very many plasmas have the property that they are cylindrically symmetric. This fact enables one to address the problem deducing the radial distribution from the chordal measurements using the known mathematical properties of the Abel transform.

A light beam S, which propagates through an electron density distribution has a modified phase compared to an uninterrupted light beam as shown in figure 2.2. The phase difference results from a change in the refractive index N. By integrating along the light pathway for the phase shift $\Delta\Phi$ is given by

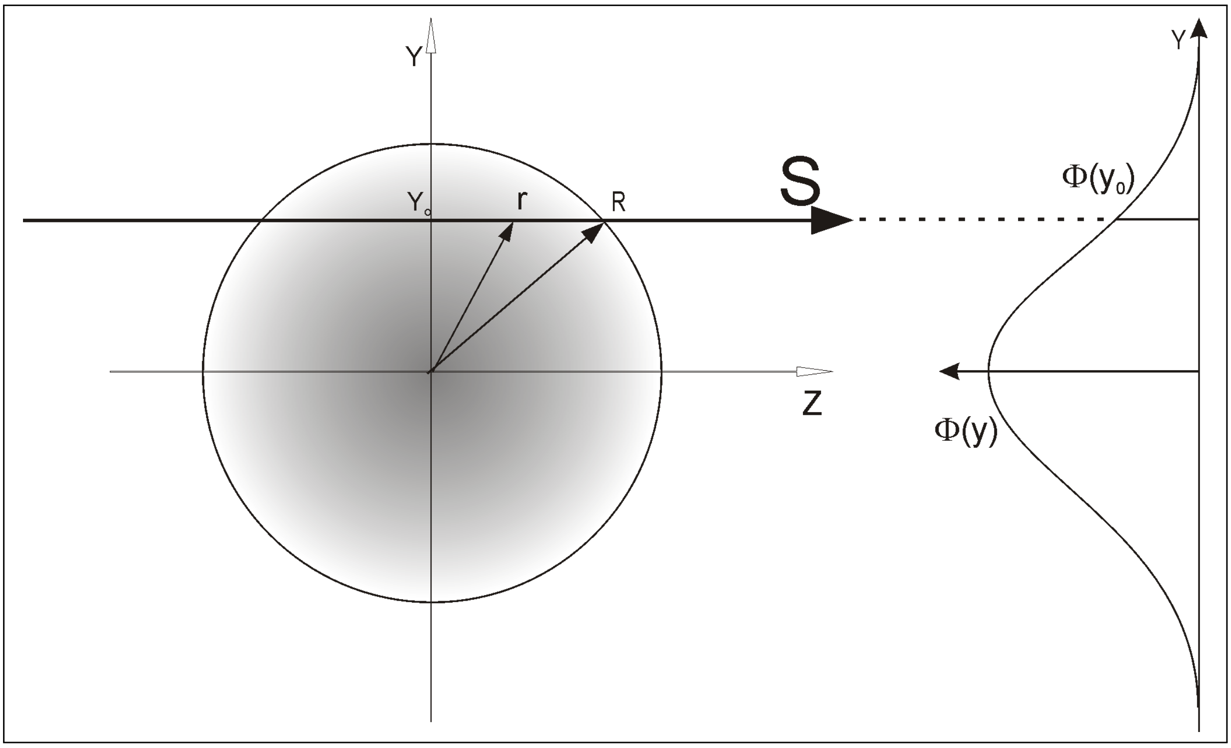

Figure 2.2: Geometrical description of the Abel inversion [38].

$$\Delta\Phi_{(x,y)} = \frac{2\pi}{\lambda_L}\int_{Z_i}^{Z_f} \left(1 - N(x,y,z)\right)\mathrm{d}z\,. \tag{2.28}$$

Here λ_L is the wavelength of light, Z_i is the entrance position of light into the plasma, while Z_f is the exit position. $\mathrm{N}_{(x,y,z)}$ is the spatial dependent refractive index. The phase difference is caused by the spatial dependent refractive index.

Substituting $r^2 = y^2 + z^2 \Rightarrow \mathrm{z} = \sqrt{r^2 - y^2}$ and $\mathrm{d}z = r(r^2 - y^2)^{-1/2} r\mathrm{d}r$, it follows from equation (2.28)

$$\Delta\Phi_{(x,y)} = \frac{2\pi}{\lambda_L}\int_{Y_0}^{R} \frac{r(1 - N(x,r))}{\sqrt{r^2 - y^2}}\mathrm{d}r\,. \tag{2.29}$$

Here Y_0 is the distance to the z-axis and R is the radius of the spatial dependent refractive index (Figure 2.2). This equation is the Abel transformation of the function $\Delta N(x,r) = (1 - N_{(x,r)})$.

Equation (2.29) can be inverted if and only if the electron density distribution has a cylindrical symmetry around a horizontal axis perpendicular to the target.

$$\Delta N(x,r) = \frac{\lambda_L}{2\pi^2}\int_{r}^{R} \frac{\partial\Delta\Phi(x,y)}{\partial y}\frac{\mathrm{d}y}{\sqrt{y^2 - r^2}}\,. \tag{2.30}$$

with the help of equation (2.27), equation (2.29) may be transformed into

$$n_e(x,r) = n_{e,C}\left\{1 - \left(\frac{\lambda_L}{2\pi^2}\int_r^R \frac{\partial\Delta\Phi(x,y)}{\partial y}\mathrm{d}y\sqrt{y^2-r^2}\right)^2\right\} \tag{2.31}$$

The phase shift generated by the free electron density, which can be determined experimentally, is substituted into this equation.

2.7 Fabrication of cryogenic solid targets

Cryogenic crystals of the different gases argon, neon, nitrogen, hydrogen and deuterium have been grown as a part of the present work. For a better understanding of the growth mechanism one must carefully examine the necessary thermodynamic properties of each substance. Some of these properties have been discussed in the following sections.

2.7.1 Triple points and critical points

There are two important fixed points: the triple point and the critical point. The triple point is the single state with pressure and temperature at which the solid, liquid and vapour phases are all in equilibrium. It is the most important point for the sample has to pass through it experimentally each time it freezes or liquefies.

Table 2.1: Temperature and pressure of the target gases at triple and critical points [40, 41, 42].

	Argon	Nitrogen	Neon	Deuterium	Hydrogen
Temperature at triple point (K)	83.806	63.2	24.553	18.73	13.956
Pressure at triple point (mbar)	689.48	125.30	433.32	171.50	72.00
Temperature at critical point (K)	150.70	126.2	44.40	38.35	33.19
Pressure at critical point (mbar)	48.6	34	26.53	16.65	13.15

Table 2.2: Physical properties of the target gases [40, 41, 42].

	Argon	Nitrogen	Neon	Deuterium	Hydrogen
Molar mass (g/mol)	39.984	28.013	20.179	4.029	2.016
Gas density (kg/m^3)	1.67	1.185	0.853	0.168	0.085
Solid state density (g/cm^3)	1.77	1.03	1.51	0.202	0.088
Freezing point (K)	83.95	63.3	24.5	18.6	14.01
Boiling point (K)	77.35	87.29	27.1	23.57	20.38

The critical points are those where liquid and vapour merge into a single fluid phase and the internal translational energy is zero. This is usually considered to be the more important fixed point, from a theoretical point of view. Practically, however, it is not. This is because a very high room temperature gas pressure would be needed to come close to the critical point upon cooling. In most real cases the liquification of hydrogen is obtained at a temperature far below the critical point [40].

2.7.2 Phase diagrams

A typical phase diagram exhibits a gas or a vapour phase, a liquid phase and several solid phases. The liquid-gas boundary ends in a critical point, where as the solid-gas, liquid-gas and solid-liquid phase boundaries intersect at the triple point. The phase diagrams of both hydrogen and deuterium are shown in figures 2.3 and 2.4 respectively.

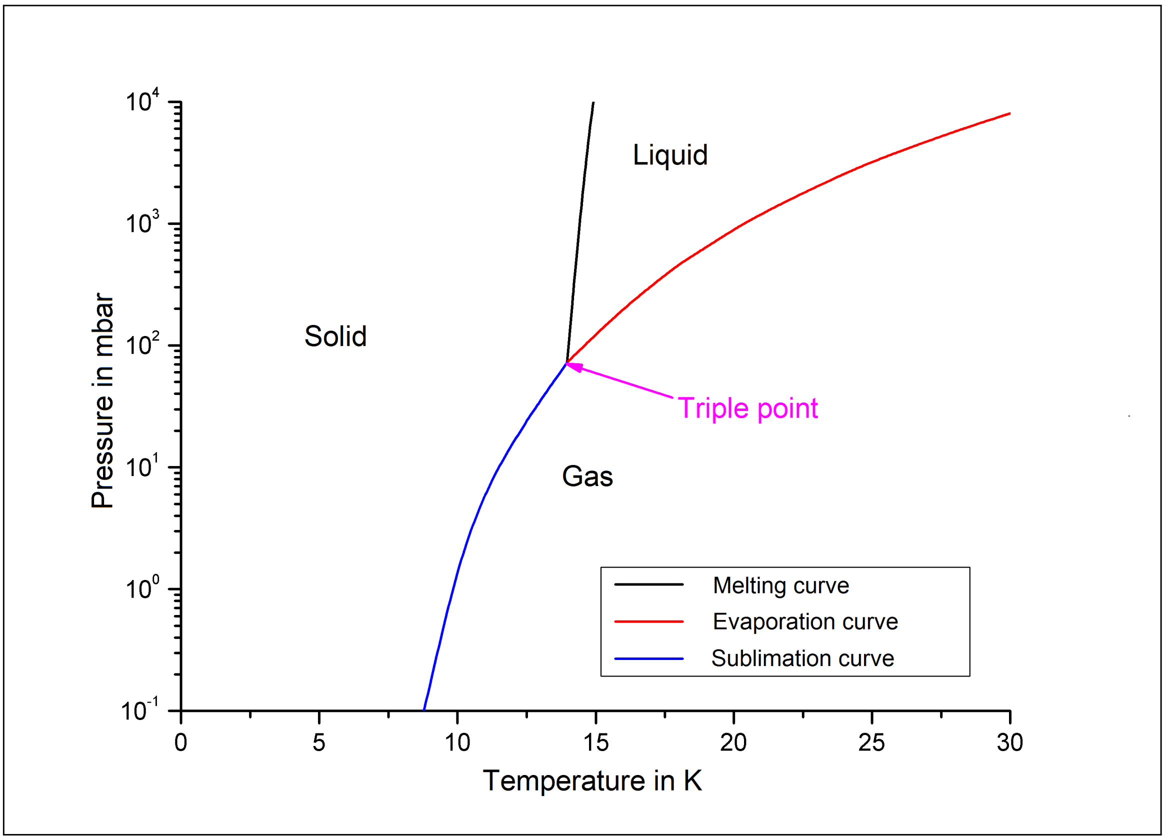

Figure 2.3: Phase diagram of hydrogen [43].

2.7.3 Theory of crystal growth

The study of crystal growth mechanism is a complex subject, involving not only the atomic processes taking place at the growing crystal interface, but also classical problems of heat flow and

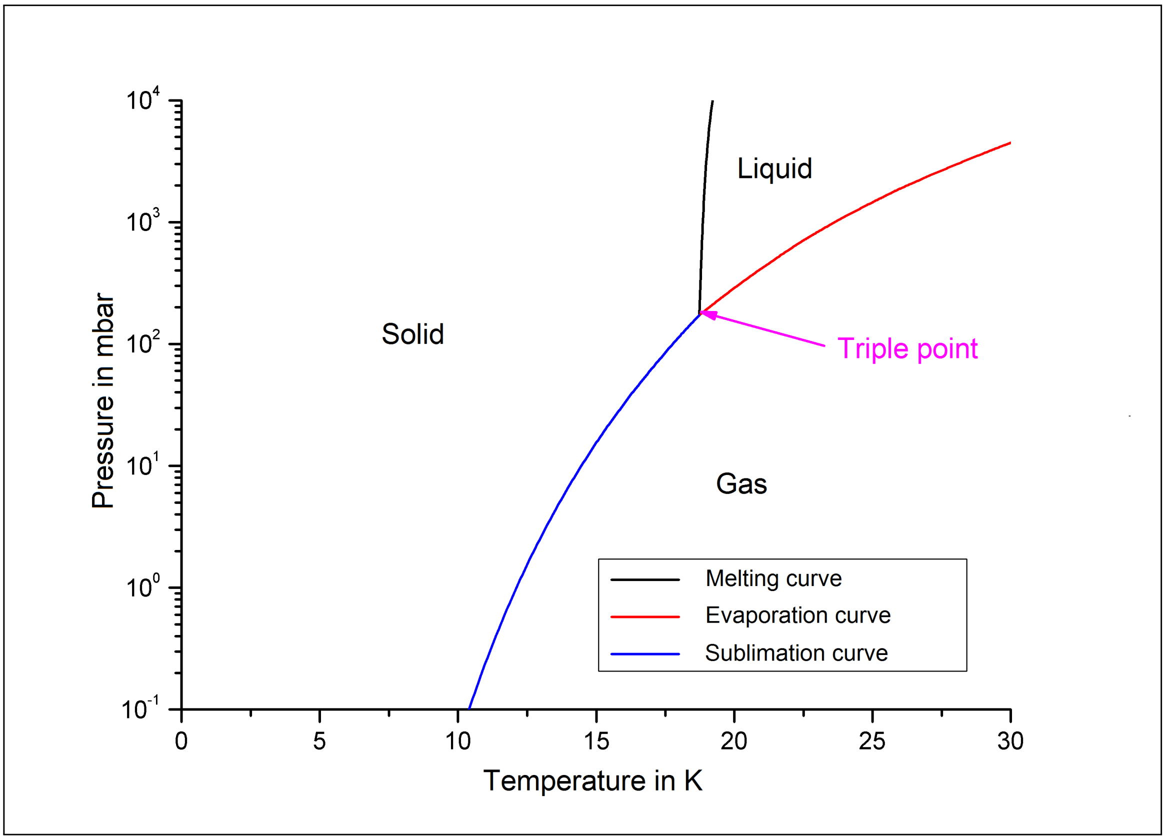

Figure 2.4: Phase diagram of deuterium [43].

mass transport (diffusion) in both the solid and fluid phases [41]. Techniques for growing cryogenic crystals generally fall into one of the three categories: namely, growth from the vapour, growth from a solution, or growth from the liquid (or melt). In the case of vapour growth at low pressure the atomic processes are most important, but in growth from high pressure vapour or from the melt, heat flow and diffusion in the fluid can be dominant.

The roughness of the solid-fluid interface on an atomic scale determines the pattern of crystallization. Based on the simple nearest neighbour bond models of the interface the important parameter is α. When α is small, the interface is rough and vice-versa [44].

$$\alpha \simeq 2/3(L/kT) \tag{2.32}$$

where L is the latent heat of transformation. The interface is rough if $\alpha < 2$.

Crystal growth from the liquid

The method is in principle very simple. A sample of liquid is formed in a suitable container and then cooled until it solidifies. In practice, however, uniform cooling from the liquid may produce defective samples due to a combination of factors. Firstly, the thermal expansivity of the rare gas solids may well be more than 100 times that of the container it is grown in.

This, coupled with a small yield strength near the triple point and relative brittleness at low temperature means that the defects are introduced by temperature changes. Secondly, the low latent heat of fusion of the solids means that crystals can easily be grown too quickly and defects appear on solidification. All rare gases have $\alpha < 2$, and thus having atomically rough interface, and the crystal growth rate is limited by the rate of heat removal only.

Crystal growth from the vapour

When crystals are grown below the triple point, pressure and temperature solidification takes place directly from the vapour, with no liquid present. The general rule is that the growth from the vapour produces finer grained, and more defective, polycrystals than the growth from the liquid. Nonetheless, for some experiments, thin films of the solids are required and it is natural to grow those by vapour deposition. For rare gas crystals, vapour growth leads to much higher values of α, since the relevant value of L is now the latent heat of vaporization and T is the temperature of the crystal which can be much less than the melting temperature. The values of α for vapour growth at the triple point range from 5.9 for Ne to 6.3 for Xe. These values should give rise to faceted growth, where low index crystal faces are formed which are atomically smooth [45].

3 Experimental Setup

At GSI the Z6 experimental facility is unique worldwide for it combines state of the art high power lasers and heavy ion beams: an ultimate temptation to realize beam plasma interaction experiments. In this chapter details of the experimental setup are given. After a brief overview of the accelerator facility and the laser systems at GSI, the diagnostics for the study of plasma, laser and ion beam properties are described.

3.1 The UNILAC

The wide range of experimental activities at GSI is based on a multi stage accelerator facility mainly consisting of a UNILAC[1], a heavy ion synchrotron SIS[2] and an ESR[3]. The UNILAC serves two functions. It provides ions for experiments at low energies and also acts as a pre-accelerator for the SIS. It can be filled with different types of ions using three distinct ion sources and can accelerate ions of any kind from protons to uranium within the energy range of 3.6 – 20 MeV/u. A schematic view of different accelerating stages of the UNILAC along with the low energy experimental areas is given in figure 3.1.

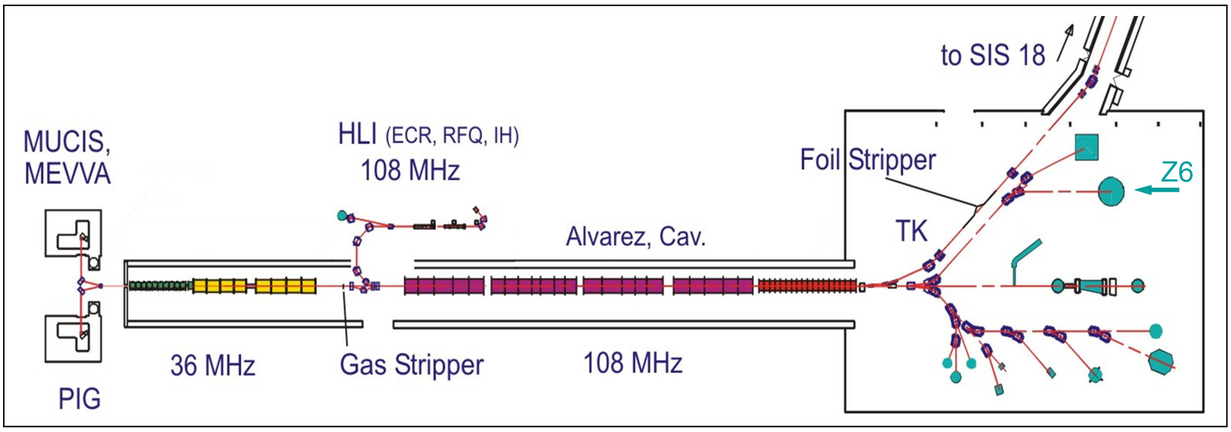

Figure 3.1: Schematic view of the UNILAC accelerator at GSI [46].

Located at the beginning of the beam path are the injectors MUCIS[4], MEVVA[5] and PIG[6] ion sources, from which low-energy small-charge-state ions are extracted through an RFQ (Radio Frequency Quadrupole) which operates at a frequency of 36.136 MHz. This frequency is imprinted on the ion beam bunch structure corresponding to a peak-to-peak distance of 27.673 ns.

---

[1] **Uni**versal **L**inear **Ac**celerator

[2] **S**chwer**i**onen**s**ynchrotron

[3] **E**xperimental **S**torage **R**ing

[4] **Mu**lti **C**usp **I**on **S**ource

[5] **Me**tal **V**apour **V**acuum **A**rc

[6] **P**enn**I**n**G** ion source

The ions then pass through a supersonic gas beam, in the process of which they undergo such violent collisions that many more electrons are stripped off than initially was the case in the ion source. Next comes the Alvarez section which consists of four tanks and operates at a frequency of 108.408 MHz. The energy is increased step-wise from 3.6 MeV/u to 11.4 MeV/u. Behind the Alvarez section there is a single resonator section which accelerates the ions to higher energies depending on the ion species, for instance, $^{238}U^{28+}$ can be accelerated up to maximum energy of 17.7 MeV/u [46].

Another ion source, high charge state injector HLI[7] is additionally installed at the Alvarez stage. This injector is designed to produce ions with a high charge state and uses an ECR (Electron Cyclotron Resonator) ion source. After a first acceleration ions from this source are directly injected into the Alvarez section and use the full Alvarez frequency corresponding to a peak-to-peak distance of 9.2 ns between the pulses.

The energy loss measurements from laser induced plasmas performed by the plasma physics group at GSI are conducted at the Z6 experimental area. The characteristic features of the ion beam used at the Z6 are: if the accelerator is using the north or south ion sources the time difference between the beam's micro bunches is about 27 ns. If the accelerator is using the HLI ion beam the micro bunches have a FWHM duration of 2-3 ns and a peak to peak distance of 9.2 ns.

3.2 The *nhelix* laser system

The *nhelix*[8] laser can be used to generate and diagnose hot dense plasmas. The laser scheme is shown in figure 3.2. The system comprises of two commercially available laser oscillators, the Powerlit (OS1)[9] and the Geola (OS2)[10]. The OS1 is a Nd:YAG resonator and uses a Pockels cell as an active Q-switch. The Q-switch generates a Gaussian shaped pulse of 15 ns FWHM duration. However for the purpose of creating a plasma the laser pulse shape should have a sharply rising edge in order to heat the target instantaneously. Thus another Pockels cell is used to transform the Gaussian shape into an almost rectangular shape. The 3 ns rise time of these pulses is limited by the rise time of the Pockels cell's high voltage pulse.

Kepler telescopes are used to increase the beam diameter, and in the focal plane of these telescopes, apertures are used to filter out high spatial frequencies. Thus the setup also acts as a spatial filter which smooths the beam profile. The lasing material is a Nd:YAG crystal. The maximum achievable energy is 100 J over 15 ns. The amplified light is transported to the Z6 target chamber over a bridge and focused onto the targets through a lens doublet. A phase plate is placed between the lens and the target in order to achieve a spatially homogeneous laser focus on the target. With a 10 ns long pulse carrying 50 J and a focal spot of 1 mm, an intensity of 5×10^{11} Wcm^{-2} has been delivered to the target. With a small focus of 50 μm,

---

[7] Hochladungsinjektor

[8] Nanosecond High Energy Laser for Ion EXperiments

[9] Model: Powerlit precision 8000, company; Continuum

[10] Model: G-Mini-B100-GSI, company : Geola Technologies

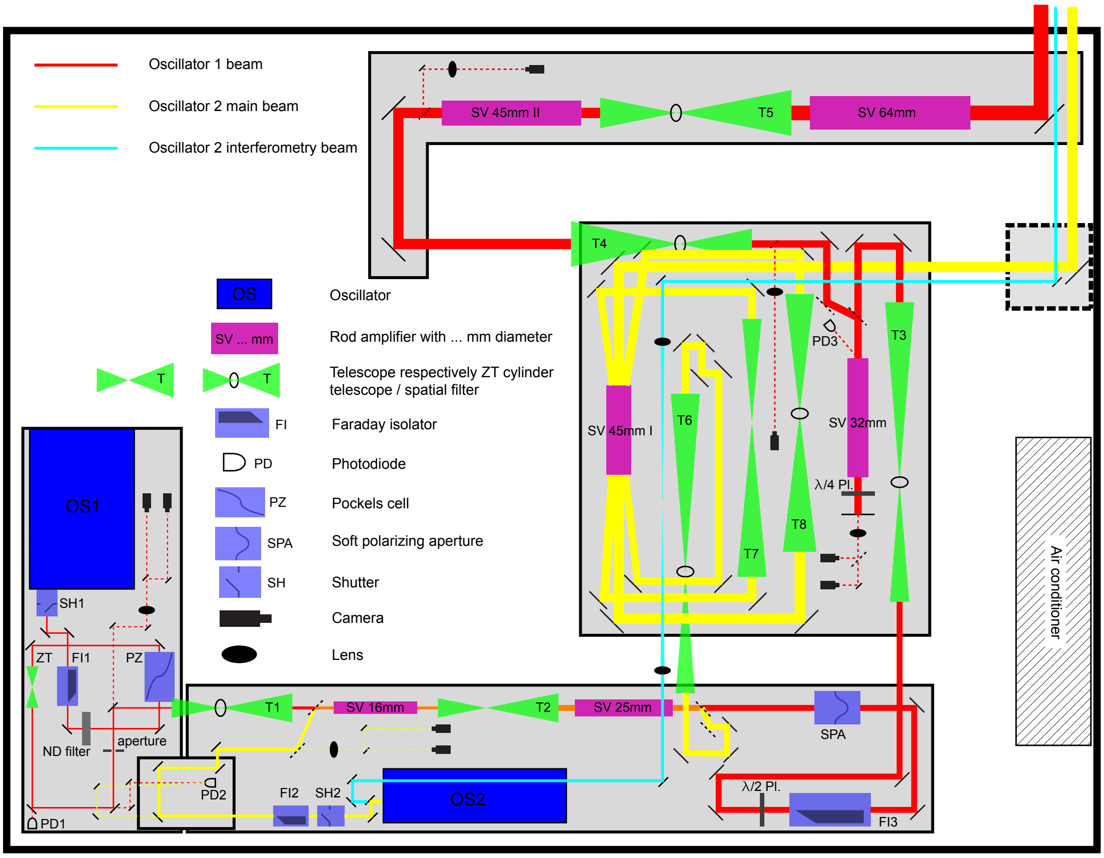

Figure 3.2: Schematic view of the *nhelix* laser system [47].

however, an intensity of 10^{14} Wcm^{-2} is also possible.

The OS2 is also a Nd:YAG laser. The pulse is created with an active Q-switch. The pulse duration is 5 ns FWHM which is further shortened to 0.5 ns using a SBS (Stimulated Brillouin Scattering) box. This beam can be frequency doubled to a wavelength of 532 nm. It is also possible to triple the frequency. At 3ω the beam has a wavelength of 355 nm which is used for interferometric measurements.

3.3 The PHELIX laser system

The PHELIX[11] is a flash lamp pumped Nd:Glass laser system capable of generating intense laser beams with energies upto 1 kJ or likewise power exceeding 500 TW. The facility has added promising opportunities for energy loss experiments at the Z6 as well as other experiments like proton acceleration and X-ray laser generation. The schematic view of the system is given in figure 3.3.

---

[11] Petawatt High-Energy Laser for Heavy Ion EXperiments

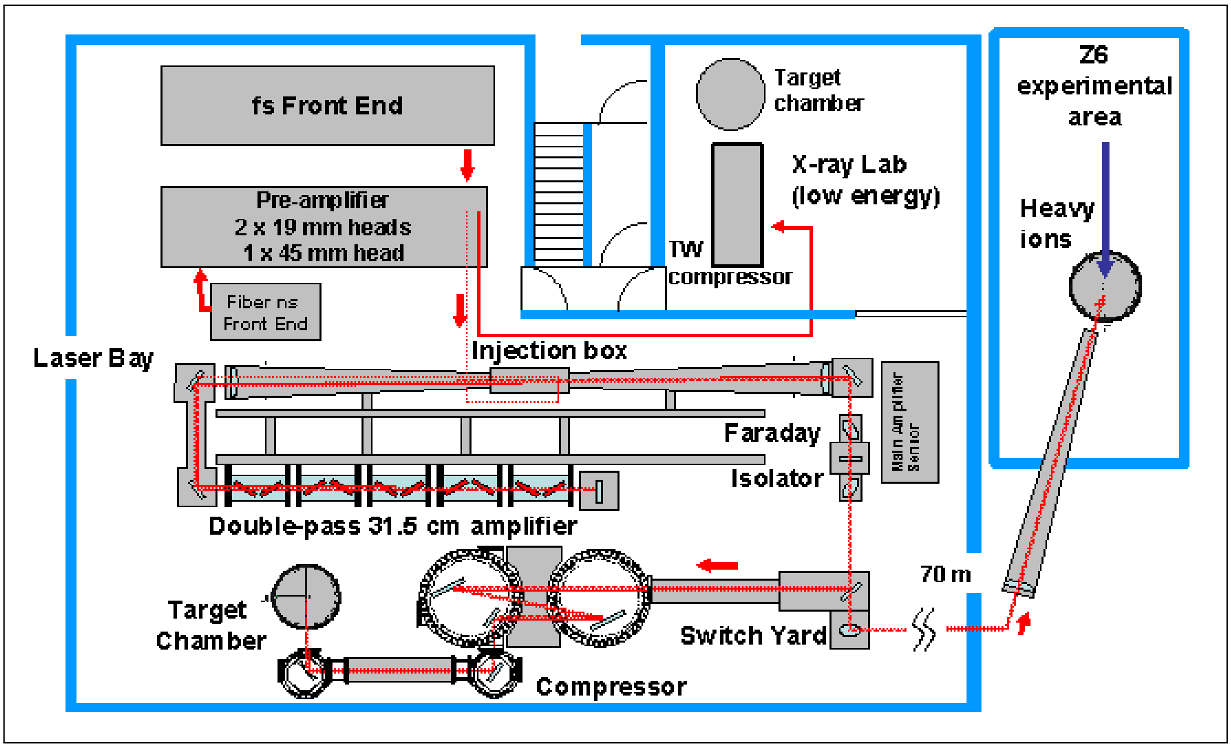

Figure 3.3: Schematic view of the PHELIX laser system [48].

The major parts of the system are two front ends, a pre-amplifier and a main amplifier. The so called Chirped Pulse Amplification CPA is used to generate extreme laser intensities exceeding 10^{20} Wcm^{-2} while high energy beams are delivered by the nanosecond front end which delivers arbitrary pulse shapes and pulse duration between 1 and 15 ns. The main parts of the front end are a fibre base cw single mode[12] laser, an acousto-optic modulator, a double-pass fibre amplifier and an intensity modulator. The nanosecond front end can generate laser pulses with a duration between 700 ps and 20 ns. The system delivers pulse energies upto 10 nJ. These pulses are feeded to a flash lamp pumped regenerative ring amplifier. The resulting energies are upto 20 mJ with a repetition rate of 0.5 Hz. A femtosecond laser oscillator[13] inside the femtosecond laser front end can generate 100 fs, 4 nJ laser pulses. The chirped pulsed amplification is achieved through an adjustable pulse stretcher, where a pulse is stretched in time, amplified and re-compressed. The stretched pulse is further amplified through a regenerative linear and ring shaped Ti:Sapphire amplifier. The amplifier produces pulses of 1.2 ns and a typical energy of 30 mJ.

The pre-amplifier mainly consists of three flash lamp pumped Nd:glass amplifiers. The input delivered by the femtosecond front end can be amplified up to 5 J, while 50 nJ pulse from the nanosecond front end is amplified up to 10 J. The main amplifier consists of the Nd:glass amplifier cassettes which can achieve a maximum gain of 100. The maximum output energy for the fs pulse is 250 J while for the ns pulse the output energy is 1 kJ. The repetition rate of

---

[12] Koheras Basik

[13] Coherent Mira

the whole system is 90 minutes when operating in the high energy mode.

3.4 Diagnostics

Several diagnostics have been developed in order to examine the characteristics of the laser and ion beams as well as plasmas generated at the Z6. These include a Wollaston interferometer for plasma free electron density measurements while the plasma temperature can be measured through a X-ray streak or a pinhole camera [37]. A visible streak camera is used to record the plasma expansion and the measuring of its velocity whereas the same can be done using a fast shutter CCD camera. A few of these diagnostics are described in the following sections.

3.4.1 The Wollaston interferometer

The principle of the laser interferometry is based on the fact that the plasma index of refraction is proportional to the free electron density. The variation in the index of refraction is similar to a change in the path length of a laser beam, resulting in a phase shift. From the phase shift the electron density can be calculated with the help of Abel inversion method which assumes cylindrical symmetry. This is automatically done by a computer program [38].

For typical interferometric measurements, the expanding plasma is placed in one of the arms of the interferometer, whereas the probe beam passes orthogonal to the plume expansion direction. The method permits an accurate determination of the electron density and is particularly used during first instants of the plume expansion. The Wollaston interferometer, however, allows beam splitting after it has passed through the plasma. This is done using a Wollaston crystal. The concept of the Wollaston interferometer at the Z6 is illustrated in figure 3.4.

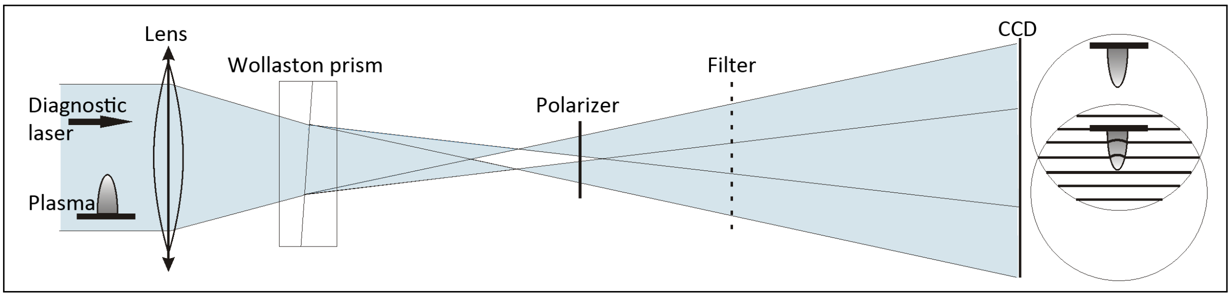

Figure 3.4: Design of a Wollaston interferometer at the Z6: The undisturbed upper part and the lower parts of the beam leave the Wollaton prism at such an angle that they interfere at the image plane [38].

A small extracted part of the Geola beam which is frequency tripled at 355 nm is used as probe beam. This pulse is defocused and partly passes through the plasma while the rest is propagating through the vacuum. In the Wollaston birefringent crystal two perpendicularly polarized beams are produced which propagate at a small angle to each other. Finally a polarizer oriented at 45° is placed so that the transmission is the same for both polarizers and thus leads to a contrast enhancement. An interferometer filter stops the stray light and the light from the plasma to reach the camera.

3.4.2 The streak camera

In the present work a streak camera[14] has been used to record plasma plume expansion. The streak camera converts incident light into electrons and performs a high-speed sweep, enabling detection of the time variation of the incident light intensity by converting these into different positions on the screen. The working principle is illustrated in figure 3.5. The light pulse to be measured is focused onto the photocathode of the streak tube through the slit, where the photons are converted into a number of electrons proportional to the intensity of the incident light. These electrons are accelerated and conducted towards the phosphor screen, and a high-speed voltage which is synchronized to the incident light is applied. The electrons are swept at high speed from top to bottom and are then multiplied in the MCP (micro-channel plate), after which they are bombarded against the phosphor screen of the streak tube and converted to an optical image [49]. Using calibrated streak images the glowing plasma velocity can be determined.

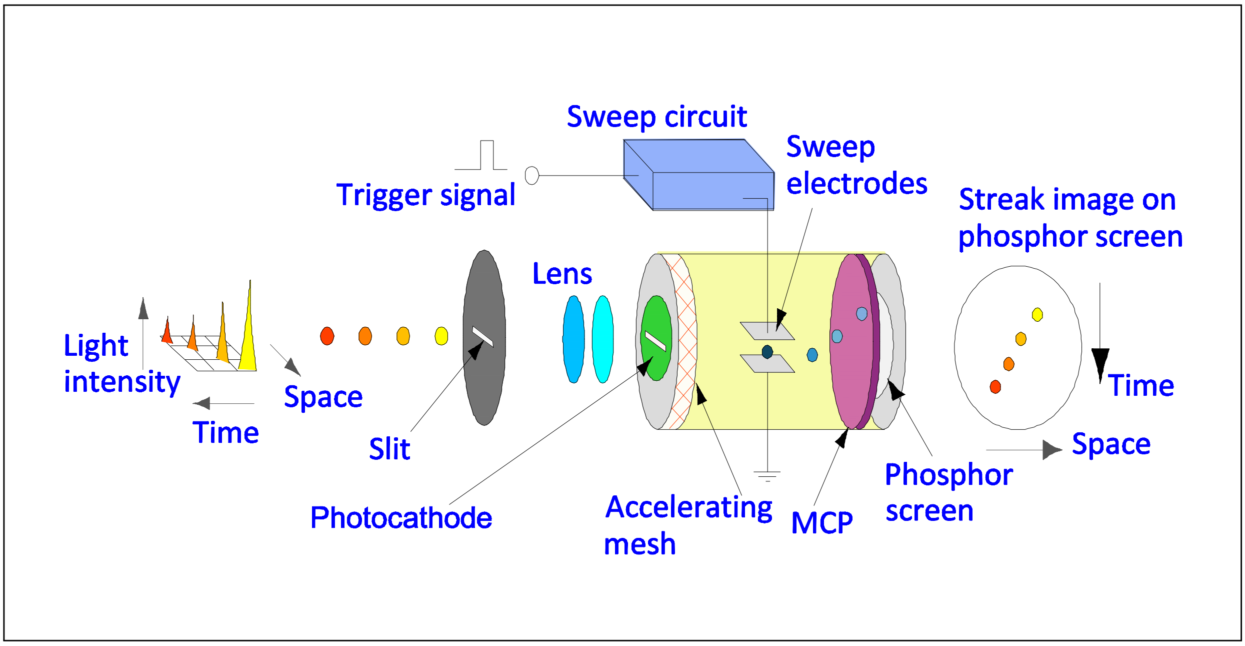

Figure 3.5: Working principle of a streak camera [50].

---

[14] Streak Camera C2830 Hamamatsu Photonics

3.5 Experimental setup for the energy loss measurements

The experimental setup for the energy loss measurements of heavy ion beams interacting with hot dense laser produced plasmas is schematically depicted in figure 3.6. Both sides of the target foils are irradiated with the *nhelix* and PHELIX lasers. The third laser directed perpendicular to the direction of the plasma expansion maps the plasma for interferometric measurements. The ion pulses from UNILAC are focused with the help of a quadrupole in the middle of the target chamber, where the target is located. The projectiles give off part of their kinetic energy during the interaction with the plasma and then set with a reduced speed to a diamond detector after covering 12.1 m distance. The diamond detector measures their arrival time with a high temporal resolution.

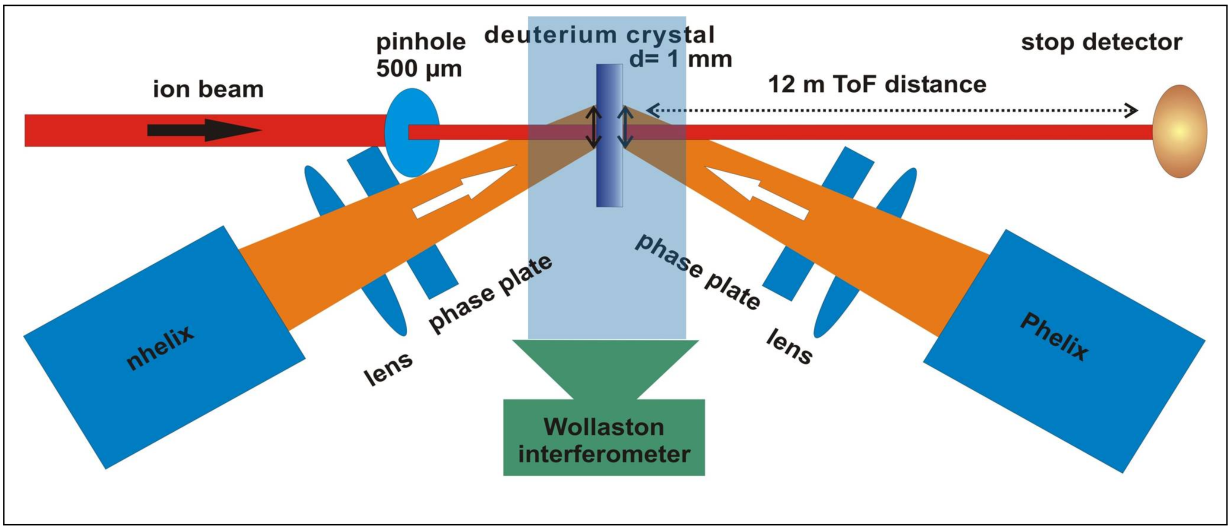

Figure 3.6: Schematic view of the energy loss experiment at the Z6 [51].

Although the diamond detector has a good temporal resolution it cannot perform spatially resolved measurements. Therefore the arrival time of the projectiles coming along the plasma axis cannot be distinguished from those coming from the edges of the plasma. For a better understanding of the beam-plasma interaction one needs to prevail constant plasma parameters at least within the cross section of ion beams. The laser focusing on the target has a direct influence on plasma parameters. For instance, if the incident beam has a Gaussian profile the intensity distribution varies sharply such that it reduces to half at the boundary compared to the centre of the focus. A phase plate between the lens doublet and the target foil can solve the problem. It produces small scale intensity non-homogeneities on the focal spot however the intensity remains constant over the entire focal envelope. The quadrupole magnet can focus the ion beam only upto few millimetres. Therefore a circular aperture of 500 μm diameter is used to reduce the beam waist while the laser focal spot is kept to 1 mm for the present experiment. For energy loss measurement the so-called time-of-flight method is used, which is described in the next section.

3.6 The time-of-flight (TOF) method

The energy loss measurements mainly involve three stages. At first, the ions propagate through a cold target and loose a part of their kinetic energy corresponding to the target thickness. The signal at the stop detector shows a constant energy loss. Then the laser pulse heats the target and turns it into a plasma. The interaction of projectiles with plasma changes their kinetic energy and hence their time-of-flight. Figure 3.7 shows the delayed arrival of the micro pulses resulting from enhanced energy loss of the ions traversing through the plasma. Finally the target vanishes due to hydrodynamic motion which results in a reduced energy loss detected by a negative delay of the ion bunches at the stop detector. With this method the energy loss can be detected before, during and after the plasma formation in one single shot. Using the precise micro structure and a time-of-flight distance the energy loss can directly be deduced from the time of arrival of subsequent ion bunches. The measurements of ion-beam energy loss through the cold target can also be calculated using SRIM (Stopping and Range of Ions in Matter) [52]. These measurements together with the data obtained from the time-of-flight method can be used to calculate the target thickness. A detailed description of the time-of-flight method can be seen in [34, 37, 53].

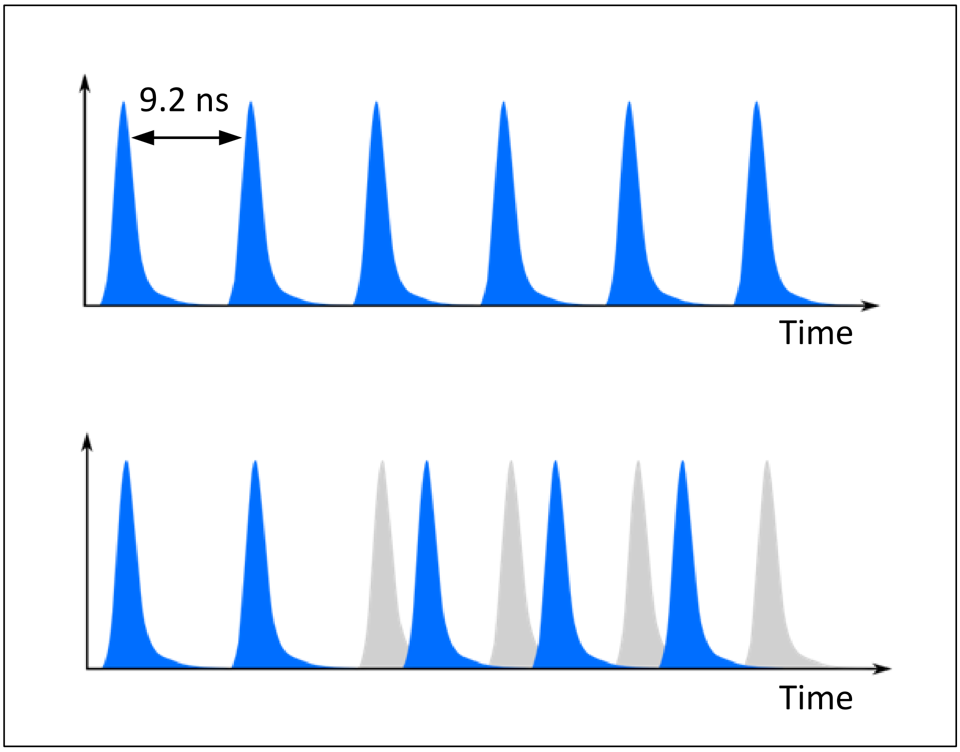

Figure 3.7: Typical view of ion beam pulses before (top) and after (bottom) suffering delay due to plasma ignition (grey: expected arrival ; blue: actual arrival) [54].

4 Design, Fabrication and Installation of the Cryogenic Target System

The cryogenic system [43] has been developed and tested at the Technical University of Darmstadt and was later installed at the GSI Z6 experimental area for beam-plasma interaction experiments. The system cannot be deployed permanently at the Z6 since the facility is in use for different experiments. Therefore it was mandatory to build a separate robust test system that can be operated off-line as well. The setup comprises a test chamber, a cryostat, target growing chambers, gas supply system, temperature and pressure sensors and an electron source for target thickness measurements. After a brief description of the design and the development of these parts, different methods of target fabrication have been discussed. Finally, the installation of the system at the Z6 experimental area is presented.

4.1 The cryostat

The cryostat is a closed cycle SRDK-415D[1] cryocooler. It consists of a cold head (RDK-415D), a compressor unit (CSW-71), interconnecting flexible gas lines and a buffer tank. The cold head is a two-stage Grifford McMahon (GM) cycle cryo-refrigerator capable of producing continuous closed cycle refrigeration depending upon the imposed heat load. The specifications of the system are listed in table 4.1.

Table 4.1: Specifications of the cryogenic system [55].

Cold head RDK-415D	Cooling capacity	1st stage	35 W
		2nd stage	1.5 W
	Low temperature typical	1st stage	50 K
		2nd stage	4.2 K
	Cool down time (2nd stage)	<60 min (4.2K)	
	Dimensions (mm)	180 x 294 x 557	
	Weight	18.5 Kg	
Compressor CSW-71	Filling pressure	16.5 Kg f/cm^2 G (235 psig)	
	Cooling	Water	
	Dimensions (mm)	450 x 500 x 686	

---

[1] Sumitomo Heavy Industries Limited Tokyo Japan

The cold head mainly consists of a cylinder, two displacers, a drive mechanism and a cold head drive motor. A schematic view of the system showing the cold head cross section and the operating cycle is given in figure 4.1. The cylinder contains a displacer inside and is closed at both ends. The length of the displacer is about three quarters of the cylinder. With the help of the drive motor, the volumes above and below the displacer can be varied from zero to maximum, but the total volume remains constant. The two spaces are connected through a thermal regenerator to a gas supply system which consists of inlet-outlet valves, a helium gas compressor, and high and low pressure reservoirs. The valves are coupled to the rotary drive mechanism and their operation is synchronized with the position of the displacer. For the supply and return of helium a pair of 6 m (20 m without buffer tank) long interconnecting flex line is provided. A heat exchanger is included downstream of the helium gas compressor to cool the gas to the ambient temperature after the compression.

The refrigeration operation, as illustrated in figure 4.1, completes in four steps.

1 Pressure build-up: The displacer stays at the bottom of the cylinder. The inlet valve is open and the outlet valve is closed, which results in a pressure increase and the fluid flows through the inlet valve to fill the regenerator and the space V_1 above the displacer.

2 Intake stroke: The inlet valve opens and the displacer moves from the bottom of the cylinder to the top displacing the high pressure fluid from V_1, through the regenerator to V_2. In passing through the regenerator the gas cools causing the pressure to decrease and further gas enters the system to maintain the maximum cycle pressure.

3 Pressure release and expansion: With the displacer at the top of the cylinder the inlet valve closes and the outlet valve opens, fluid escapes decreasing the pressure and hence decreasing the temperature of the gas in V_2. This is the useful refrigeration process of the cycle.

4 Exhaust stroke: With outlet valve open, the displacer is brought to its initial position. The fluid is displaced from V_2 to V_1 and the cycle is completed.

4.2 The target growing chamber

Solid targets are grown on a copper block called target support which is fixed to the cryostat anvil. In order to deposit the gas onto the target support a retractable growing chamber is used. The volume and the shape of the crystal is defined by the shape of the growing chamber. Figure 4.2 shows a sketch of the target growing mechanism and a typical growing chamber.

In order to grow a cubic or a round cylindrical crystal the growing chamber is made by inserting a square or a bowl-like cup of metal (copper or steel) into a PVC-block. The gas inlet is connected using a Swagelok. At the top of the chamber a M6 screw is fixed that can be joined with the manipulator to precisely approach the cold head and to set back after the crystal has been grown. The metallic growing chambers have produced good quality crystals, however, optical view of the crystal growing process is not possible. Therefore, transparent plastic like

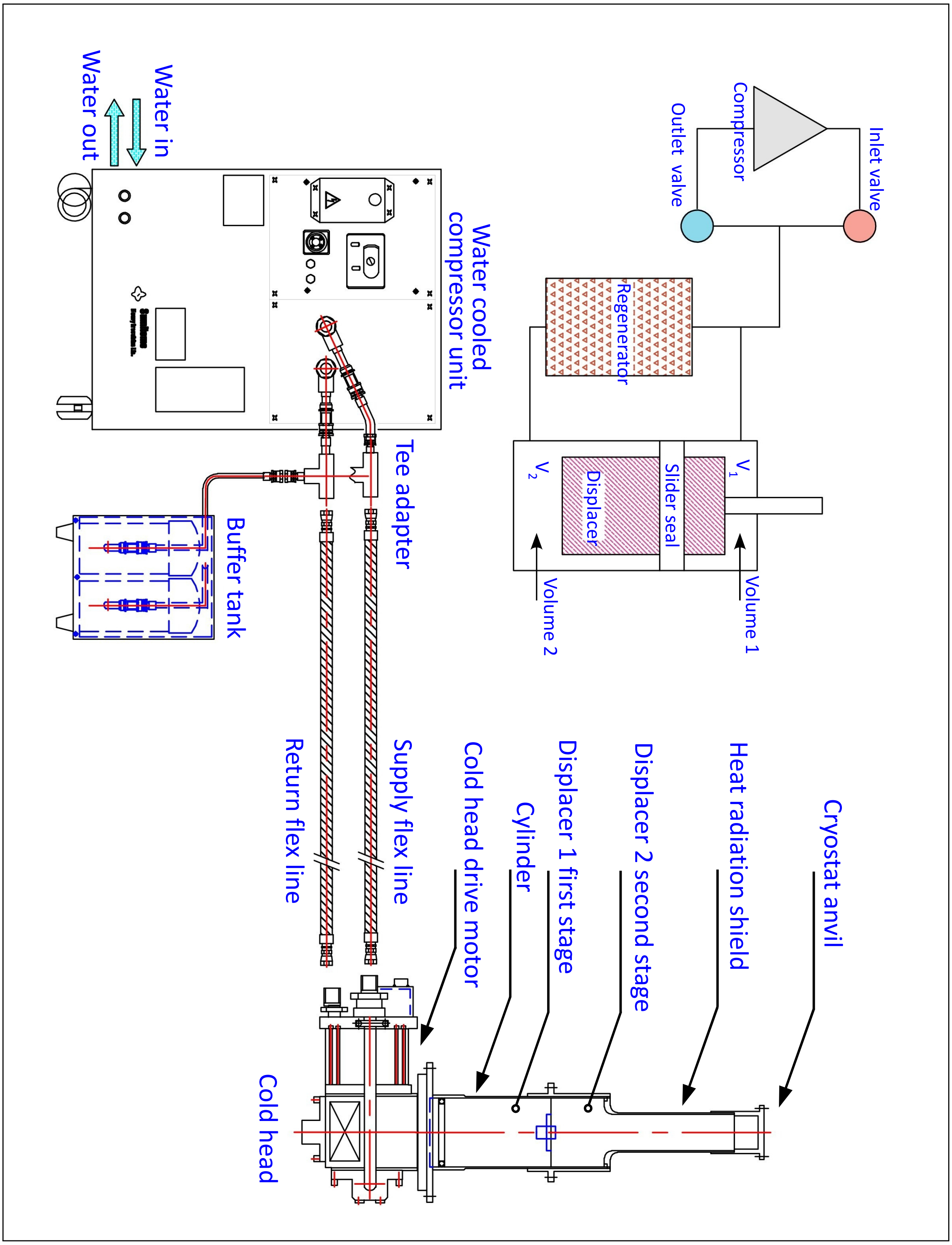

Figure 4.1: Schematic view of the cryogenic system and the Grifford McMahon refrigeration principle.

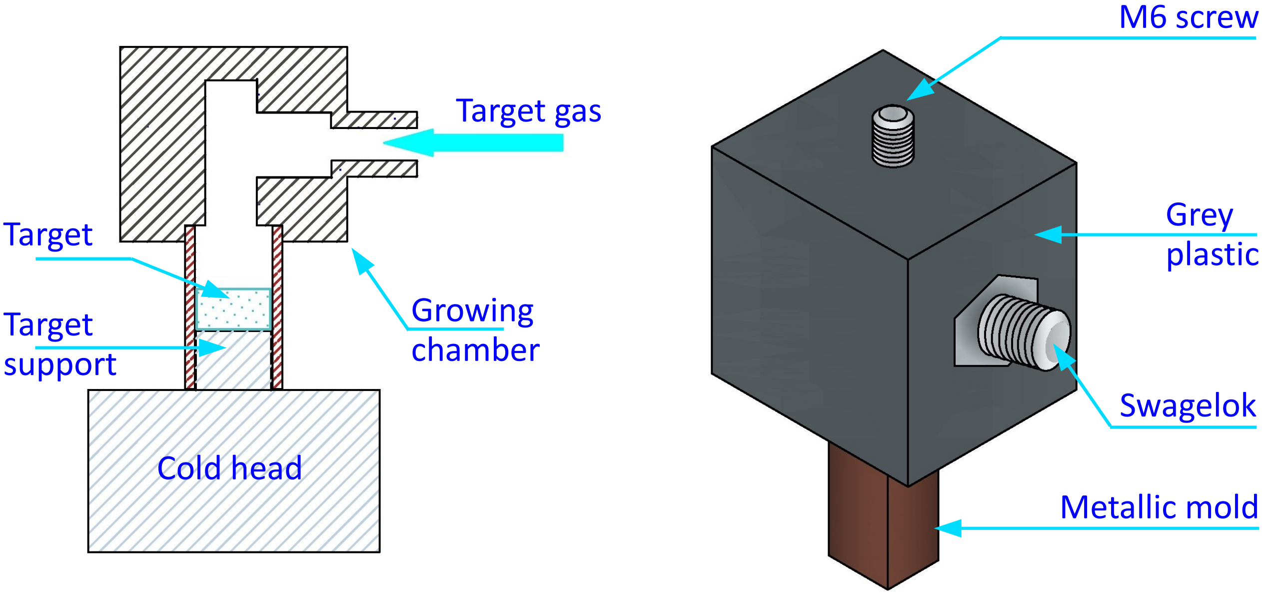

Figure 4.2: The construction of a target growing chamber used to grow cubic shape crystals. The idea of gas deposition onto the target support is also depicted.

plexi glass has also been used to manufacture growing chambers. When the crystal has grown, the growing chamber is lifted and the crystal can be exposed to the laser beam for plasma generation.

4.3 The gas supply and handling system

The main parameters to be controlled during target growth are the temperature of the cooling head and the gas pressure inside the target growing chamber. As indicated by their phase diagrams (section 2.7.2), solidification of different gases requires different pressures. In order to maintain a steady gas flow during the target growth and removal of the residual gases, a gas supply system has been developed. The scheme of the system is shown in figure 4.3. The system mainly comprises a mass flow control unit, a pressure sensor, control valves, a diaphragm vacuum pump and a gas pre-cooling arrangement.

Before growing a crystal the gas feed system is evacuated to eliminate any water vapours. The gas is feeded to the mass flow control (MFC) through a pressure reducing valve(1) connected

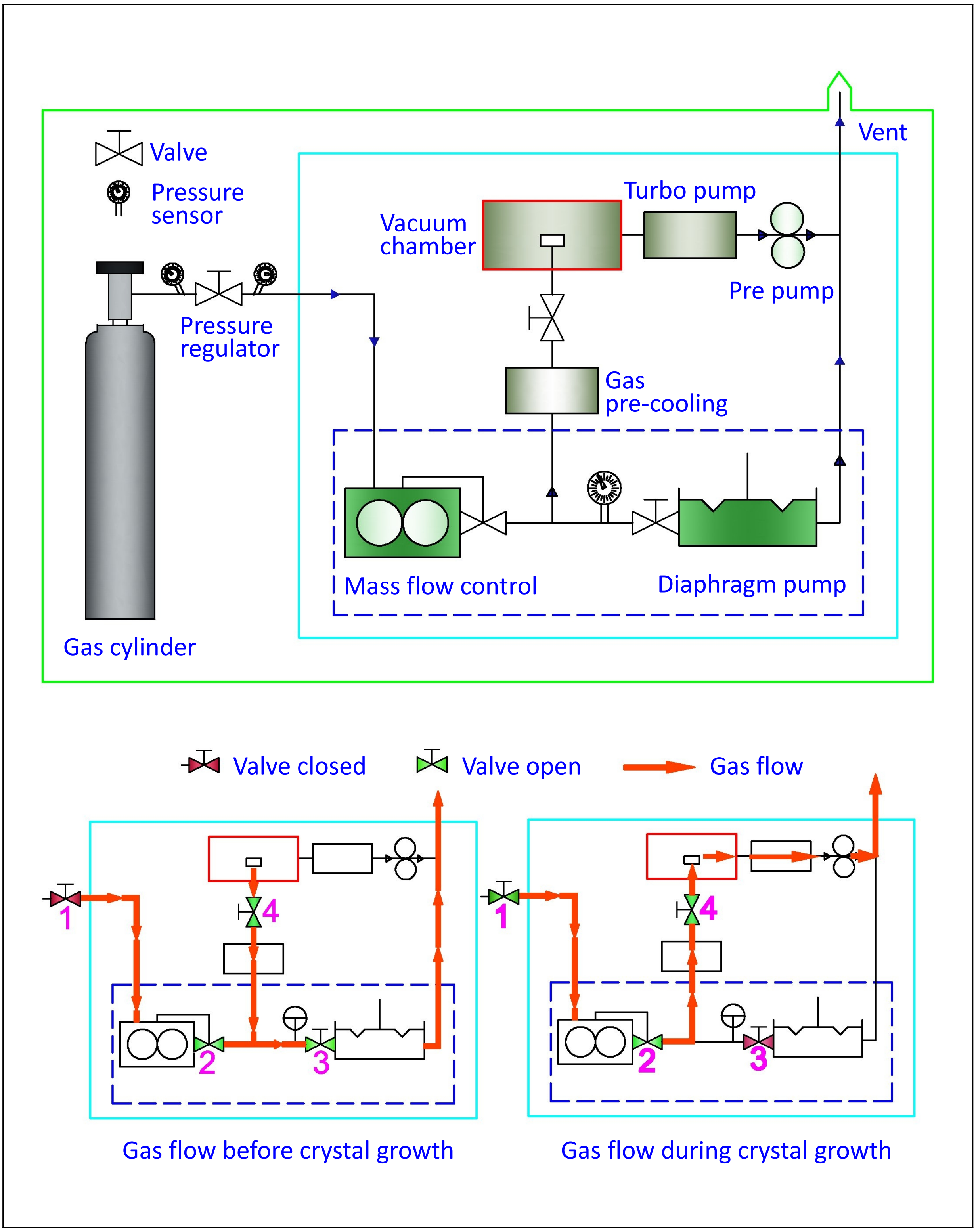

Figure 4.3: Topology of the gas supply system to grow cryogenic targets. Below is the sketch to illustrate the direction of gas flow before and during the target growth.

with the gas cylinder. The mass flow control is a closed loop device that sets, measures and controls the flow of the gas. For crystal growth as shown in figure 4.3, the gas enters into the growing chamber through another valve. An almost stationary gas flow is maintained by the mass flow control until the crystal is grown. When the crystal has grown the gas supply is stopped by closing the valve(2), and the residual gas within the system is evacuated by the diaphragm pump. In case of hydrogen and deuterium safe removal of the residual gas is necessary. For this the outlets of the vacuum pumps are coupled together and the gas remains within the closed duct until it is vented through the roof exhaust using a high pressure air blow.

Gas pre-cooling

If the gas is introduced into the growing chamber at room temperature, it causes an increase of a few Kelvin of temperature when it gets in contact with the target support. For the growth of rare gas and nitrogen crystals this is not an issue as the temperature remains below the triple point anyhow. In case of deuterium and hydrogen having freezing temperatures of 18 K and 13 K respectively, the situation is different. If the temperature rises to 18 K or higher, the target growth is difficult. One possible way to cope with this problem is to increase the inertia of the target support. This is, however, not feasible for the present working conditions. The other possible solution is to pre-cool the gas at liquid nitrogen temperature (77 K) so that the low temperature at target stage remains relatively stable. To implement the idea a spiral made of copper pipe (4 mm diameter) was inserted into the gas supply line. The spiral shown in figure 4.4, is dipped into a dewar flask containing liquid nitrogen.

4.4 Temperature control and measurements

For temperature measurements cernox[2] thin film resistance temperature sensors[3] have been used. Each sensor is calibrated from 1.4 K to 300 K. They are highly sensitive to temperature variations at low temperature but have a good sensitivity also at higher temperatures. The sensors are well suited for the present experimental set-up for they have excellent resistance against ionizing radiation and low magnetic field induced errors.

The temperature is displayed on an eight-channel temperature monitor[4] which also provides current sources for sensor operation and memory for each sensor to store the calibration data. In order to eliminate the effects of lead resistance, cernox sensors use a 4-lead measurement. Two of the leads supply current to the sensor, while the other two leads are used to eliminate the effect of lead resistance by measuring the voltage at the sensor voltage leads. The reason this measurement scheme works is that the voltage drop in the current leads is not measured, and the voltage drop in the voltage leads is extremely small due to the very small current required by the voltmeter (picoamperes or less) to make the voltage measurement.

---

[2] Cernox is the trade name for Zirconium oxy-nitride

[3] Lake Shore Cryotronics, Inc

[4] Lakeshore Temperature Monitor Model 218S

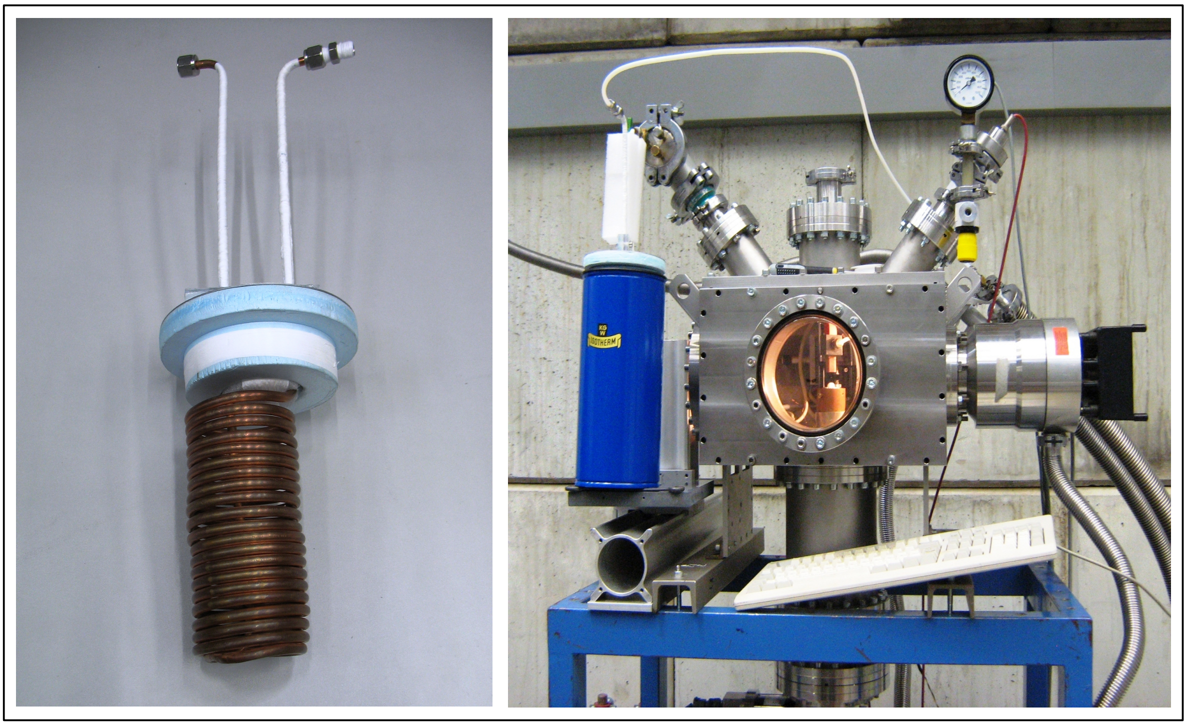

Figure 4.4: A spiral made of copper pipe (left) immersed in liquid nitrogen filled dewar flask (right) to cool the target gas.

For increasing the heat load, a 3 m long (16.5 ohm) heating element[5] with cold ends was coiled around the cold head. The core of the element was made of nickel-chromium with a stainless steel sheath material. Setting an appropriate value of load across the heater, one can easily control the temperature up to 50 K.

4.5 Measurements of the target thickness

The knowledge of the target thickness and uniformity is essential since it is a key parameter to analyze experimental results. The thickness can be measured using an ion beam, however, an alternate method is also needed so that the thickness can be measured off-line as well. For this an electron source has been developed. The details of the system are given in [43]. The schematic view of the electron source for thickness measurements is given in figure 4.6.

The electron source is an electron tube (Model 3-659)[6] housed in a separate vacuum system. The test chamber and the electron source chamber are connected through a manual valve. This is necessary to keep the electron source always in vacuum to avoid water contamination which

---

[5] Thermocoax standard heating element

[6] Clinton Electronics Corporation

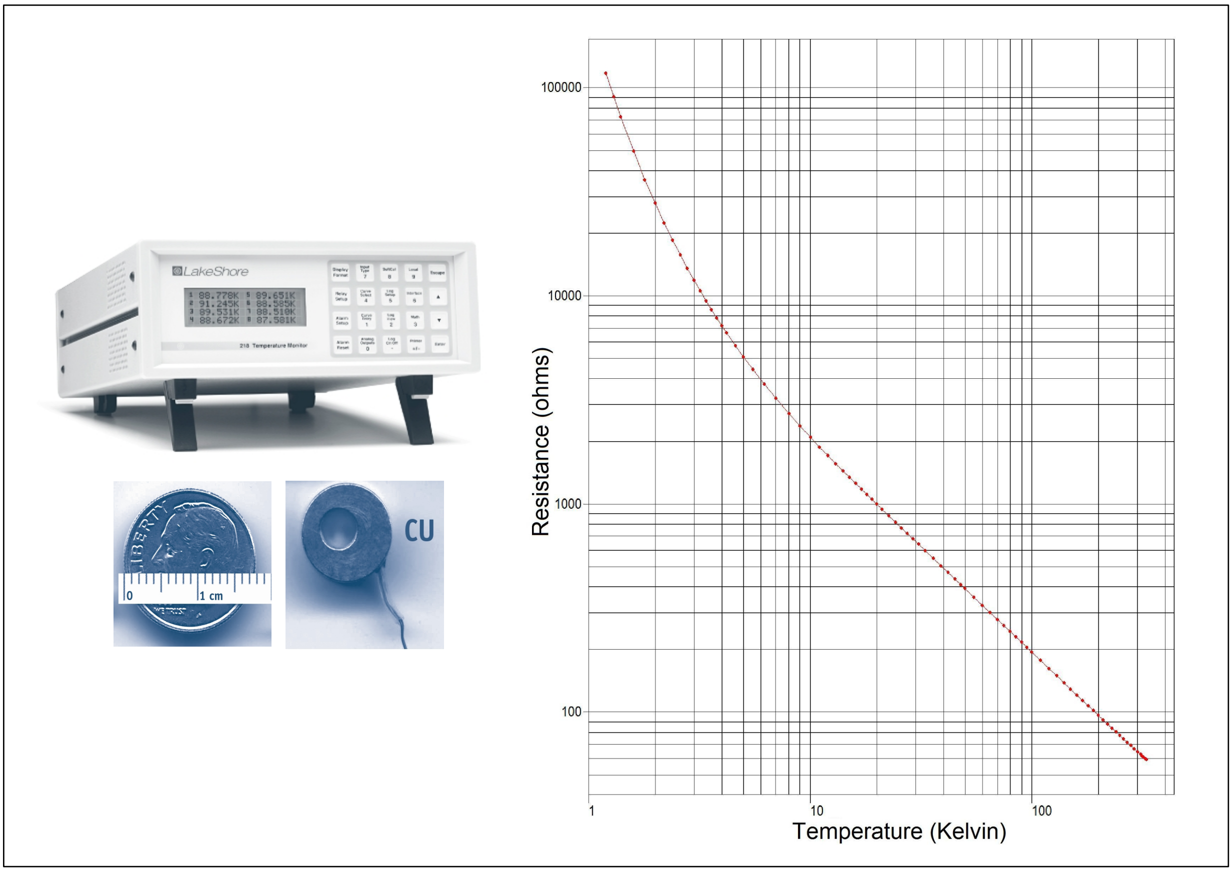

Figure 4.5: Temperature monitor and sensor along with calibration curve [56].

may erode the electron tube. The high potential and the filament current for the electron tube are supplied from the power supply NGR-15kV[7]. The deflection of the electron beam is done by the help of magnets, whereas electrostatic lenses are used to focus the beam on the target. After the electrons have passed through the target they are collected at a Faraday cup and the current is measured using an ammeter[8]. The value of the current corresponds to a certain electron flux, and the thickness can be calculated using the simulated correlation between electron flux and corresponding thickness.

The combination of electrostatic lenses and dipole magnets as shown in figure 4.7, has been used to transport the electron beam to the target. The bending magnets are four pole pieces, placed at an angle of 90° from each other such that they circle the path of the electron beam. The pole pieces are made of an iron core to which a wire is wounded. The strength of the magnetic field and hence the deflection can be controlled by changing the current in the windings. The electrostatic lens integrated within the electron source can focus the beam upto 5 mm approximately, however, electrostatic lenses between the two deflection magnets can focus the beam roughly upto 2 mm. The focusing potential can be varied between +600 V and -900 V. For

---

[7] IBT Elektronik GmbH

[8] Keithley 177 Microvolt DMM

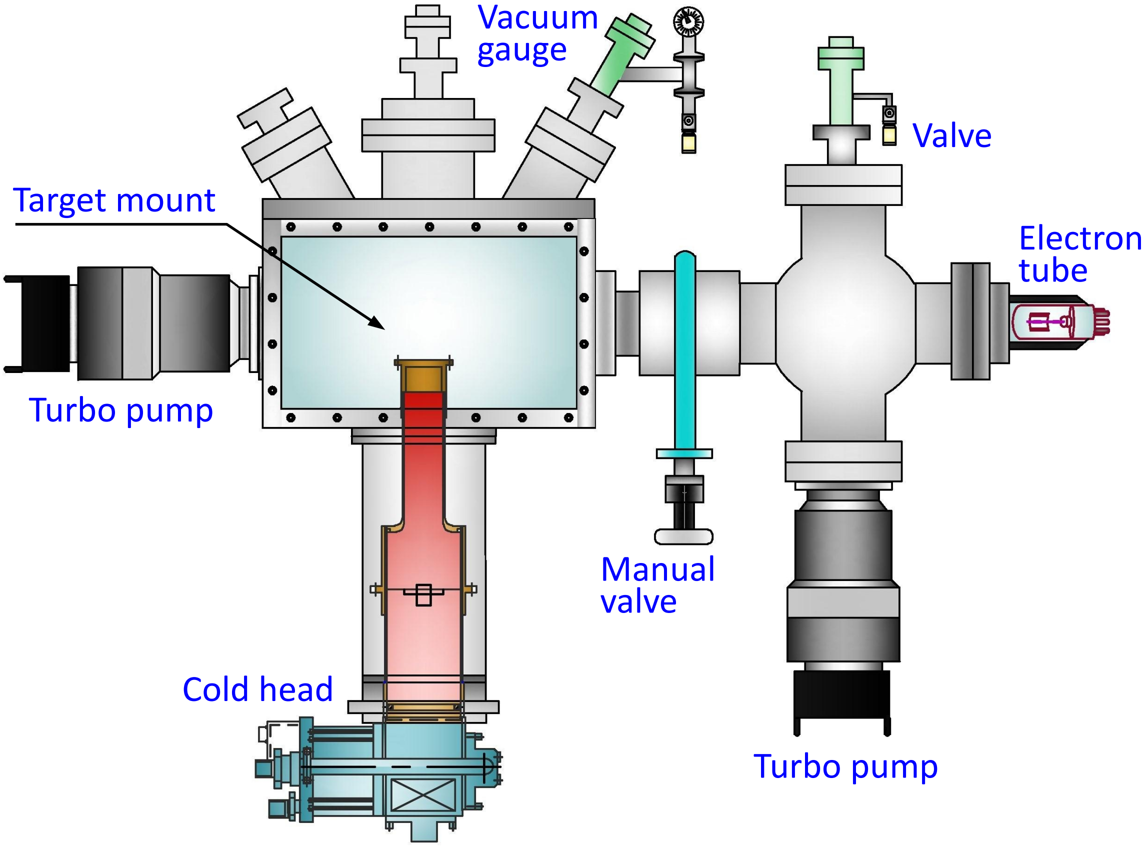

Figure 4.6: Installation of the electron source to measure the thickness of the target.

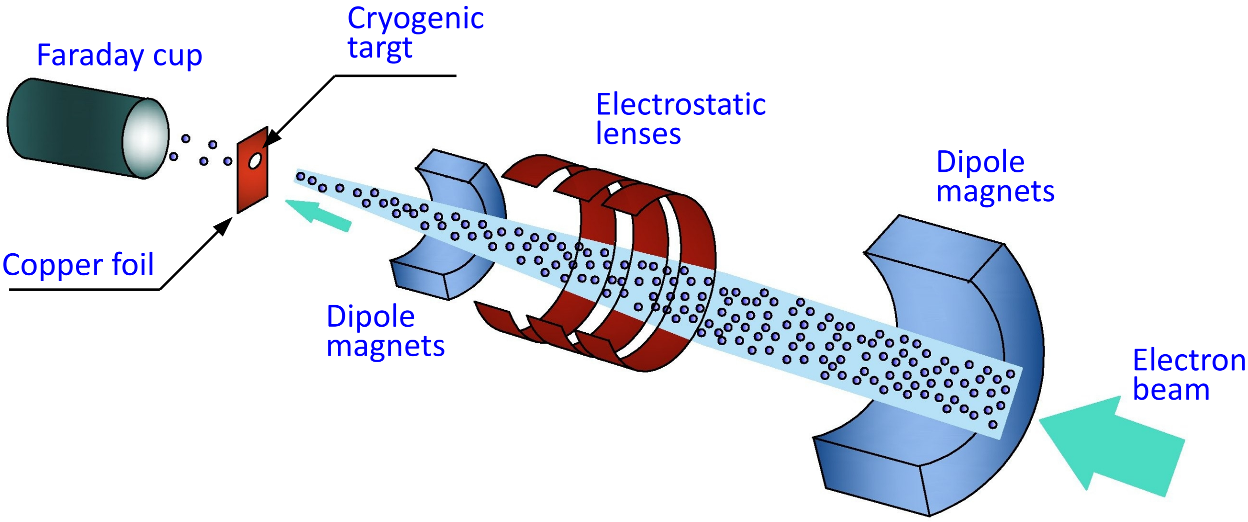

Figure 4.7: The combination of the electrostatic lenses and deflection magnets for the transport of the electron beam to the target for thickness measurements.

adjustment of the beam position, scintillator material is placed at the position of the Faraday cup.

4.6 Free standing cm-size rare gas targets

To start with the testing of the cryogenic system rare gas argon crystals have been grown, since the freezing temperature for argon is 83 K, close to that of nitrogen. Therefore similar conditions, as in the case of argon proved appropriate to grow transparent reproducible nitrogen crystals for the laser plasma experiments at the Z6. As a second choice neon crystals have been grown. For neon the freezing temperature is 24 K, which is close to the freezing point of deuterium. Therefore, for normal operation and testing, neon appears to be quite suitable since it is safe to work with, while deuterium needs special care to meet safety requirements. Cryogenic round argon and quadratically shaped neon targets of cm-dimensions are shown in figure 4.8.

At the interface between the target support and the cold head a thin indium foil is placed to stop gas leakage from the growing chamber. In this way a firm sealing is assured otherwise gas leakage does not allow to maintain the required pressure and hence the target growth. The process lasts from 5 to 20 minutes depending on the gas type.

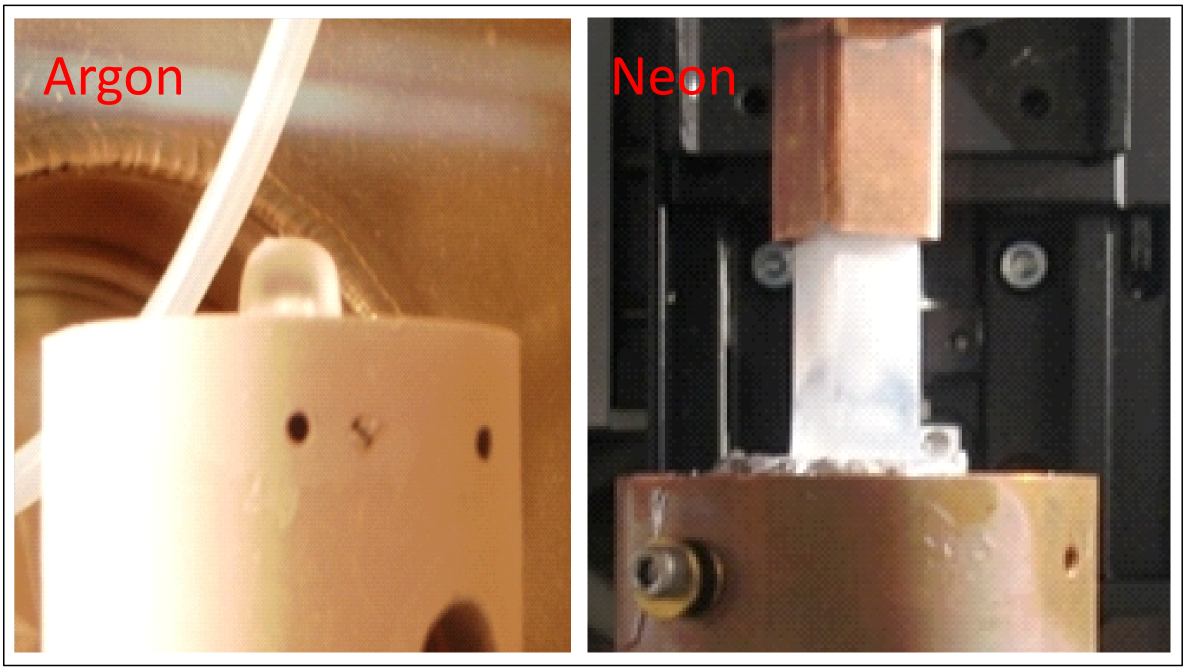

Figure 4.8: Free standing argon and neon solid targets.

4.7 Free standing mm-size solid targets

Free standing thin cryogenic targets can be used for many interesting laser plasma experiments [57, 58]. As described in the previous sections the size and shape of the mold determine the size and shape of the target, a small target mold with 1 mm thickness has been tested to fabricate free standing thin targets. The growing procedure is the same as described for cm-size targets. Figure 4.9 shows free standing neon (front and side view) and deuterium targets. The deuterium target was broken during retracting the growing chamber. The problem is typical for the targets that have been grown using a mold, as the thermal expansivity of the cryogenic crystals is greater than the container. However, taking special measures the fracture can be avoided [59].

4.8 Free standing cryogenic nitrogen targets

The first laser produced plasma experiments have been performed with nitrogen cryogenic crystals as targets. The arrangement for growing the crystals within the Z6 target chamber is depicted in figure 4.10.

The geometry of the growing chamber has been described in 4.2. A small cubic block of copper has been used to support the target. The growing chamber stays over the target support such that this small block is immersed into it and the rest of the volume is filled with the target. As a first benefit, this eliminates the use of the indium foil. The tiny spaces located within

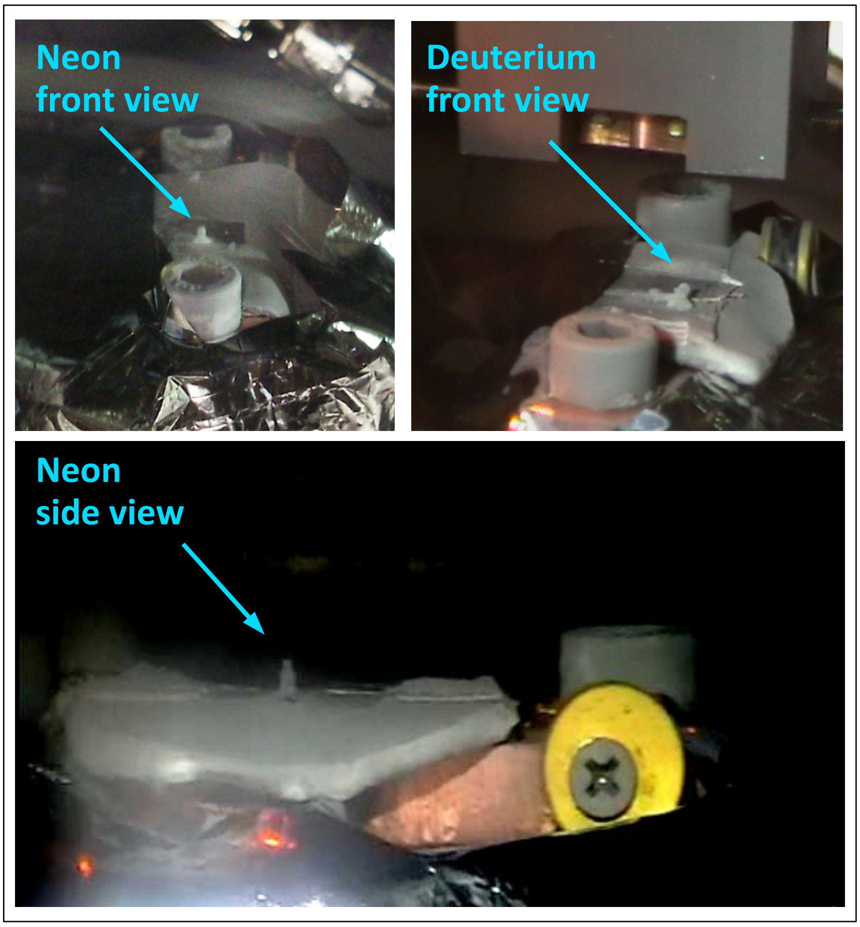

Figure 4.9: Free standing mm-size neon and deuterium crystals.

the contact area between the growing chamber walls and the copper block are initially filled by the freezing of the target gas, stopping any further leakage. Secondly, the position of the block keeps the position of subsequent target fixed and hence always properly adjusted to the experimental setup.

Solid nitrogen targets are grown by fast deposition of the gas onto the target support. A stainless steel cup, with outer dimensions of 1 cm × 1 cm square cross section serves as mold for the growing of the target. The stainless steel is better as it prevents heat conduction to the environment. The gas is initially introduced slowly, until a visible seal is made between the mold and the target support by the frozen gas. The solid made during this is amorphous as observed by its snowy appearance. Once the seal is made the gas pressure is increased to 100-200 mbar. After completion of the growth, the flow is shut and the mold is then retracted, leaving behind an optically clear, free standing target. The targets are of cubic shape with fairly plane faces. One such crystal is shown in figure 4.11. The laser beam has been focused at one of the side faces of the crystals in order to produce a plasma.

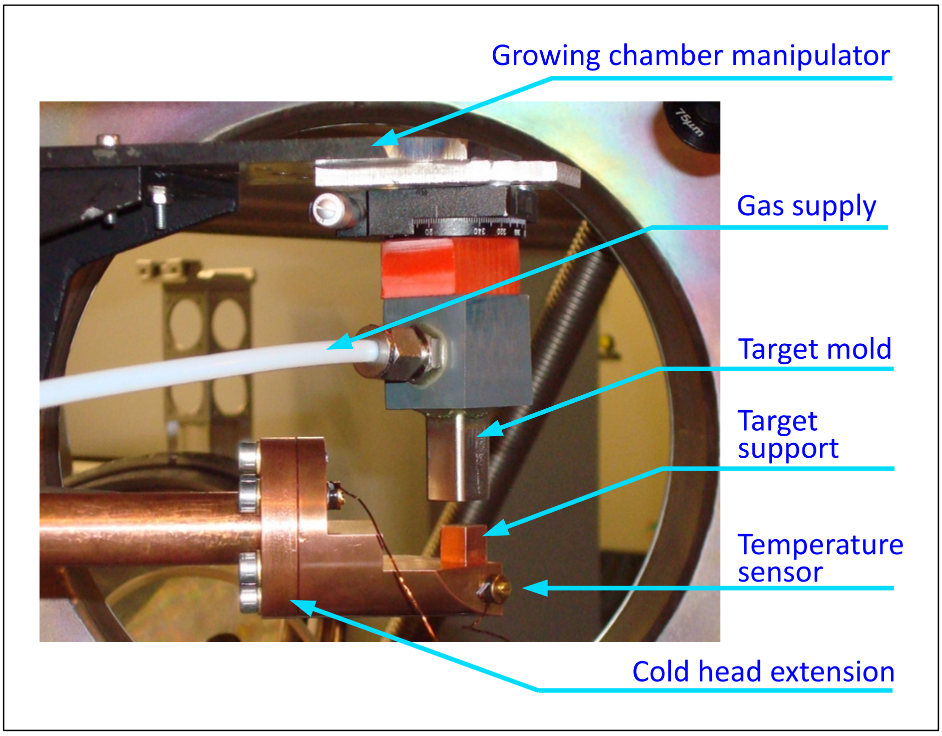

Figure 4.10: Setup for growing nitrogen crystals at the Z6 target chamber.

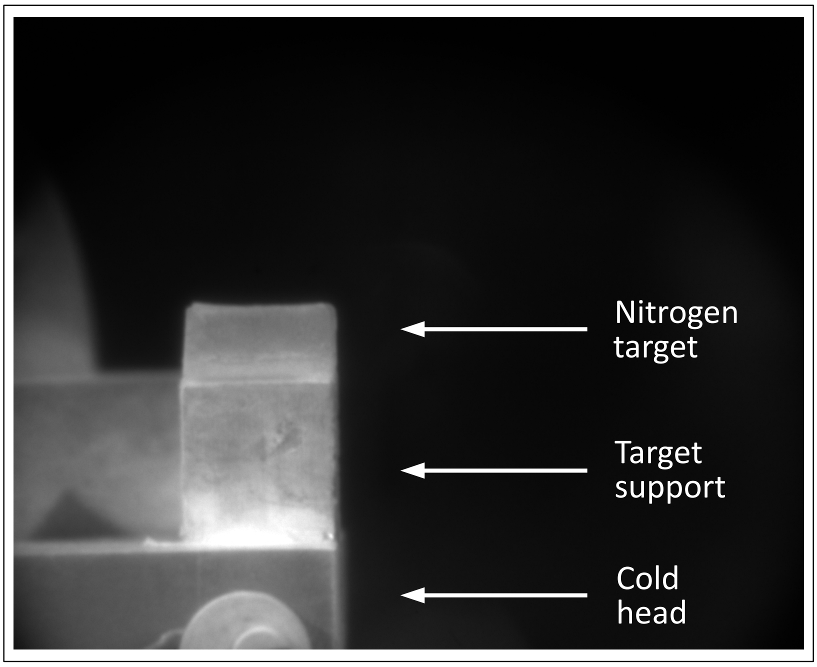

Figure 4.11: Cryogenic nitrogen crystals grown at the Z6 target chamber.

4.9 Thin copper-foil supported deuterium targets

At the Z6 experimental area, the energy loss experiments performed until now, have used thin carbon foils as targets for the plasma generation. The commissioning of the cryogenic system at the Z6 offered an opportunity to use foil-like hydrogen targets. For the first experiments, however, deuterium has been selected owing to its higher melting point (18 K) as compared to hydrogen (13 K).

Figure 4.12: Cryogenic thin planar foil of deuterium [43].

A 500 μm thick copper foil is used to support the target. Inside the foil a circular hole of 2 mm diameter is made to house the target. The foil is screwed with the target support. The walls of the growing chamber made of plexi glass surrounds the copper foil and the deuterium gas freezes within the space of the hole. The nominal time to grow the crystal is about 30 minutes.

4.10 Deployment of the cryogenic system at the Z6

The target chamber at the Z6 is roughly a spherical (1 m diameter) stainless steel chamber. In the outer walls, portholes of different sizes are symmetrically integrated. The interior of the chamber can be accessed from eight vertically aligned ports while the rest of the ports are inclined at an angle of 45°. There is only a little room for the installation of the cryogenic system because the chamber is crowded with diagnostics and passages of laser and ion beams. Therefore, certain modifications have been performed to adjust the cold head to conventional Z6 experimental conditions. The position of the target must be at the centre of the chamber where the laser beam is focused. The length of the cold head is not sufficient to reach the centre, therefore an extension is needed. For this a 26 cm long copper rod has been added to the cold head's 2nd stage. The sketch of the extension along with other accessories is shown in figure 4.13.

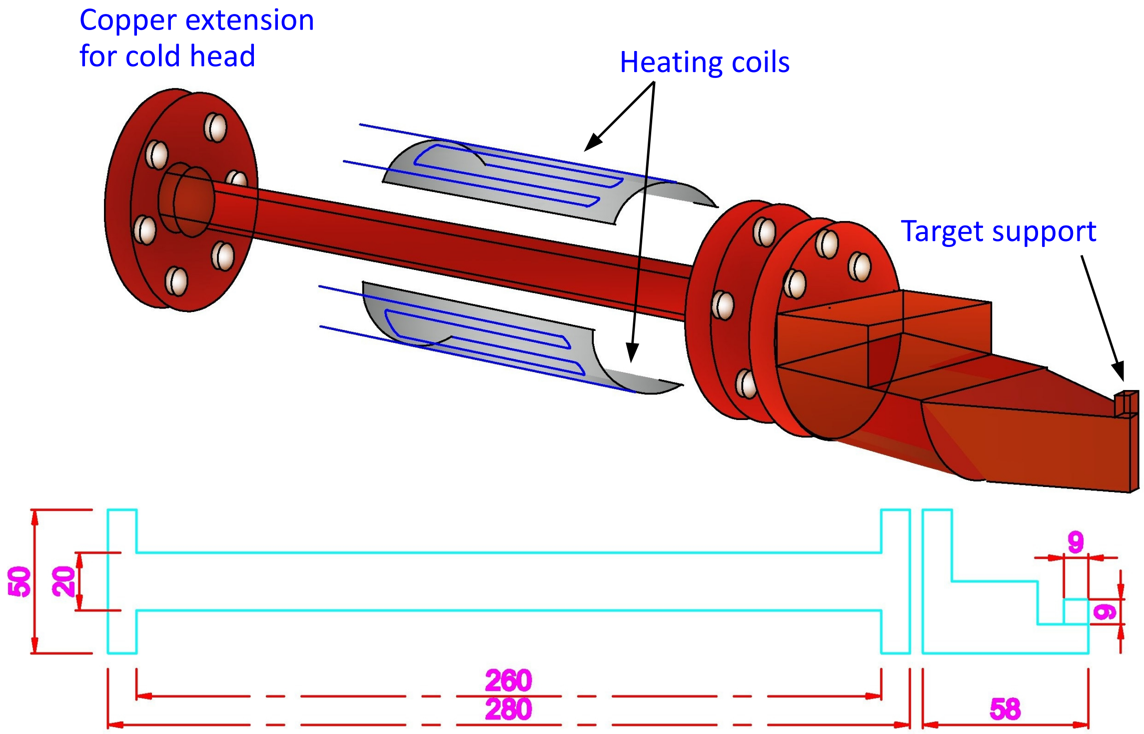

Figure 4.13: Accessories to install cold head at the Z6 target chamber.

The addition of the extra length did not change the cooling capacity but the time to reach the lowest temperature which is 6 K for the present case. The typical cooling time with copper extension is about 90 minutes. The extension also needed to be protected from the ambient radiations for which a cylindrical aluminium shield along with an adaptor was joined to the existing 50 K shield. For temperature control the heating element is mounted on metallic shells which can be fixed on the copper finger. Spatial distortions are quite likely owing to alignment of lasers and diagnostics. Moreover contraction resulting from cooling may also change the position of the target. In order to compensate these distortions, bellows have been used to mount the cold head. The growing chamber has been fixed with a three dimensional manipulator. The manipulator comprises of three linear stages[9] so that the growing chamber can be moved to the boundary of the chamber and hence prevent hindrance to diagnostics.

---

[9] Micos VT-80

5 Experimental Results and Discussions

The possibility to fabricate cryogenic targets at the Z6 experimental area for laser plasma interaction experiments has been realized using the experimental set up described in previous chapters. Two separate experiments have been performed, one with cubic-shaped nitrogen crystals and the other with thin foil like deuterium targets. For plasma generation the nitrogen crystals have been irradiated with the *nhelix* laser. The deuterium crystals have been irradiated from both sides using the *nhelix* and PHELIX lasers and the UNILAC ion beam has been used to study beam plasma interactions. The results of these experiments are described in the following sections.

5.1 Laser induced nitrogen plasmas

For the first experiments, nitrogen targets have been selected mainly because the freezing point (63 K) is relatively easy to manipulate, and reproducible targets can be fabricated within few minutes. The crystals have a cubic shape with fixed length and width each equal to 90 mm, whereas the height varies from 40 – 60 mm depending upon the growing time. The *nhelix* laser beam (50 J ; 10 ns) has been focused to a focal spot of 1 mm at one of the planar sides of the target, by a combination of a phase plate and a lens doublet. The diagnostics included a Wollaston interferometer for free electron density measurements, a fast shutter CCD camera[1] and a streak camera[2]. The orientation of the target with respect to the irradiating laser and positions of the diagnostics is depicted in figure 5.1. The fast shutter CCD camera captures images of the plasma expansion. One such image taken with 25 ns exposure time is shown in figure 5.2.

5.1.1 Visible streak camera data

The working principle of a streak camera has been described in section 3.4.2. A visible streak camera placed perpendicular to the plasma plume expansion, records plasma images for a certain short duration, the so called streak time. The images can be adjusted to temporal and spatial axes according to calibrated equivalence between the number of pixels and the time as well as position. Figure 5.3 shows an image of the laser induced nitrogen plasma captured by streak camera . From the values of time and position along horizontal and vertical direction respectively, the glowing plasma velocity can be calculated. This is 90.8 km/s for the present case. The temperature can be calculated using equation (2.6). It turns out to be 172 eV.

---

[1] DiCAM Pro PCO AG Germany

[2] Streak camera C2830 Hamamatsu Photonics Japan

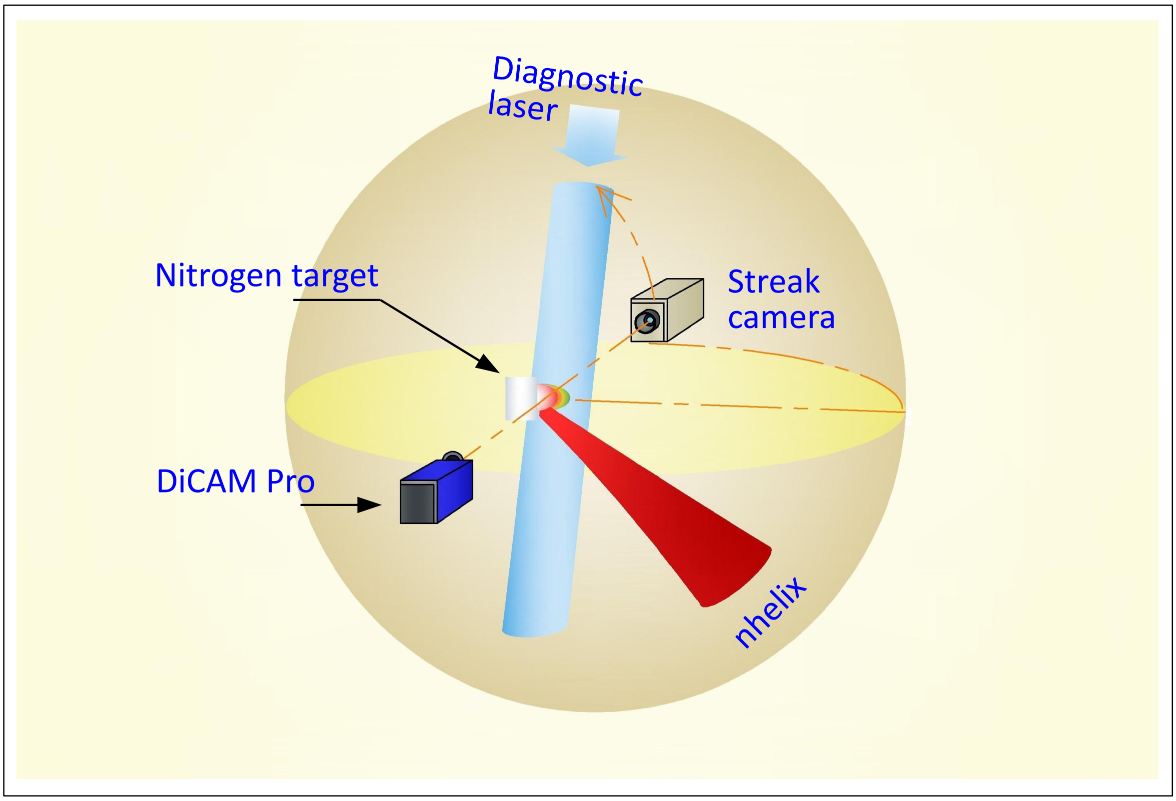

Figure 5.1: View of the nitrogen target placed at the centre of the Z6 chamber along with diagnostics.

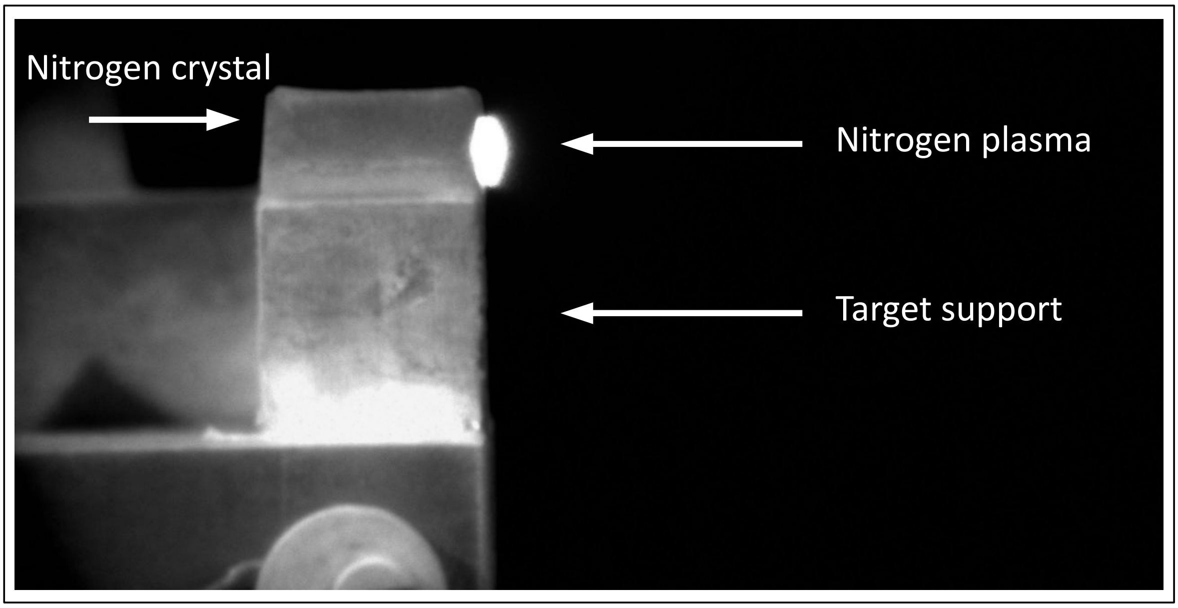

Figure 5.2: Image of the laser induced nitrogen plasma taken by the fast shutter CCD camera.

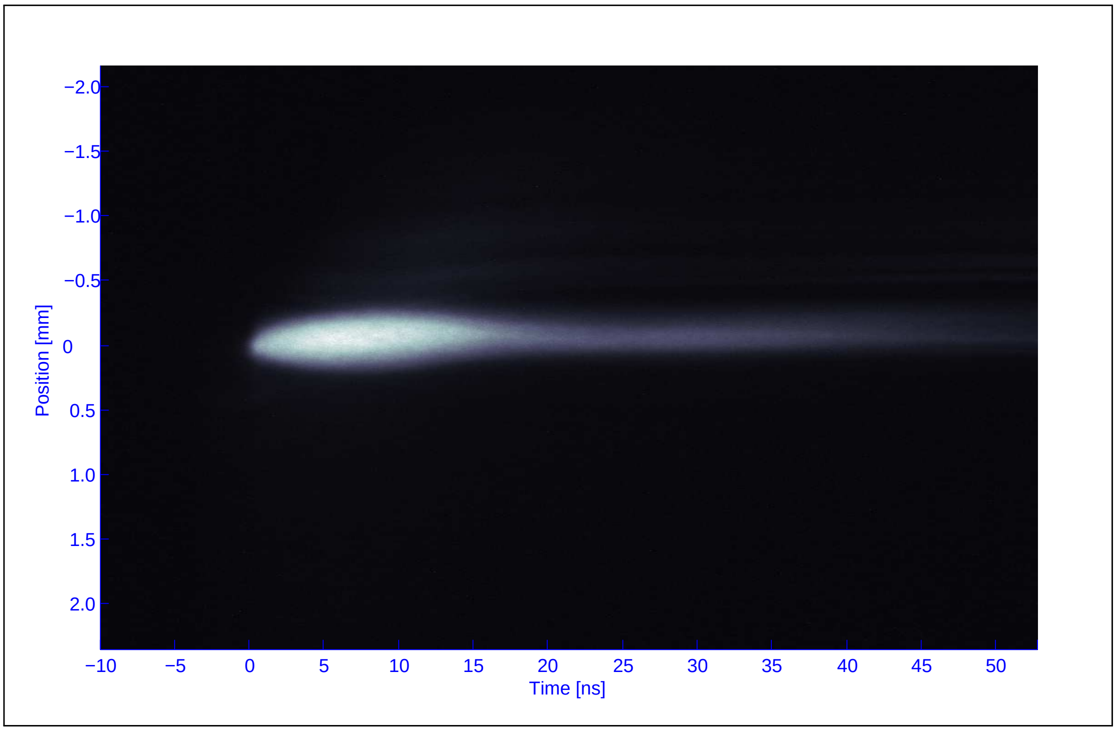

Figure 5.3: View of the nitrogen plasma taken by the streak camera.

5.1.2 Interferometric measurements

The knowledge of plasma parameters like temperature and density is essentially significant for the understanding of laser produced plasmas, particularly beam-plasma interaction phenomena. In order to measure quantitative and spatially resolved free electron density, optical interferometry plays an important role. In the present work a Wollaston interferometer has been used to determine the electron density. The detail of operating principles and experimental setup is given in sections 2.6 and 3.4.1.

In order to calculate the fringe shift a reference of undisturbed fringes is always needed. Usually this is done by using a large field of view of the camera so that there is always an area without plasma and thus undisturbed fringes. Alternatively, a more practical method which is used in this experiment is to take every time a reference image without plasma and a separate image for recording the fringe shift i.e. with plasma. From comparison of both images the fringe shift and hence the electron density can be calculated. A reference image with straight fringes as well as a plasma image showing the change in fringes is shown in figure 5.4.

First the raw image is masked. The target is on the left-hand side of the image. The laser comes from the right, thus the plasma will expand from the target to the right hand side. Every area where there no fringes can be discerned has to be masked, including the area where the target support is located. Then the image is processed in order to enhance the contrast between fringes. From these images the shift appearing in the fringes with respect to their original posi-

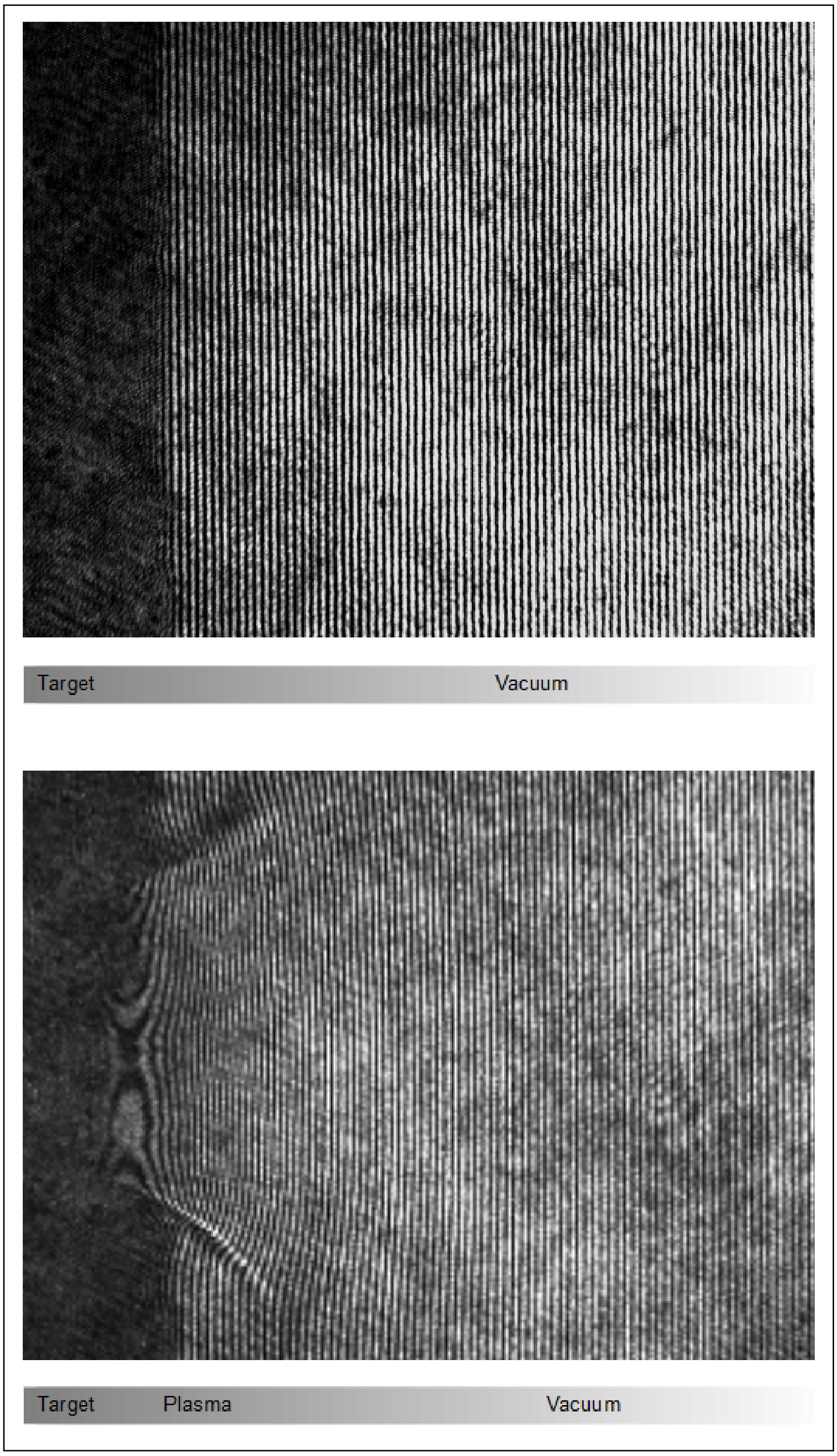

Figure 5.4: Reference image and the image taken during laser irradiation as used for phase change measurements.

tion allows the determination of the phase change with the help of a computer program which has especially been written for this purpose [38]. Further, it can also be used for automatic computation of the electron density. The algorithm is based on the principle of *Abel inversion* which implies the assumption of a cylindrical symmetry of the expansion of the plasma.

Most of the interesting phenomena in the plasma are limited to very short time scales, particularly from the beam-plasma interaction point of view the first 20 seconds are important. Therefore, the variation of the electron density with respect to the time needs to be estimated. The Wollaston interferometer can measure the plasma density only for a certain instant of time. However, an adjustment of the timing between heating and the diagnostic pulse helps to reveal the plasma electron density at different instants of plasma expansion. In figure 5.5 the timing of heating and diagnostic pulse is depicted. A comparison of the obtained values helps to analyze the time evolution of the density although the experimental conditions are not perfectly reproducible due to laser energy fluctuations and target quality. In figures 5.6 – 5.9 the measured electron densities and density profiles along the directions parallel as well as perpendicular to the target surface have been shown.

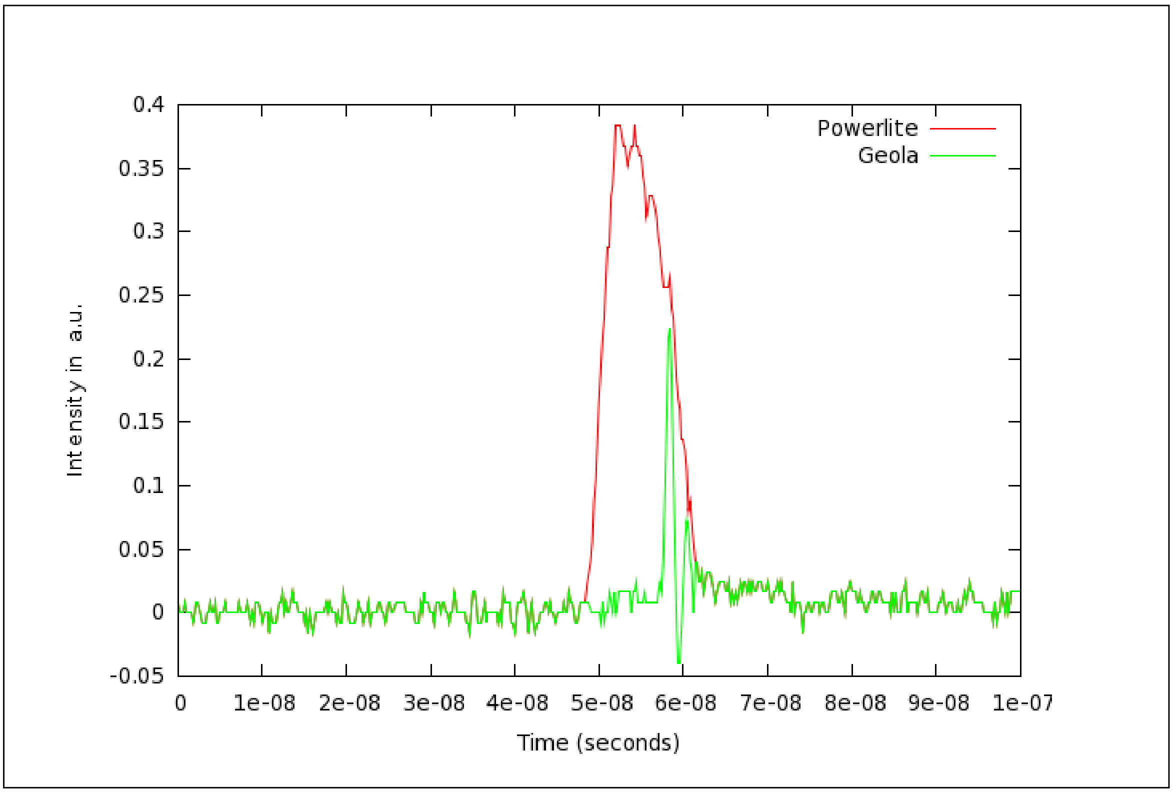

Figure 5.5: Oscilloscope signals of the heating and diagnostic laser pulses.

An imperative condition for the energy loss experiments is to prevail homogeneous plasma at least within the ion beam cross-section. For this, the size of laser focus would be larger than the ion beam. Practically an ion beam can only be focused to few millimetres, however an aperture can be used to reduce the beam size down to 500 μm. A further reduction of the size makes no sense as ion beam intensity at the detector would be too low. The analyses of the electron density profiles taken parallel to the target surface at 0 μm and 500 μm manifest a considerable decrease of the electron density. Therefore targets with cm-dimensions are not

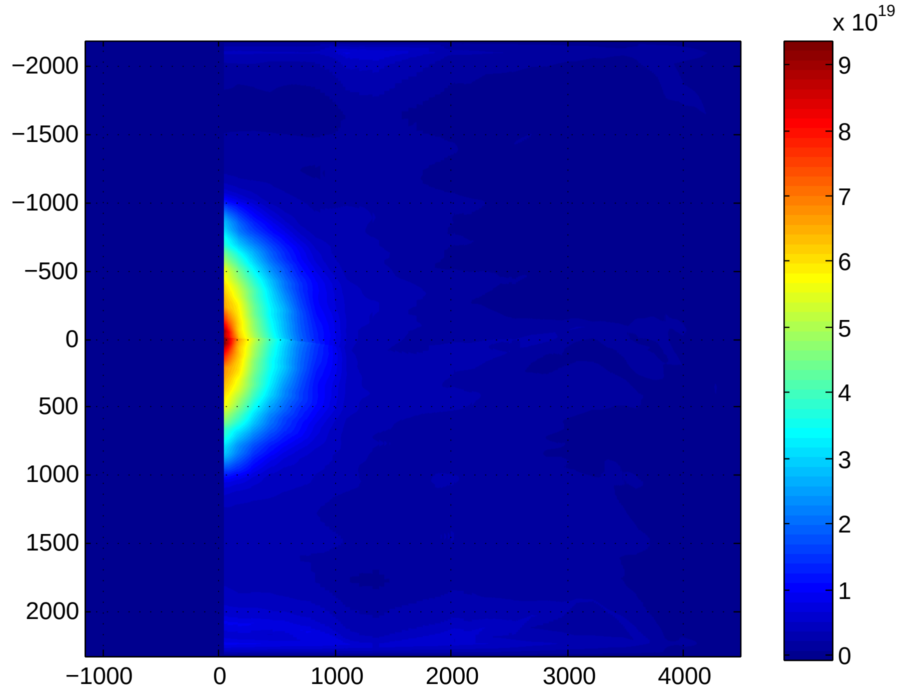

Figure 5.6: Electron density distribution of the nitrogen plasma 5 ns after commence of laser heating. Space in $\mu\mathrm{m}$ - colorbar shows density in $10^{19}\mathrm{cm}^{-3}$.

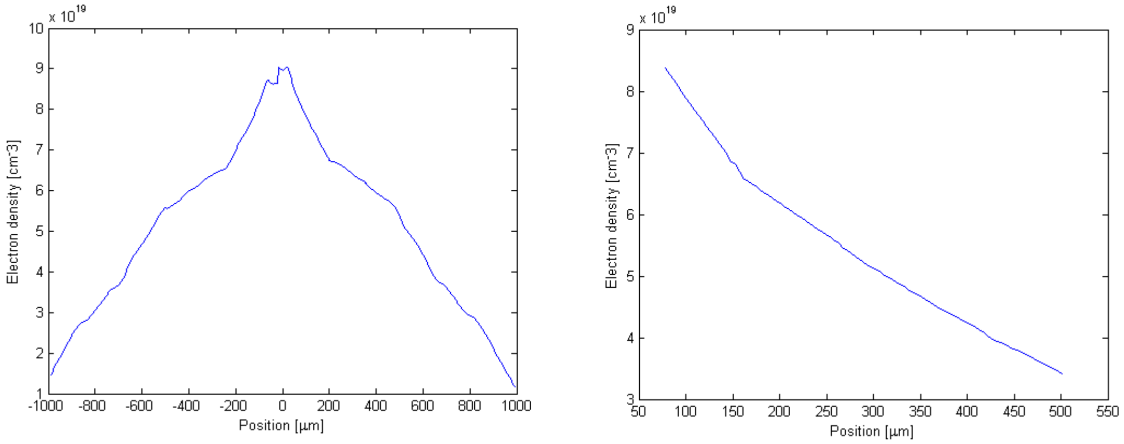

Figure 5.7: Electron density profiles of the nitrogen plasma taken along (left) and perpendicular (right) to the target surface.

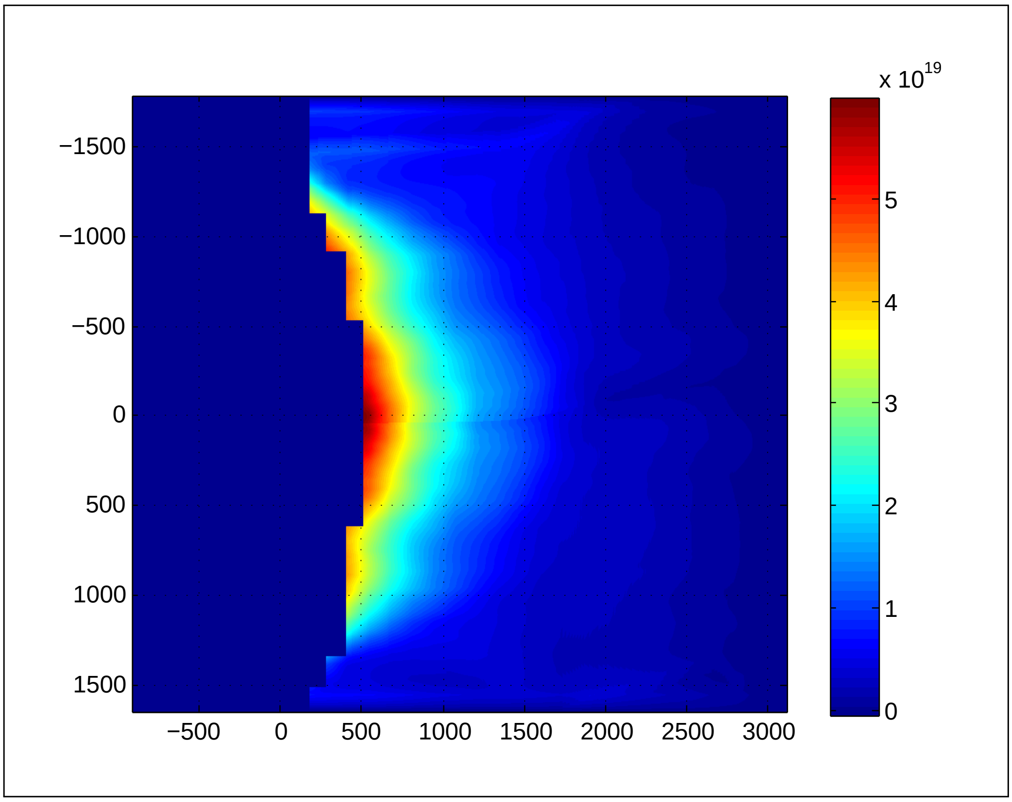

Figure 5.8: Electron density distribution of the nitrogen plasma 10 ns after commence of laser heating. Space in μm - colorbar shows density in $10^{19}\mathrm{cm}^{-3}$.

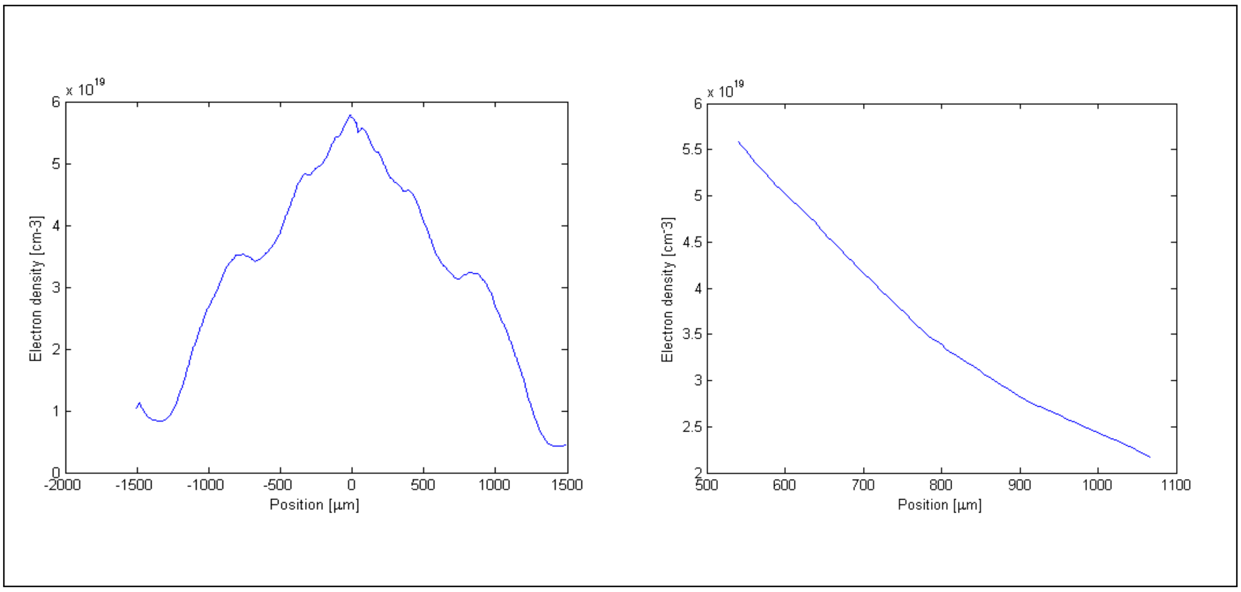

Figure 5.9: Electron density profiles of the nitrogen plasma taken along (left) and perpendicular (right) to the target surface.

suitable for energy loss experiments. At the Z6, thin carbon foils (1.75 μm) have been used for energy loss measurements. Therefore, thin foil like deuterium targets have been fabricated at the Z6 for energy loss experiments.

5.2 Thin deuterium targets for energy loss experiments

Cryogenic hydrogen or deuterium targets are quite interesting for they allow the generation of laser plasmas with a high degree of homogeneity, thus allowing measuring the ion energy loss under well defined conditions in fully ionized plasma [60]. For the energy loss experiment deuterium targets have been selected, as they are easy to grow relative to hydrogen targets. The necessary arrangements for the development of thin deuterium targets at the Z6 have been described in section 4.10. A view of the target position, the direction of the ion and laser beams as well as the diagnostics is shown in figure 5.10.

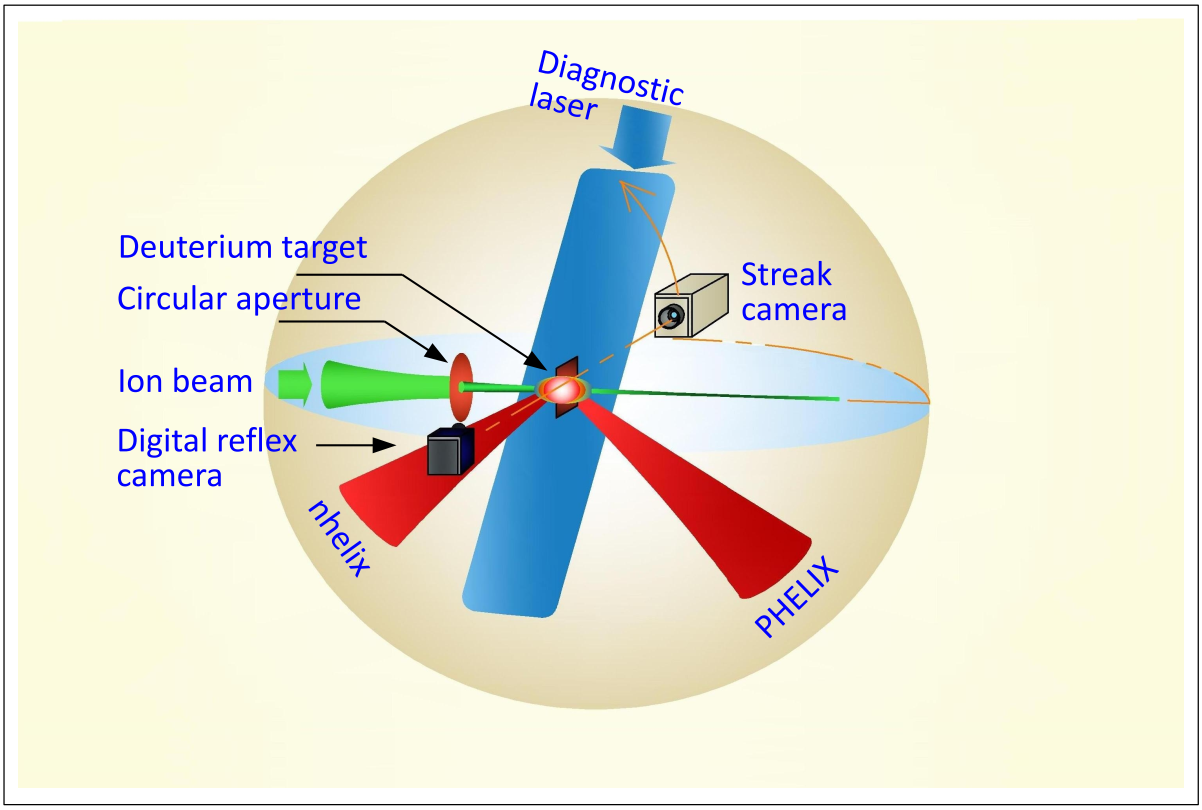

Figure 5.10: Experimental arrangement for thin deuterium targets.

For plasma generation the target is heated from both sides with the *nhelix* and PHELIX laser beams (50 J in 10 ns @ 1064 nm; 1053 nm). An argon beam (^{36}Ar, 4.0 MeV/u) with 36 MHz micro structure has been used to characterize the target thickness. The electron density measurements have been performed using a Wollaston interferometer. Figure 5.11 shows an image of the plasma taken by a digital reflex camera.

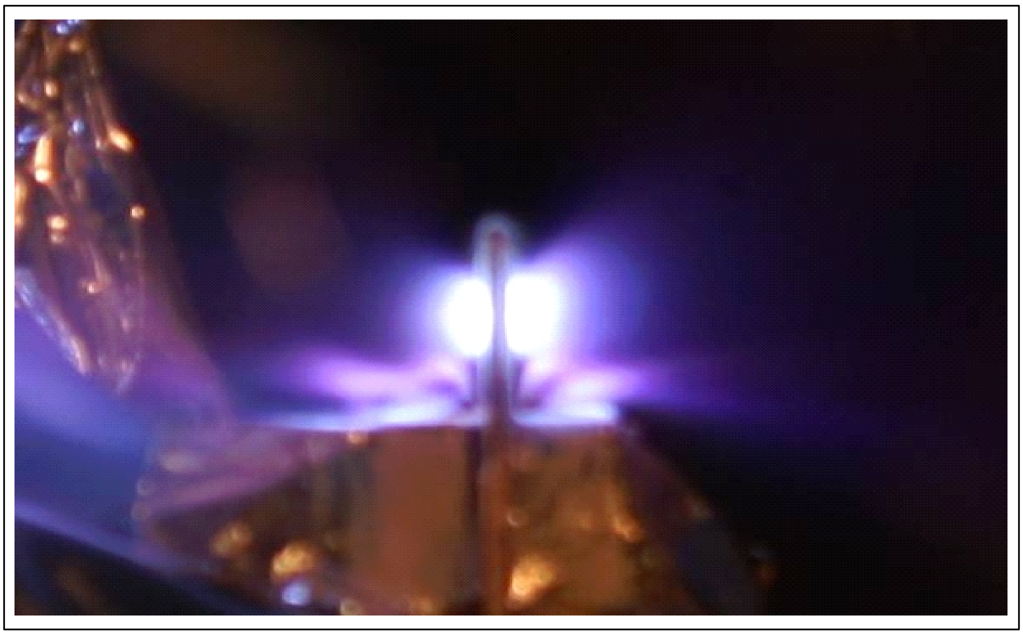

Figure 5.11: Image of the laser induced deuterium plasma taken by a single-lens reflex camera.

5.2.1 Interferometry

The method for measurement of electron density is almost the same as for nitrogen targets with an exception that here the target is heated from both sides. Moreover, the target is supported by a thin copper foil which is immersed into the target support. This target support hinders part of the interferometric measurements and damages their symmetry of the measurements. The problem can however be addressed by masking the irrelevant portion of the image or processing half of the image and then mirroring it around the axis. The resulting electron density is shown in figure 5.12.

5.2.2 Interaction with ion beam

For energy loss measurements the time of flight method is used, details of which have been described in section 3.5. For these measurements one needs a reference signal that is compared with the signal obtained when the beam interacts with the plasma. The target has initially a thickness of $\approx 500\,\mu$m, however the appropriate thickness for energy loss measurements is 50 μm or less. Therefore, the target has been regularly irradiated with the ion beam to examine the possibility of the beam passage through the target. Since the targets have been grown in a vacuum chamber, they sublimate and their thickness drops. The moment the crystal reaches the desired thickness, a synchronous irradiation of the target with ion and laser beams is to be done. This needs few minutes for preparation. However, during this time the target being very thin, appears vulnerable for further sublimation and there has not been any chance to shoot the

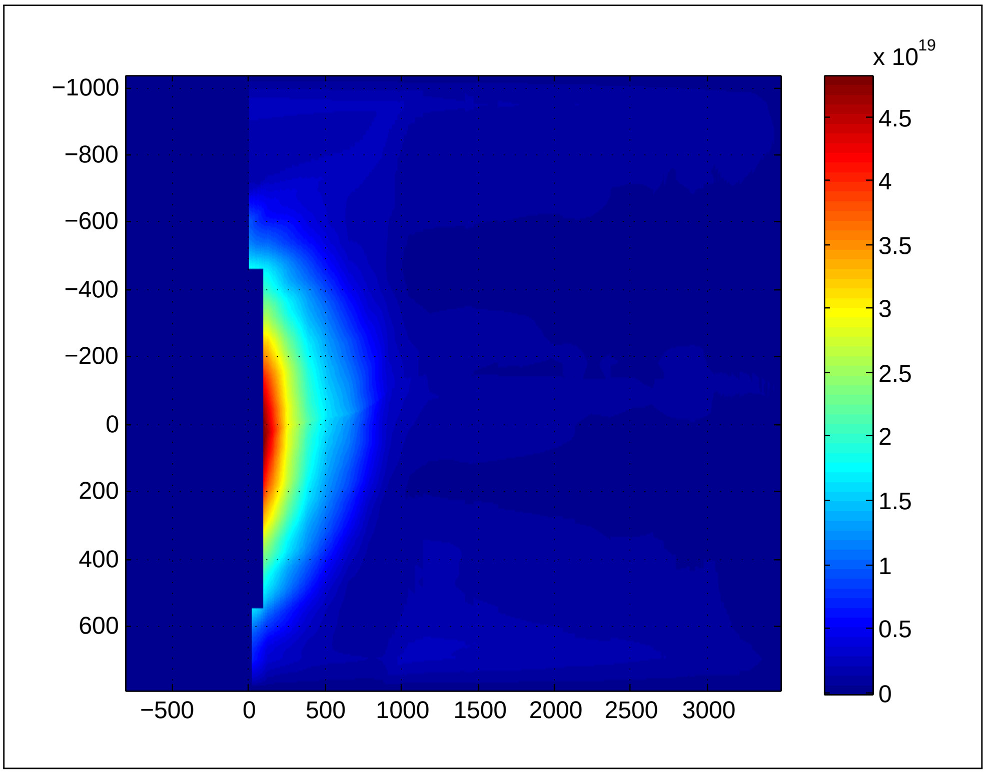

Figure 5.12: Electron density distribution of the deuterium plasma 10 ns after commence of laser heating. Space in μm - colorbar shows density in $10^{19}\mathrm{cm}^{-3}$

target for useful measurements. Therefore, an external source to control the target thickness e.g. infrared heating or electron sputtering is necessary. There is also a need to develop a method for the target thickness measurement in addition to the ion beam. An electron source has been used to determine the target thickness off line. The details of this method can be seen in [43]. With the help of this method target thickness ranging ($5\,\mu\mathrm{m} - 15\,\mu\mathrm{m}$) can be measured with a precision of 12%.

5.3 Conclusions

Based on the experimental observations as described in the previous sections, one may conclude that cryogenic targets can be fabricated and adapted to the Z6 experimental setup. As a first attempt nitrogen crystals have been used for laser plasma experiments. Good quality, reproducible targets with cm-dimensions have shown interesting results, however they are not suitable for energy loss measurements. Thin foil-like deuterium targets, having a thickness of few tens of microns and a large transverse size have been fabricated for energy loss experiments. The ion beam can pass through these targets which suggests the possibility to realize the energy loss measurements. However there is a need for an improved control of the target thickness and to improve the characterization of the targets.

6 The Lowering of the Ionization Energy of Dense Hydrogen-like Carbon Plasmas

Basic ideas about the role of energy shifts on the properties of the dense plasmas have been studied for the last three decades [15, 21]. The advent of high intensity short duration lasers, however, turned the generation of hot dense plasma to such a scale of densities where it becomes nonideal. For these plasmas, the mean interaction energy of charged particles may be of the order of their kinetic energy and various features of the system deviate essentially from those of low density plasmas. The physical properties of such plasmas are determined by the Coulomb interactions between the charged plasma particles. The most important physical effect of these interactions is the lowering of the border between the discrete and the continuous energy spectrum, thus the lowering of the effective ionization and excitation energies [61].

Hydrogen-like particles, that means hydrogen itself, but also one-fold ionized helium and five-fold ionized carbon atoms play an important role in astrophysics and are of interest in connection to future laboratory experiments. Thus, for instance, a careful recalculation of the partition functions of dense charged carbon plasmas is necessary. This is implemented by calculating the partition function taking into account density-dependent and temperature-dependent energy levels of the carbon ions. Concerning the relative energy level shifts by increasing plasma density, we start the investigation based on Jacobi-Padé approximations. In these approximations, the shifts are a function of the energy eigenfunctions of the systems in momentum space. But applicable expressions of the eigenfunctions, even in case of hydrogen-like particles, are generally known only in spatial space. Thus the solutions in spatial space have first to be transformed into the momentum space for as much energy eigenstates as possible. This is done above all numerically. For some main quantum numbers, analytical results are found, which help to check the computer program. In comparison to former works of Ebeling et al. [17] the dependence of the relative energy level shifts on the orbital angular momentum quantum number is also studied.

The following sections will elaborate relevant plasma properties as well as the necessary terminology and methodology to develop a mathematical model. Starting from basic ideas and some physical effects, the construction of the Jacobi-Padé approximation along with limits of application will be described. Finally, mathematical expressions developed for eigenvalues in momentum space and their use to ascertain energy shifts will also be discussed.

6.1 Relevant plasma properties

The plasma states exist in many varieties and their characterization extends to a large range of parameters. The density-temperature regime in which matter behaves as an ideal and non-ideal (strongly coupled) plasma is shown in figure 6.1. Owing to the strongly different attitudes of the plasma state and their dependence on the considered parameter range, it is worth to mention relevant properties for their theoretical description.

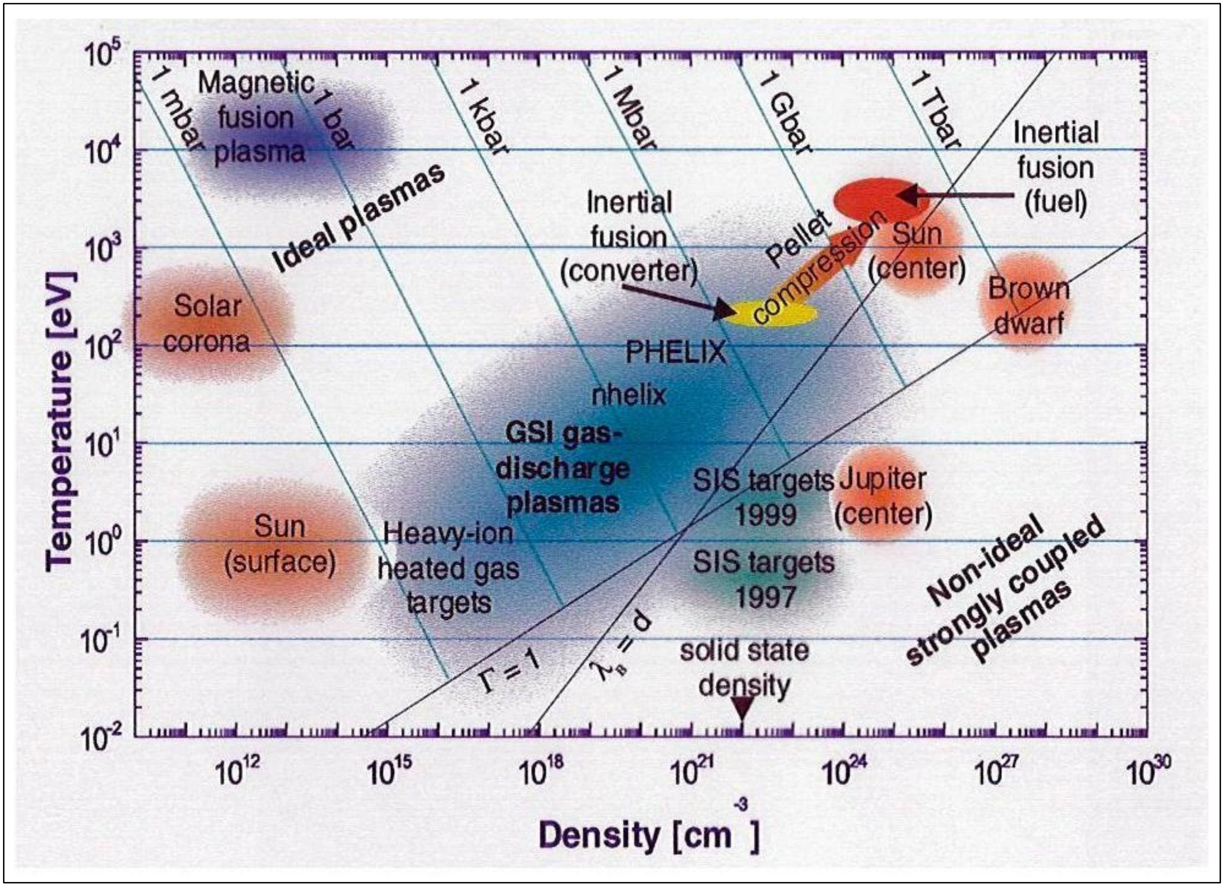

Figure 6.1: Natural and laboratory plasmas in the density-temperature plane [62].

6.1.1 Inter-particle interactions and ideality criteria

At low densities, a low temperature, partially ionized plasma can be regarded as a mixture of ideal gases of electrons, atoms and ions. Electrostatic interactions between individual particles are occasional and relatively rare events. Such plasmas are termed weakly coupled. Analogous to classical thermodynamics, the plasma is approximately treated as an ideal gas of charged particles, that is, a gas that can have a charge density and electric field but in which no two *discrete* particles interact. The potential energy of the particles is very small compared to the average kinetic energy.

With an increase in density, the mean distance between the particles decreases and they start spending even more time interacting with the surrounding particles. Under these conditions, the mean energy of the particle interactions increases. When this energy becomes comparable with the mean kinetic energy of the thermal motion, the plasma is called non-ideal. The plasma parameter

$$\Gamma = \frac{1}{4\pi n_e r_D^3} \quad .$$

describes the degree of nonideality of the plasma. Here r_D is the Debye radius. In figure 6.1 the line $\Gamma = 1$ separates ideal and non-ideal plasmas.

6.1.2 Degeneracy

In case of classical equilibrium plasmas, the distribution function is the well known Boltzmann-distribution function

$$f(p) = e^{-\beta(\frac{p^2}{2m}-\mu)} = \tilde{z} e^{-p^2/(2mk_BT)}. \tag{6.1}$$

Here, k_B is the Boltzmann constant, μ is the chemical potential, $\tilde{z}$ is the fugacity and $\beta = 1/k_BT$.

The fugacity and the chemical potential are given by

$$\tilde{z} = \frac{n\Lambda^3}{2s+1}, \qquad \mu = k_BT \ln\left(\frac{n\Lambda^3}{2s+1}\right), \tag{6.2}$$

where Λ is the thermal wavelength defined by

$$\Lambda = \left(\frac{2\pi\hbar^2}{mk_BT}\right)^{1/2}. \tag{6.3}$$

The properties of dense plasmas are not described by the simple relationships of the theory of ideal gases and plasmas. The quantum character of the plasma particles plays a decisive role and cannot be neglected. The first modification is the use of the wave function "$\psi - function$" instead of the trajectory to characterize the momentum of the plasma particle. Secondly, the behaviour of a many particle system is essentially determined by the spin statistics theorem. The state vectors of Bose particles are symmetric and those of Fermi particles are antisymmetric. We can roughly subdivide plasmas into non-degenerate plasmas if $n\Lambda^3 << 1$, and strongly degenerate plasmas if $n\Lambda^3 >> 1$. It is worth to be mentioned here that the degeneracy influences the chemical potential and hence degeneracy has a certain effect on ionization energies.

6.1.3 Partition function

In statistical physics, the partition function is an important tool that encodes the statistical properties of a system in thermodynamic equilibrium. Based on statistical collectivity and the corresponding states variables, the partition function helps to develop all thermodynamic relations. By definition it is given by

$$U_i(T) = g_{(i,s)} \sum_s \exp\left(-\frac{E_{i,s}}{k_B T}\right). \tag{6.4}$$

The sum is taken over all possible energy states $E_{i,s}$ of the $i - th$ plasma particle. The factor $g_{i,s}$ is the statistical weight of the states of the particle with energy $E_{i,s}$, while i, s describe the possible energy states. The simple illustration for the partition function is just what its name implies: a function related to the specific way particles are “partitioned” among the various energy states accessible to them.

6.2 Saha equation

In the case of both increasing temperature and growing plasma density, the degree of plasma ionization gets larger. To determine the degree of ionization one can study the free energy of the plasma as function of volume, density and temperature. There the ionization process may be described by a chemical reaction between the atom (ion with charge $q_0 = ie$) and the ion with elementary charge e (ion with charge $q_i = (i+1)e$) and an electron with charge $q_e = e$. In thermodynamic equilibrium, the free energy as a function of particle numbers must have a minimum, or what is equivalent, the sum of the chemical potentials of the reactants is equal to the sum of the chemical potentials of the products of the reaction i.e.

$$\mu_0 = \mu_i + \mu_e \tag{6.5}$$

The chemical potential μ_a may be expressed as sum of the part describing particles in ideal systems μ_a^{id} and the additional interaction part μ_a^{int},

$$\mu_a = \mu_a^{id} + \mu_a^{int} \tag{6.6}$$

The ideal part may be expressed by [15]

$$\mu_a^{id} = \mu_a^0(T) + k_B T \ln n_a \tag{6.7}$$

$$\mu_a^0 = -k_B T \left(\ln \left[\frac{U_a(T,V)}{\Lambda_a^3} \right] \right) \tag{6.8}$$

where Λ_a is the thermal wavelength while U_a is the partition function given by equations (6.3) and (6.4) respectively.

The energies E_s are counted from the zero energy of a free electron at rest, that means all binding energies of the atoms are negative. g_s is the statistical weight of the electron state with energy E_s. Λ_a designates the thermal wavelength of the particle a, $\Lambda_e \approx 7.45.10^{-8} m/\sqrt{T}$, and $\Lambda_{12c} \approx 5.04.10^{-10} m/\sqrt{T}$. The combination of equations (6.5- 6.8) gives

$$\frac{n_0}{n_i n_e} = K(T,n_e,n_0) = \frac{U_0}{U_i U_e} \frac{\Lambda_i^3 \Lambda_e^3}{\Lambda_0^3} \exp\left[(\mu_i^{int}(T,n_e,n_0) + \mu_e^{int}(T,n_e,n_0) - \mu_0^{int}(T,n_e,n_0))/k_B T \right] \tag{6.9}$$

For the free electron at rest $E = 0, U_e = 2$. And in case of hydrogen atoms, that means at total degeneration of the energy levels with respect to the spin quantum number and the magnetic quantum number, one has [15]

$$U_0(T,n_e,n_0) = (2s_e + 1) U_i(T) \sigma(T,n_e,n_0), \sigma(T,n_e,n_0) = \sum_{n,l} (2l+1) \exp(-E_{nl}(T,n_e,n_0)/k_B T) \tag{6.10}$$

Then the mass action law is

$$\frac{n_0}{n_i n_e} = \frac{U_e}{2} \frac{\Lambda_i^3 \Lambda_e^3}{\Lambda_0^3} \sum_{n,l} \sigma(T,n_e,n_0) \approx \Lambda_e^3 \sum_{n,l} \sigma(T,n_e,n_0) \tag{6.11}$$

6.3 Partition function cutoff and lowering of the ionization energy

It is quite evident from the expression of the partition function (equation 6.4), that for an isolated atom the sum U diverges, since there exists an infinite number of energy states s, and U becomes lower when E_0, s is restricted to the ionization energy $E_{1,0}$. The situation for a gas with finite density is different from the situation of an isolated atom. In this case, the physical effects appear in such a way that the sum is only extended over finite numbers of terms.

With ever growing excitation, the mean distance between the excited electron and the nucleus also grows and becomes infinite when the excitation energy balances the ionization energy. For a finite density, however, the expansion of a single atom is limited and therefore the partition function cutoff is to be realized after certain finite numbers of terms. Moreover, interactions with the surrounding plasma have to be treated kinetically which means that energy shifts are dynamic effects. The fluctuations of micro-electric fields ultimately lead to the broadening of energy levels. If the width of the higher states tends to be equal to the term-distance then the excited electron cannot be exactly assigned a term.

The cutoff of the partition function can be assumed by introducing the weighting factor ω_s in U,

$$\omega_s = \begin{cases} 1, & \text{if } s \leq s_{max} \\ 0, & \text{otherwise.} \end{cases} \tag{6.12}$$

It can easily be seen from the above expression that s_{max} must be elected small for high temperature and pressure. A further option is the Planck-Larkin approximation with [15]

$$\omega_s = 1 - \exp\left(\frac{E_s}{k_B T}\right) + \frac{E_s}{k_B T}\exp\left(\frac{E_s}{k_B T}\right), \tag{6.13}$$

which results into

$$K(T) = \Lambda^3 \sum_{s=1}^{\infty} s^2 \left(\exp\left(-\frac{E_s}{k_B T}\right) - 1 + \frac{E_s}{k_B T}\right). \tag{6.14}$$

These approximations are based on the theory of second virial coefficients [21]. Another fact is that the long-range Coulomb potential of a singly charged particle is modified through collective effects and the effective field can be described in first approximation by the Debye-potential.

$$\phi(r) = \frac{q}{4\pi r} e^{\frac{-r}{r_D}}.$$

where r_D is the Debye radius.

For the partition function apparently the shift of the energy levels is particularly displaced in the upper part of the continuum where the atom holds only a limited number of energy levels. One of the clear consequences here is the lowering of the ionization energy depending on the temperature and density of the plasma. The chemical potential μ of the plasma which consists of an ideal part and an interaction part $(\mu_K^*)^{int}$ is given by

$$\mu_K^* = \mu^0 + k_B T n_K^* + (\mu_K^*)^{int}.$$

Here the interaction part $(\mu_K^*)^{int}$ is interesting for the lowering of the ionization energy. In Debye approximation, the interaction part is given by $(\mu_K^*)^{int}$ [15]

$$(\mu_K^*)^{int} = -\frac{e_K^2}{2r_D(1+\frac{\Lambda}{8r_D})}.$$

6.4 Energy levels of individual hydrogen-like atoms

The energy of an electron moving in the central field of a non-moving point charge equals

$$E_n = -\frac{m_r e^4 Z^2}{2(4\pi\epsilon_0\hbar)^2 n^2} = -\frac{hZ^2}{n^2} R_\infty \tag{6.15}$$

$$R_\infty = \frac{m_e e^4}{8ch^3\varepsilon_0^2} = \frac{\alpha^2}{2\lambda_{C,e}}, \qquad \alpha = \frac{e^2}{2c\epsilon_0 h} = \frac{1}{137}, \qquad \lambda_{C,e} = \frac{h}{m_e c} \tag{6.16}$$

In the case of an electron moving in the electric field of an ion of finite mass, one has to substitute R_∞ by

$$R_i = \frac{R_\infty}{1 + m_e/m_i} \tag{6.17}$$

6.5 Shifts of the energy levels and ionization gap

For isolated systems of pairs of charged particles, the bound state levels are given as the eigenvalues of the corresponding Schrödinger equation. If, however, the bound pair is embedded into a plasma, the situation is much more complicated due to the influence of the surrounding plasma on the quantum states of the pair. The embedding into the plasma gives rise to four important physical effects:

- Both the electron and the nucleus are sitting in a potential hole which is produced by polarization of the plasma. This gives rise to the so-called self-energy effects.
- The bare coulomb forces are screened by the plasma. This leads to Debye-type interaction laws and to corresponding shifts, which are termed as Debye shifts.
- The electron orbiting around the nucleus is not allowed to occupy any state since the Pauli principle leads to several restrictions. States which are already occupied by plasma electrons have to be avoided in all interactions and scattering processes. This leads to the so-called Pauli shifts which are of special importance for the excited states.
- Due to the collision of the bound state electrons with the surrounding plasma, the bound state of a pair negatively and positively charged particles embedded into a plasma have a finite life-time.

In order to take these effects into account we follow here the approach proposed by Kilimann et al. [63]. For a non-degenerate plasma which consists of electrons and ions of different charges, the number densities of free electrons n_e , singly charged ions n_1, doubly charged ions n_2 etc. as well as the number densities of free bare nuclei n_Z are given as

$$n = \sum_{z=0}^{Z} n_z \tag{6.18}$$

with n being the total density of nuclei. From electro-neutrality follows

$$n_e = \sum_{z=0}^{Z} z n_z \; . \tag{6.19}$$

A key quantity is the reciprocal Debye radius which is given by

$$r_D^{-1} = \kappa = \left\{4\pi\beta \left[n_e + \sum_{z=1}^{Z} n_z z^2 \right] e^2 \right\}^{1/2}, \qquad \beta = \frac{1}{k_B T} \tag{6.20}$$

The three main contributions to the energy level shift are the self-energies of electrons (Δ_e), ions (Δ_z), and the Debye shift (Δ_k^{z-1})

$$\tilde{E}_k^{z-1} = E_k^{z-1} + \Delta_e + \Delta_z + \Delta_k^{z-1} \tag{6.21}$$

where

$$E_k^{z-1} = -\frac{m_r \eta^2 Z^2}{2\hbar^2 n^2}, \quad \eta = \frac{e^2}{4\pi\varepsilon_0}, \quad m_r = \frac{m_e m_i}{m_e + m_i}.$$

$$\Delta_e \approx -\frac{1}{2} e^2 \kappa. \tag{6.22}$$

$$\Delta_z \approx -\frac{1}{2} z^2 e^2 \kappa. \tag{6.23}$$

$$\Delta_k^{z-1} =< (V_{ei}^{eff} - V_{ei}) >_k . \tag{6.24}$$

The Debye shift of the energy level k is estimated here as the expectation value of the difference between Coulomb potential and Debye potential in the quantum state k:

$$\Delta_k^{z-1} = z e^2 < (r^{-1} - r^{-1}\exp(-\kappa r)) >_k \tag{6.25}$$

$$= z e^2 \begin{cases} \kappa - \frac{1}{2}\kappa^2 < r >_k + \frac{1}{6}\kappa^3 < r^2 >_k + ..., & \text{if } \kappa a_B << 1 \\ \\ < r^{-1} >_k, & \text{if } \kappa a_B >> 1 \end{cases}$$

where $< r^n >_k$ are the expectation values of r^n for the orbit k corresponding to the eigenstate k. For the ground state of an ion carrying (z-1) protonic charges, one has

$$\tilde{E}_{1n}^{z-1} = E_{1n}^{z-1} - \frac{1}{2}(z-1)^2 e^2 \kappa. \tag{6.26}$$

As we see the ground state shifts cancel for singly charged ions. However for excited states the parameter

$$\kappa < r^n >_k \tag{6.27}$$

is large and cannot be neglected. For an estimate we use the Jacobi-Padé approximation (Ebeling et al. [64]),

$$\Delta_k^{z-1} = z e^2 \kappa \frac{1 + a_k^z \kappa}{1 + b_k^z \kappa + c_k^z \kappa^2} \tag{6.28}$$

where the coefficients are given by

$$a_k^z = \frac{\{\frac{1}{4} < r >_k^2 - \frac{1}{6} < r^2 >_k\} < r^{-1} >_k}{D}, \tag{6.29}$$

$$b_k^z = \frac{1}{2} < r >_k + a_k^z, \tag{6.30}$$

$$c_k^z = \frac{a_k^z}{< r^{-1} >_k}, \tag{6.31}$$

$$D = 1 - \frac{1}{2} < r >_k < r^{-1} >_k \tag{6.32}$$

From these formulae we may conclude that the Debye shift can be neglected for high quantum numbers. Therefore, we get for the limit to the continuum

$$\tilde{E}_{\infty}^{z-1} = \Delta_e + \Delta_z \approx -\frac{1}{2} e^2 (1 + z^2) \kappa . \tag{6.33}$$

In contrast to the ground state level, the continuum edge is strongly density dependent and there is no compensation even for z = 1 (hydrogen like ions).

Taking into account the numerical observation from Rogers et al. [65] we discuss another approximation given by Kilimann et al. [66] considering that a level k disappears at certain critical value of the relation of the Bohr radius to the Debye radius, which is denoted by

$$X_k = \left[\frac{a_0^z}{r_D} \right]_{crit} . \tag{6.34}$$

In the following we shall consider only hydrogen-like levels which are characterized by a main quantum number n and the orbital quantum number l. Then the condition of the level merging requires that the gap

$$I_{nl}^{z-1} = |E_n^{z-1}| - \Delta_{nl}^{z-1} = 0 \tag{6.35}$$

disappears at $\hat{\kappa} = X_{nl}$ in accordance with the numerical results [65]. For the ground state one finds for example $X_{10} = 1.19$. In this way we find a polynomial of fourth order [17]

$$\Delta_{nl}^{z-1} = Z e^2 \kappa \left\{ 1 - \frac{1}{2} \hat{\kappa} < \rho >_{nl} + \frac{1}{6} \hat{\kappa}^2 < \rho^2 >_{nl} - \frac{1}{24} \hat{\kappa}^3 < \rho^3 >_{nl} + \hat{\kappa}^4 f_{nl}^{(z-1)} \right\} , \tag{6.36}$$

where $\hat{\kappa} = \kappa a_0^Z$.

which is consistent with the first terms of the perturbation theory and with the numerical solution as well.

We introduce the expression for the average values of ρ, ρ^2, ρ^3 [64] :

$$< \rho >_{nl} = \frac{1}{2}\left[3n^2 - l(l+1)\right] \tag{6.37}$$

$$< \rho^2 >_{nl} = \frac{1}{2}\left[5n^2 + 1 - 3l(l+1)\right] n^2 \tag{6.38}$$

$$< \rho^3 >_{nl} = \frac{7}{4} n^2 < \rho^2 >_{nl} - \frac{3}{16} n^2 \left[(2l+1)^2 - 9\right] < \rho >_{nl} \tag{6.39}$$

and ρ itself is defined according to

$$\rho = \frac{r}{a_0^z}. \tag{6.40}$$

By using these relations we come to the following expression for f_{nl}

$$f_{nl}^{(z-1)} = \frac{\dfrac{1}{2k^2 X_{nl}} - 1 + \dfrac{X_{nl} < \rho >}{2} - \dfrac{X_{nl}^2 < \rho^2 >}{6} + \dfrac{X_{nl}^3 < \rho^3 >}{24}}{X_{nl}^4}, \tag{6.41}$$

with the expression for $< \rho_{nl} >, < \rho_{nl}^2 >, < \rho_{nl}^3 >$ given by equations (6.37- 6.39). In this way the coefficients $f_{nl}^{(z-1)}$ in the polynomial is expressed in terms of the critical value X_{nl} where the level (nl) merges into the continuum. Therefore the level shift is a function which depends only on $X = \kappa a_0^z$. From equation (6.36) we get [17]

$$\Delta_{nl}^{z-1} = 2X|E_{kl}^{(z-1)}| \left\{1 - a_{nl}^{(z-1)} x + b_{nl}^{(z-1)} x^2 - c_{nl}^{(z-1)} x^3 + f_{nl}^{(z-1)} x^4\right\} \tag{6.42}$$

with coefficients following from (6.36–6.38), equation (6.42) is restricted to the region where

$$X \leq X_{nl} \tag{6.43}$$

From the energy levels calculated above one gets the spectral lines and the corresponding line shift. An interesting result is, that in the line shifts calculated from these formulae the self-energy contribution Δ_e and Δ_n do cancel which leads to line shifts

$$\Delta\nu(nl \rightarrow n'l') = h^{-1}\Delta_{nl}^{z-1} - h^{-1}\Delta_{n'l'}^{(z-1)\prime} \tag{6.44}$$

Further we see that $\Delta\nu$ depends only on the dimensionless quantity X. At the critical values $X = X_{sl}$ the line merges and therefore the shifts become meaningless.

The most serious limitation to this theory is due to the fact that we have neglected Pauli-blocking effects. The essence of this is, that states occupied already by electrons cannot be occupied by other electrons. Among the other effects this leads to the relative ”rigidness" of bound states. If a bound state (atom, ion etc.) is formed in a plasma, it needs some space which is not available to other electrons. We consider a simple estimate for these effects. A particle of radius R which is embedded into a plasma (in the 2nd virial coefficient approximation) has the following shift of the chemical potential

$$\Delta\mu = \frac{1}{3}4\pi k_B T R^3 (n_e + \sum n_z). \tag{6.45}$$

Following the general philosophy that the shifts of energy levels correspond to shifts of the chemical potential, we may conclude that the finite volume required by a bound state *nl* leads to a energy level shift.

For simplicity we restrict the following consideration to plasmas consisting only of bare nuclei z = Z and electrons. With

$$R \approx a_0 n^2 \tag{6.46}$$

we get the estimate for the shift due to the Pauli-blocking effects Kilimann et al. [66]

$$\Delta_{nl}^{(z-1)} \approx \frac{4\pi}{3}(a_0^z n^2)^3 (n_e + n_z) k_B T. \tag{6.47}$$

6.6 Recalculation of the lowering of the ionization energy of dense hydrogen-like carbon plasmas

6.6.1 Shifts of energy levels

Bornath et al. [67] found the Jacobi-Padé approximation for the shift of the energy states of hydrogen atoms as function of temperature and density

$$\Delta_{nl} = \frac{Z\varepsilon^2\kappa(1+a_{nl}\hat{\kappa}) + k_B T\hat{n}_e(1+1/Z)A_{nl}}{1+b_{nl}\hat{\kappa}+2a_{nl}\hat{\kappa}^2 n^2 + k_B T\hat{n}_e(1+1/Z)A_{nl}|E_{nl}|^{-1}} \ , \tag{6.48}$$

where

$$A_{nl} = \int \mathrm{d}\vec{p}G(\vec{p})\psi_{nl}(\vec{p})\psi^*_{nl}(\vec{p}) \tag{6.49}$$

$$G(p) = \frac{p^2/(2m)-E_{nl}}{(2\pi)^{9/2}a_0^3(k_B T)^{5/2}m^{3/2}}\exp\left(\frac{-p^2}{2mk_B T}\right) \tag{6.50}$$

and ψ_{nl} is the energy eigenfunction in momentum space.

$$a_{nl} = \frac{<\rho>_{nl}^2/4 - <\rho^2>_{nl}/6}{n^2 D}, \qquad b_{nl} =<\rho>_{nl}/2+a_{nl}, \qquad D = 1-\frac{<\rho>_{nl}}{2n^2} \tag{6.51}$$

where $<\rho_{nl}>, <\rho^2_{nl}>, <\rho^3_{nl}>$ given by equations (6.37-6.39) are the expectation values of ρ for the orbit corresponding to the energy eigenstates (n,l). ρ is defined by

$$\rho = \frac{r}{a_o} \tag{6.52}$$

$a_0 = 0.529\times 10^{-11} m$

To calculate A_{nl} one has to determine the energy eigenfunctions of the plasma particles in momentum space. This may be done by different methods e.g. applying the Ritz variational principle or solving the Schrödinger equation

$$\psi_{nlm_l}(r,\theta,\phi) = R_{nl}(r)\Theta_{lm_l}(\theta)\Phi_{m_l}(\varphi) \tag{6.53}$$

n is the main quantum number, l- the orbital angular momentum quantum number, and m_l- the quantum number of the projection of the orbital angular momentum,

$$n = 1,2,3,\ldots, \quad l = 0,1,2,\ldots,n-1, \quad m_l = -l,\ldots,l.$$

r, θ and ϕ are the coordinates of the electron in the spherical coordinate system the centre of which coincides with the mass centre of the hydrogen-like particle.
The radial part of the solution of the Schrödinger equation

$$R_{n,l(r)} = \frac{2^{l+1}}{n^2}\sqrt{\frac{(n-l-1)!}{(n+l)!}}\left(\frac{1}{a_0}\right)^3 \exp\left[-\frac{r}{na_0}\right]\left(-\frac{r}{na_0}\right)^l L^{2l+1}_{n-l-1}\left(\frac{2r}{na_0}\right) \tag{6.54}$$

is determined by the associated Laguerre polynomials

$$L^{2l+1}_{n-l-1}\left(\frac{2r}{na_0}\right) = \sum_{k=0}^{n-l-1}\frac{(-1)^k(n+l)!(2r/na_0)^k}{(n-l-1-k)!(2l+1+k)!k!} \tag{6.55}$$

The angular dependent part of the solution contains spherical polynomials [68]

$$\Theta_{l,m_l}(\theta) = \sqrt{\frac{(2l+1)}{2}\frac{(l-m_l)!}{(l+m_l)!}}P_l^{m_l}(\cos\theta), \tag{6.56}$$

$$P_l^{m_l}(\cos\theta) = \frac{(1-\cos^2\theta)^{m_l/2}}{2^l l!}\frac{d^{l+m_l}(\cos^2\theta-1)^l}{d(\cos\theta)^{l+m_l}}, \tag{6.57}$$

and the azimuthal part reads

$$\Phi_{m_l}(\varphi) = \frac{1}{\sqrt{2\pi}} \exp(i m_l \varphi), m_l = 0, \pm 1, \pm 2, ... \tag{6.58}$$

$\psi_{nlm_l}(\vec{p})$ may be related to $\psi_{nlm_l}(\vec{r})$ by

$$\psi_{nlm_l}(\vec{p}) = \frac{1}{h^{3/2}} \int \mathrm{d}r r^2 \int_0^{\pi} \mathrm{d}\theta \sin\theta \int_0^{2\pi} \mathrm{d}\varphi \exp\left[-i\frac{pr}{\hbar}\right] \psi_{nlm_l}(\vec{r}) \tag{6.59}$$

where h is the Planck constant.

$$\psi^*_{nlm_l}(\vec{p}) = \frac{1}{h^{3/2}} \int \mathrm{d}r r^2 \int_0^{\pi} \mathrm{d}\theta \sin\theta \int_0^{2\pi} \mathrm{d}\varphi \exp\left[i\frac{pr}{\hbar}\right] \psi_{nlm_l}(\vec{r}) \tag{6.60}$$

Using equations (6.59, 6.60) in the expression for (6.49) and integrating over the azimuthal angles φ and φ_1, one gets

$$\begin{aligned} A_{nlm_l} &= \frac{8\pi^2}{h^3} \int_0^{\infty} \mathrm{d}p p^2 G(p) \int_0^{\infty} \mathrm{d}r r^2 R_{nl}(r) \int_0^{\pi} \mathrm{d}\theta \sin\theta\, \Theta(\theta) \exp\left\{i\frac{pr\sin\theta}{\hbar}\right\}. \\ & \int_0^{\infty} \mathrm{d}r_1 r_1^2 R_{nl}(r_1) \int_0^{\pi} \mathrm{d}\theta_1 \sin\theta_1 \Theta(\theta) \exp\left\{-i\frac{pr_1\sin\theta_1}{\hbar}\right\} \delta^2_{m_0,0} \end{aligned} \tag{6.61}$$

Further, using

$$e^{ix} = \cos(x) + i\sin(x)$$

one may derive the relation

$$\int_0^{\infty} \mathrm{d}r r^2 R_{nl}(r) \int_0^{\pi} \mathrm{d}\theta \sin\theta\, \Theta(\theta) \exp\left\{i\frac{pr\sin\theta}{\hbar}\right\} = B_1(p) + B_2(p) \tag{6.62}$$

$$\int_0^\infty \mathrm{d}r_1^2 r_1^2 R_{nl}(r_1) \int_0^\pi \mathrm{d}\theta_1 \sin\theta_1 \Theta(\theta_1) \exp\left\{-i\frac{pr_1\sin\theta_1}{\hbar}\right\} = B_1(p) - B_2(p) \tag{6.63}$$

$$B_1(p) = \int_0^\infty \mathrm{d}r r^2 R_{nl}(r) \int_{-1}^1 \mathrm{d}z \Theta(z) \cos\left(\frac{pr}{\hbar}\sqrt{1-z^2}\right) \tag{6.64}$$

$$B_2(p) = \int_0^\infty \mathrm{d}r r^2 R_{nl}(r) \int_{-1}^1 \mathrm{d}z \Theta(z) \sin\left(\frac{pr}{\hbar}\sqrt{1-z^2}\right) \tag{6.65}$$

That means

$$A_{nlm_l} = \frac{8\pi^2}{h^3} \int_0^\infty \mathrm{d}p p^2 G(p) [B_1^2(p) - B_2^2(p)] \tag{6.66}$$

Thus, concerning the integration over the radii $\vec{r}$ and $\vec{r_1}$, one has to solve only two integrals

$$C(p,z) = \int_0^\infty \mathrm{d}r r^2 R_{nl}(r) \cos(gr) \tag{6.67}$$

and

$$D(p,z) = \int_0^\infty \mathrm{d}r r^2 R_{nl}(r) \sin(gr) \tag{6.68}$$

where

$$g = \frac{p}{\hbar}\sqrt{1-z^2} \tag{6.69}$$

$$B_1(p) = \int_{-1}^1 \mathrm{d}z \Theta_{l,0}(z) C(p,z), \qquad B_2(p) = \int_{-1}^1 \mathrm{d}z \Theta_{l,0}(z) D(p,z). \tag{6.70}$$

Substituting the radial part of the wave function (6.54, 6.55) into (6.67) and using the relations [69]

$$\int x^j e^{ax} \sin bx \mathrm{d}x = e^{ax} \sum_{k=1}^{j+1} \frac{(-1)^{k+1} j! x^{j-k+1}}{(j-k+1)!(a^2+b^2)^{k/2}} \sin(bx+kt) \tag{6.71}$$

$$\int x^j e^{ax} \cos bx \mathrm{d}x = e^{ax} \sum_{k=1}^{j+1} \frac{(-1)^{k+1} j! x^{j-k+1}}{(j-k+1)!(a^2+b^2)^{k/2}} \cos(bx+kt) \tag{6.72}$$

$$\sin t = -\frac{b}{\sqrt{a^2+b^2}}, \qquad \cos t = \frac{a}{\sqrt{a^2+b^2}} \tag{6.73}$$

that means

$$\int_0^\infty x^j e^{ax} \mathrm{d}x = \frac{(-1)^{j+1)} j! \cos([j+1]t)}{(a^2+b^2)^{[j+1]/2}} \tag{6.74}$$

$$\int_0^\infty x^j e^{ax} \mathrm{d}x = \frac{(-1)^{j+1)} j! \sin([j+1]t)}{(a^2+b^2)^{[j+1]/2}} \tag{6.75}$$

One has for C(p,z) and D(p,z)

$$C(p,z) = -n a_0^{3/2} 2^{l+1} \sqrt{\frac{(n+l)!(n-l-1)!}{(1+b^2)^{k+l+3}}} \sum_{k=0}^{n-l-1} \frac{2^k (k+l+2)! \cos[(k+l+3)t]}{(n-l-k-1)!(2l+k+1)!k!} \tag{6.76}$$

$$D(p,z) = -na_0^{3/2} 2^{l+1} \sqrt{\frac{(n+l)!(n-l-1)!}{(1+b^2)^{k+l+3}}} \sum_{k=0}^{n-l-1} \frac{2^k (k+l+2)! \sin[(k+l+3)t]}{(n-l-k-1)!(2l+k+1)!k!} \tag{6.77}$$

$$b = na_0 g = na_0 \frac{p}{\hbar} \sqrt{1-z^2} \tag{6.78}$$

Using these expressions, one obtains for $B_1(p)$ and $B_2(p)$ the relations

$$\begin{aligned} \begin{pmatrix} B_1(p) \\ B_2(p) \end{pmatrix} &= na_0^{3/2} 2^{l+0.5} \sqrt{(2l+1)(n+l)!(n-l-1)!} \sum_{k=0}^{n-l-1} \frac{2^k (k+l+2)!}{(n-l-k-1)!(2l+k+1)!k!} \\ &\cdot \int_{-1}^{1} \mathrm{d}z \frac{P_l^0(z)}{[1+n^2 a_0^2 p^2 (1-z^2)/\hbar^2]^{(k+l+3)/2}} \begin{pmatrix} \cos[(k+l+3)t(z)] \\ \sin[(k+l+3)t(z)] \end{pmatrix}. \end{aligned} \tag{6.79}$$

Clearly, $B_1(p)$ and $B_2(p)$ depend on the orbital angular momentum quantum number . The numerical solution of the equation is to be done through FORTRAN programming and the results have been used to evaluate A_{nl} and hence the energy shifts as given by equation (6.48).

6.6.2 Analytical relations developed for computer program testing

The numerical computations for B_1 and B_2 as described in the previous section have been done through computer programming. In order to verify these results analytical relations have been developed for different values of main quantum numbers and orbital angular momentum quantum numbers. The output values from these results agree quite well with those obtained from computer program.

Taking into account [70]

$$I = \int_{-1}^{1} \frac{(1-x^2)^{\mu-1}}{(1-a^2x^2)^{\nu}} \mathrm{d}x = \frac{\sqrt{\pi}\Gamma(\mu)}{\Gamma(\mu+\frac{1}{2})} {}_2F_1(\nu, \frac{1}{2}; \mu+\frac{1}{2}; a^2), \quad \text{for } \mathrm{Re}\mu > 0, a^2 < 1, \tag{6.80}$$

(expression 7.136, p.611 in (Gradshteyn and Ryzhik 1994) contains a misprint) and

$${}_2F_1(\nu, l; \nu; a^2) = \frac{1}{(1-a^2)^l}, \tag{6.81}$$

one finds for the main quantum numbers $n = 1, 2, 3$ and at $l = 0, 1, \ldots n-1$

For $n = 1$, $l = 0$

$$B_1(p) = -2\sqrt{2}\left(a_0^Z\right)^{3/2}\left[\frac{1}{a_n} - \frac{3}{a_n^2} + \frac{3}{2a_n}\left(1 - \frac{1}{a_n}\right)\frac{1}{\sqrt{-a_n c_n}}\ln\frac{\sqrt{-a_n c_n} - c_n}{c_n + \sqrt{-a_n c_n}}\right]. \tag{6.82}$$

$n = 2$, $l = 0$

$$B_1(p) = -8\left(a_0^Z\right)^{3/2}\left[-\frac{11}{a_n^2} + \frac{15}{a_n^3} + \left(\frac{3}{a_n} - \frac{21}{2a_n^2} + \frac{15}{2a_n^3}\right)\frac{1}{\sqrt{-a_n c_n}}\ln\frac{\sqrt{-a_n c_n} - c_n}{c_n + \sqrt{-a_n c_n}}\right]. \tag{6.83}$$

$n = 3$, $l = 0$

$$\begin{aligned} B_1(p) &= -6\sqrt{6}\left(a_0^Z\right)^{3/2}\left[\frac{1}{3a_n} - \frac{59}{3a_n^2} + \frac{250}{3a_n^3} - \frac{70}{a_n^4} + \left(\frac{9}{2a_n} - \frac{69}{2a_n^2} + \frac{65}{a_n^3} - \frac{35}{a_n^4}\right)\right. \\ &\qquad \left.\frac{1}{\sqrt{-a_n c_n}}\ln\frac{\sqrt{-a_n c_n} - c_n}{c_n + \sqrt{-a_n c_n}}\right]. \end{aligned} \tag{6.84}$$

$n = 3$, $l = 2$

$$\begin{aligned} B_1(p) = -24\sqrt{3}\left(a_0^Z\right)^{3/2}&\left[-\frac{1}{6a_n} - \frac{3}{4a_n c_n} + \frac{1}{12a_n^2} + \frac{5}{a_{n^2} c_n} - \frac{20}{3a_n^3} - \frac{15}{4a_n^3 c_n} + \frac{35}{4a_n^4} - \frac{1}{2c_n}\right. \\ &\left. + \left(\frac{35}{8a_n^4} - \frac{15}{8a_n^3 c_n} + \frac{15}{4a_n^2 c_n} - \frac{25}{4a_n^3} - \frac{15}{8a_n c_n} + \frac{15}{8a_n^2}\right) - \frac{1}{\sqrt{-a_n c_n}}\ln\frac{\sqrt{-a_n c_n} - c_n}{c_n + \sqrt{-a_n c_n}}\right] \end{aligned} \tag{6.85}$$

$n = 1$, $l = 0$

$$\begin{aligned} B_2(p) &= -\left(a_0^Z\right)^{3/2}\frac{\sqrt{-2c_n\pi}}{a_n^2}\left[\left(1 + \frac{c_n}{a_n}\right)^{-1/2} - \frac{4}{a_n}\,{}_2F_1\left(3, \frac{1}{2}; 2; -\frac{c_n}{a_n}\right)\right] \\ &= 3\pi\sqrt{-\frac{2c_n}{a_n}\frac{(a_0^Z)^{3/2}}{a_n^2}}, \end{aligned} \tag{6.86}$$

$n=2\,,\ l=0$

$$B_2(p) \;=\; -a_0^{Z\,3/2}\frac{4\pi\sqrt{-c_n}}{a_n^2}\left[\sqrt{a_n}-\frac{16}{a_n}\,{}_2F_1\left(3,\frac{1}{2};2;-\frac{c_n}{a_n}\right)+\frac{24}{a_n^2}\,{}_2F_1\left(4,\frac{1}{2};2;-\frac{c_n}{a_n}\right)\right], \tag{6.88}$$

$n=3\,,\ l=0$

$$\begin{aligned} B_2(p) \;=\; & -3\frac{a_0^Z\pi}{a_{n^2}}\sqrt{-6c_n a_0^Z}\left[\sqrt{a_n}-\frac{36}{a_n}\,{}_2F_1\left(3,\frac{1}{2};2;-\frac{c_n}{a_n}\right)+\frac{144}{a_n^2}\,{}_2F_1\left(4,\frac{1}{2};2;-\frac{c_n}{a_n}\right)\right. \\ & \left.-\frac{128}{a_n^3}\,{}_2F_1\left(5,\frac{1}{2};2;-\frac{c_n}{a_n}\right)\right], \end{aligned} \tag{6.89}$$

$n=1\,,\ l=0$

$$\begin{aligned} B_2(p) \;=\; & -12\frac{a_0^Z\pi}{a_{n^2}}\sqrt{-3c_n a_0^Z}\left[\frac{16}{a_n^3}\left(1+\frac{3a_n}{c_n}\,{}_2F_1\left(5,\frac{1}{2};2;-\frac{c_n}{a_n}\right)\right)-\left(\frac{12}{a_n^2}+\frac{48}{a_n^2c_n}+\frac{36}{a_nc_n}\right)\right. \\ & \left.{}_2F_1\left(4,\frac{1}{2};2;-\frac{c_n}{a_n}\right)+\left(\frac{3}{c_n}+\frac{1}{a_n}+\frac{36}{a_nc_n}\right){}_2F_1\left(3,\frac{1}{2};2;-\frac{c_n}{a_n}\right)-\frac{3\sqrt{a_n}}{c_n}\right], \end{aligned} \tag{6.90}$$

$n=1\,,\ l=1$

$$B_1(p)=B_2(p)=0 \tag{6.91}$$

where

$${}_2F_1(\alpha,\beta,\gamma;z) \;=\; 1+\frac{\alpha\beta}{\gamma}z+\frac{\alpha(\alpha+1)\beta(\beta+1)}{\gamma(\gamma+1)}\frac{z}{2!}+\frac{\alpha(\alpha+1)(\alpha+2)\beta(\beta+1)(\beta+2)}{\gamma(\gamma+1)(\gamma+2)}\frac{z^3}{3!}+\ldots \tag{6.92}$$

is the hypergeometric function and

$$c_n=n^2(a_0^Z)^2p^2/\hbar^2<0,\; a_n=1-c_n\,. \tag{6.93}$$

6.7 Results of the numerical calculations

Calculations of the relative line shifts are performed for five-fold ionized carbon ions with densities of the order of $10^{27} - 10^{29} m^{-3}$ at temperatures of $10^6 - 10^8$ K using the relations (6.48, 6.50, 6.61, 6.82–6.93). There the term proportional to $\hat{\kappa}^2$ in the denominator of equation (6.48) is neglected. The chosen plasma parameters occur in the inner parts of a star like the Sun, but they should also be (soon) reachable in laboratory experiments with high energy density beams and X-ray lasers.

Figure 6.2 shows the Mott parameter of the studied carbon plasma as function of the temperature. The Mott parameter is proportional to the square root of the plasma density and the inverse temperature.

The function $A_{nl}(T)$ (multiplied by h^3) is presented in figures (6.3-6.6) for the main quantum numbers $n = 1, 2, 3$ and the orbital angular momentum quantum numbers $l = 0, 2$ in case of the bound states of five-fold-ionized carbon as function of the temperature. In the present approximation A_{nl} does not depend on the plasma density, and in the case of $l = 1$, A_{nl} equals zero. In case of $B_1^2(p) - B_2^2(p) > 0$, the integrand of the p-integration of A_{nl} increases with increasing temperature at constant p. It has a maximum at $T = p^2/(5m_e k_B)$, and then it decreases again. This easily follows from equation (6.66). Thus at growing $p = const$ also the maximum of the integrand occurs at a large temperature. Consequently, within the frame of the present approximation, $A_{nl}(T)$ may have not only one extremum at a certain value of T, but there may exist both maxima and minima.

The relative energy shifts of the bound states of the five-fold-ionized carbon ions are shown in figure 6.7. There all shifts are normalized to the ground state energy of the carbon ions. All shifts for the whole analyzed temperature-density region are presented in the chosen interval of Mott parameters. This interval is only a small part of the studied Mott parameters to be seen in figure 6.2. It is tried to present results where the splitting of the curves for different l is to be seen at constant n. Besides, it is concentrated on results for the shifts of lines before the merging with the continuum of the ground state starts. As the terms proportional to A_{nl} in the nominator and the denominator of equation (6.48) are smaller than the other terms, respectively, the shifts may be presented - on a first sight- as a function of Mott parameter $\hat{\kappa}$ only. It is to be seen that within the studied temperature region the relative energy level shifts for the given n and l increase with increasing $\hat{\kappa}$. At constant main quantum number n and constant Mott parameter $\hat{\kappa}$, the energy shift decreases with growing angular momentum quantum number l, and at constant l and $\hat{\kappa}$, the shift gets smaller with increasing n. Curves presenting shifts at constant n and l may cross with increasing $\hat{\kappa}$. So, at $\hat{\kappa} < 0.45$, the shifts for $n = 2$, $l = 1$ are larger than those for $n = 3$, $l = 0$. But under the condition $\hat{\kappa} > 0.45$, the contrary behaviour is found.

6.8 Conclusions

In connection with the strong interest in the thermodynamics of dense carbon plasmas in astro physics and laboratory experiments, a careful recalculation of the partition function of hydrogen-like warm dense matter is necessary. Here, an attempt is made to contribute to a review concerning the density and temperature dependence of the energy level shifts in dense matter. At the same time, some small misprints in former papers of other authors are corrected, at least noted.

The work especially considers the relative energy shift of the spectral lines based on the Jacobi-Padé approximations developed by Ebeling, Killimann and Kraeft. In these approximations the shifts depend on the almost unknown eigenfunctions of the systems in momentum space. Here a, to a large extent analytical, method is developed to calculate these line shifts starting with the energy eigenfunctions in spatial space. This approach makes it possible to distinguish between line shifts for different orbital angular momentum quantum numbers in case of the same main quantum number. The developed method will be practicable also in case of future improved Padé approximations of line shifts.

In the work, nine-fold integrals describing line shifts are analytically reduced to a two-fold integral. In the case of the main quantum numbers $n = 1, 2$ and 3, even reductions to one dimensional momentum integrals are found. These results are very useful to check currently being developed numerical codes to calculate line shifts. They are applied to construct a new model for the partition function of warm dense matter.

For the case of the plasma of five-fold ionized carbon ions, the relative level shifts are calculated for a rather large density-temperature region. Although the general Padé approximation for the relative line shifts has to be further developed to improve the description of the plasma thermodynamics approaching the region of the Mott transitions, the overall behaviour of the relative line shifts as function of the Mott parameter is obtained. The relative line shifts increase with increasing Mott parameter, but approaching the merging of the spectral lines with the continuum, the growth of the shifts gets weaker. Dependencies of the line shifts on main quantum numbers and orbital quantum numbers are discussed. These results were presented at the Heavy Ion Fusion (HIF 2010) conference at Darmstadt and are accepted for publishing in Laser and Particle Beams.

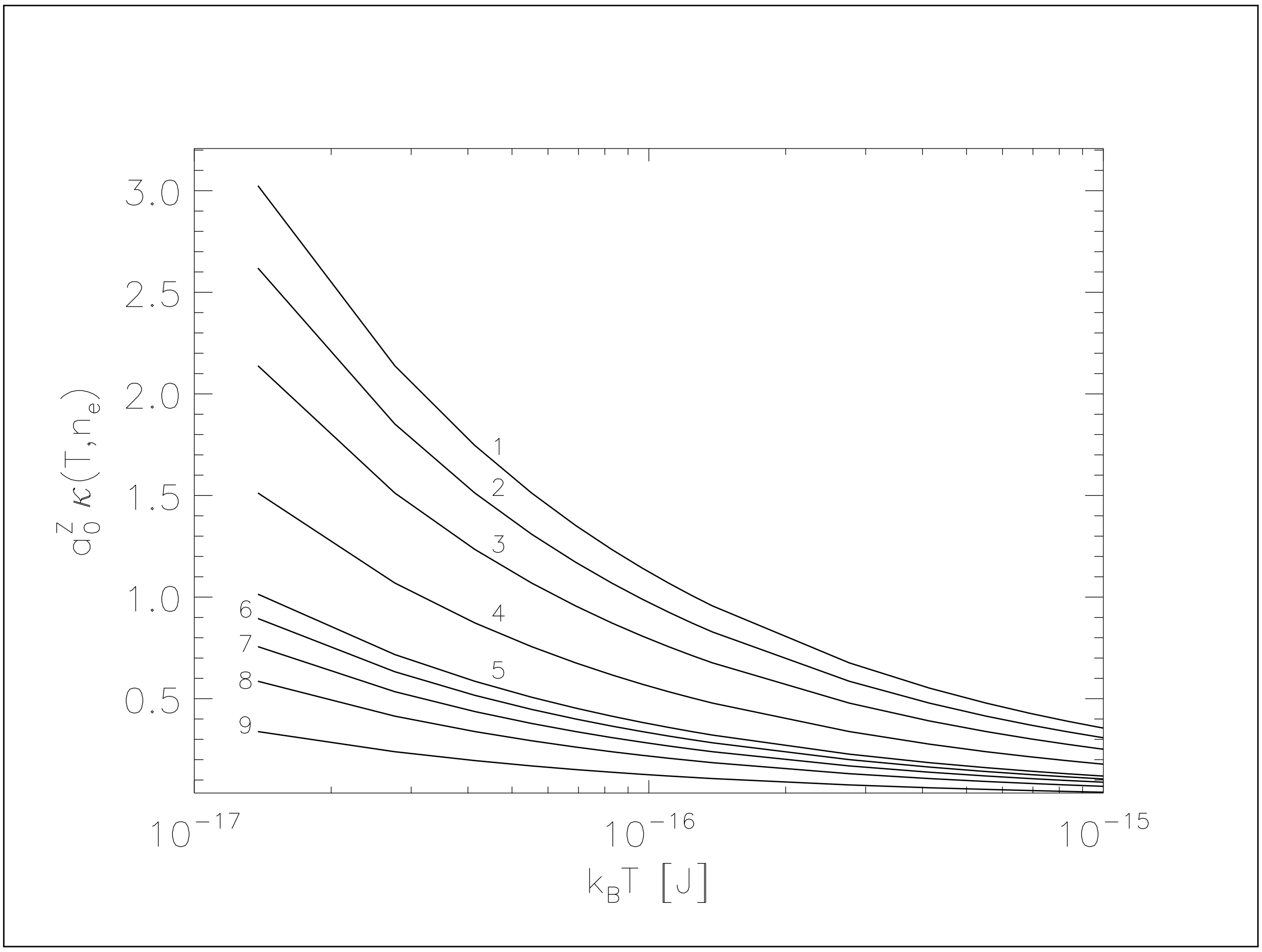

Figure 6.2: Mott parameter of a plasma of five-fold-ionized carbon ions as function of temperature times Boltzmann constant. $10^{-17}\mathrm{J} = 62.5\mathrm{eV}$. 1) $n_e = 8.10^{31}\mathrm{m}^{-3}$, 2) $n_e = 6.10^{31}\mathrm{m}^{-3}$, 3) $n_e = 4.10^{31}\mathrm{m}^{-3}$, 4) $n_e = 2.10^{31}\mathrm{m}^{-3}$, 5) $n_e = 9.10^{30}\mathrm{m}^{-3}$, 6) $n_e = 7.10^{30}\mathrm{m}^{-3}$, 7) $n_e = 5.10^{30}\mathrm{m}^{-3}$, 8) $n_e = 3.10^{30}\mathrm{m}^{-3}$, 9) $n_e = 10^{30}\mathrm{m}^{-3}$.

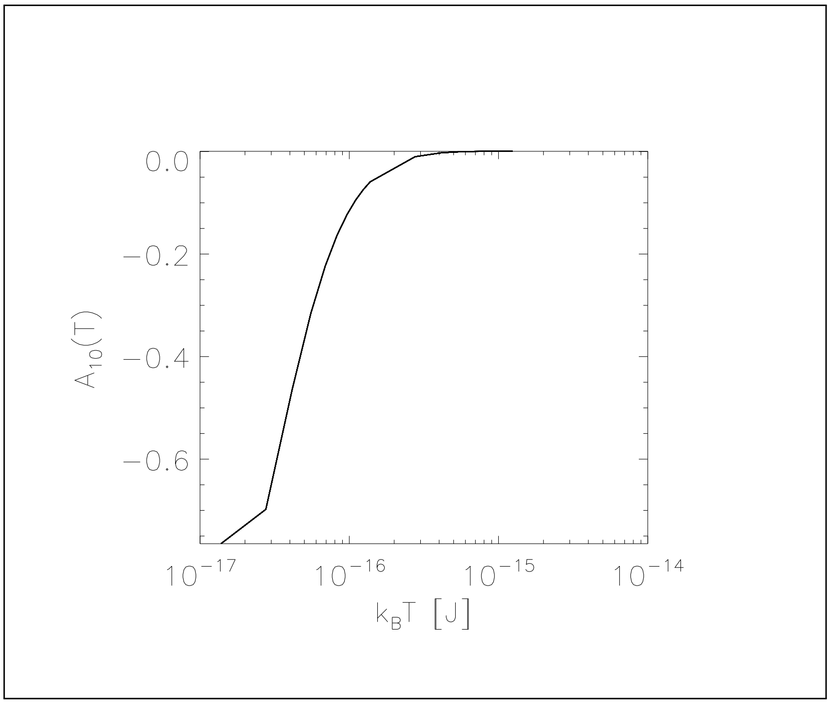

Figure 6.3: A_{10} as a function of temperature *T*.

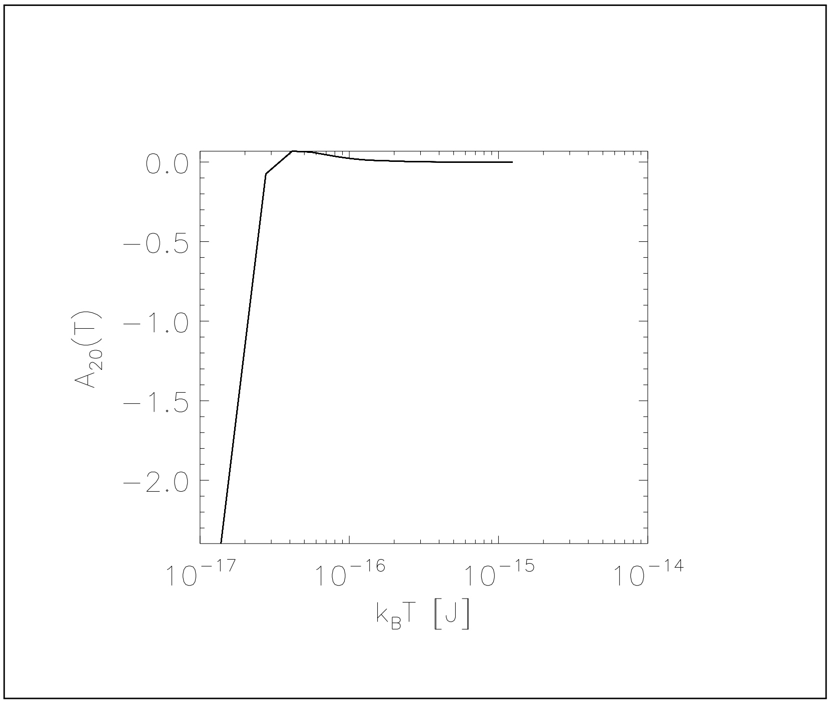

Figure 6.4: A_{20} as a function of temperature *T*.

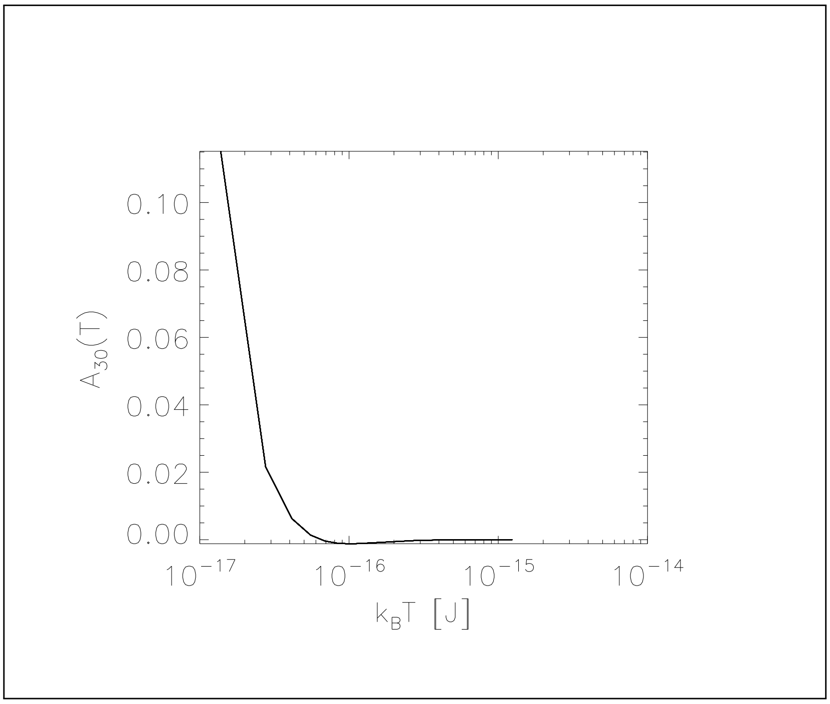

Figure 6.5: A_{30} as a function of temperature *T*.

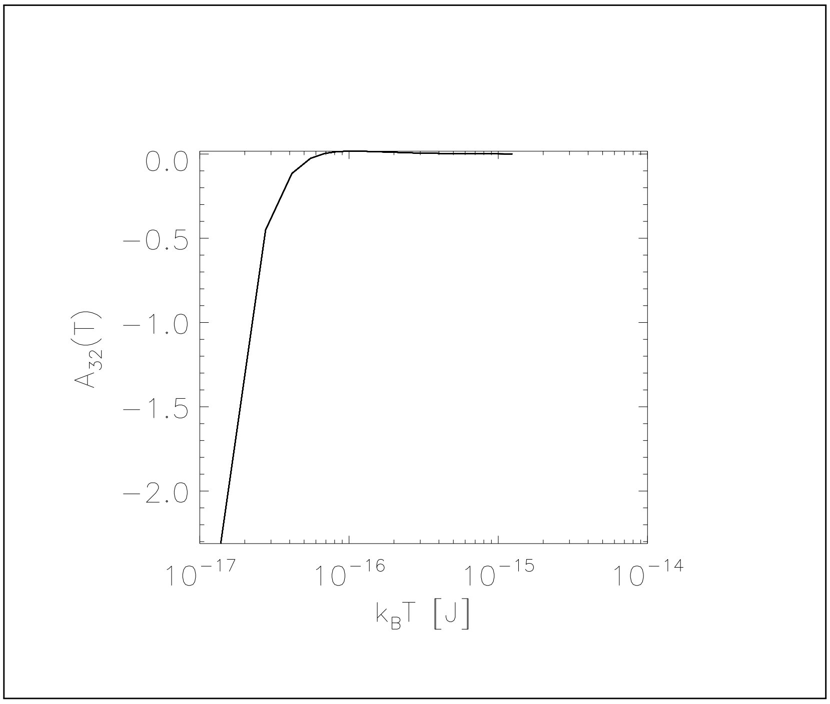

Figure 6.6: A_{32} as a function of temperature *T*.

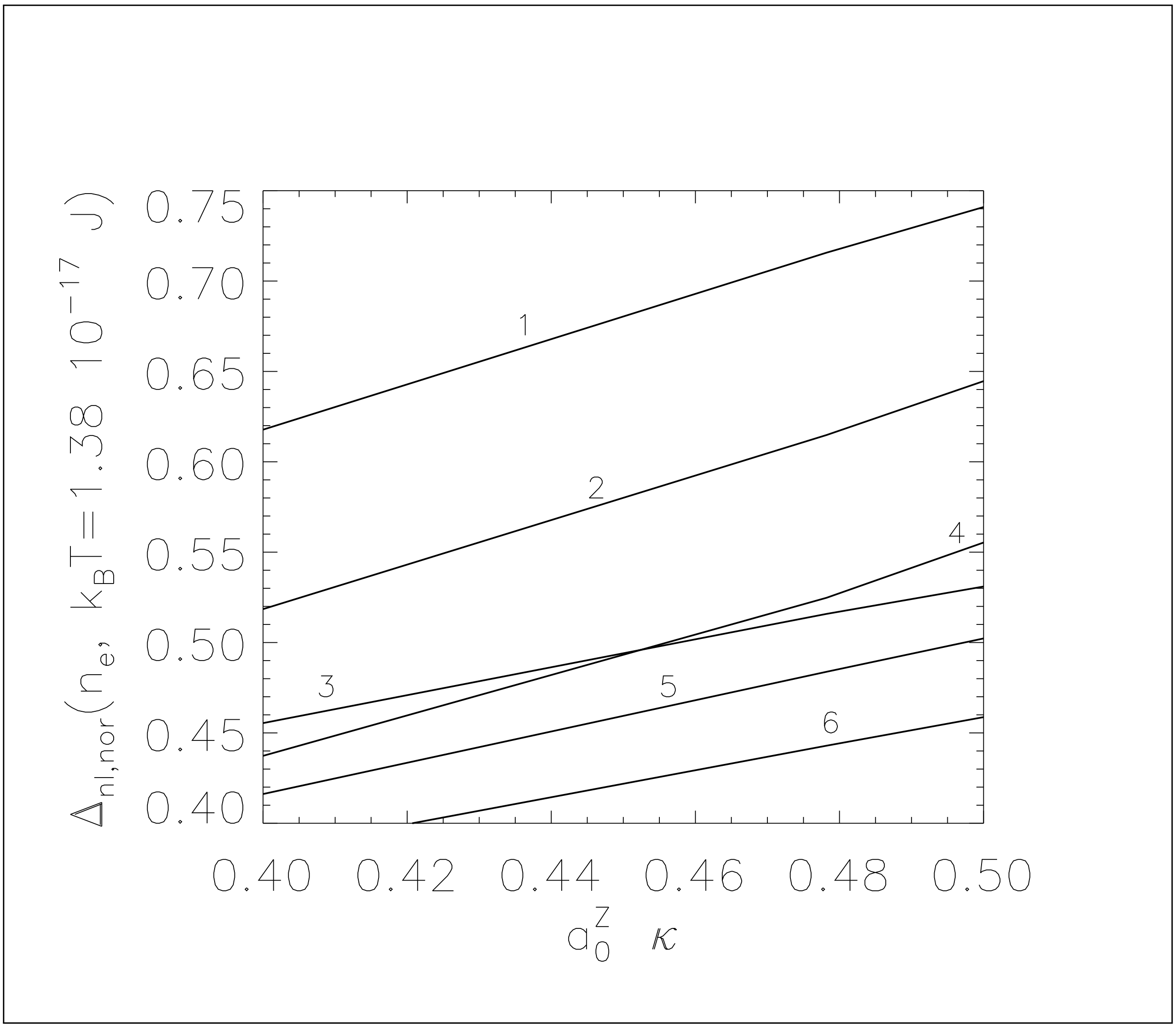

Figure 6.7: Relative energy shifts $\Delta_{n,l,nor}$ of hydrogen like carbon bound states as function of the Mott parameter $\hat{\kappa}$. The energy shifts are normalized to the energy of the ground state of the carbon ion. $1)\,n=1,l=0,\ 2)\,n=2,l=0,\ 3)\,n=2,l=1,\ 4)\,n=3,l=0,\ 5)\,n=3,l=1,\ 6)\,n=3,l=2$. *n*-main quantum number, *l*-orbital angular momentum quantum number. Curve 5 is separately to be seen between the curve 4 and 6 at $\hat{\kappa}=a_0^Z\kappa>0.08$.

Outlook

Part of the present work has been contributed to develop cryogenic system in which solid-state targets of rare gases, nitrogen, deuterium and hydrogen of different geometries and sizes can be produced. After few modifications the system has been installed at the Z6 experimental area of GSI where first beam plasma interaction experiments have been conducted. The targets are sufficiently sustainable within the experimental conditions at the Z6 and can be reproduced at a repetition rate of a few minutes to half an hour depending on the target substance. In order to produce a high density fully ionised laser generated plasma thin deuterium targets are well suited. In the present work thin solid deuterium targets with a diameter of 2 mm have been simultaneously irradiated by the *nhelix* and PHELIX high energy laser systems and free electron density measurements have been done within the framework of the present dissertation.

There are a few technical issues that need to be addressed to perform energy loss experiments using cryogenic targets. One of the key developments required is the in-situ arrangement for the characterization of the target thickness. The targets are produced in vacuum and their thickness is reduced due to sublimation. However, the idea to sublimate the target did not work as the target vanishes before performing useful experiments. Therefore, an external source like infra-red heating or beam sputtering may be devised to effectively control the target thickness.

The second part of the dissertation is focused on the study of hydrogen-like bound-states addressing phenomena like self-energy, dynamical screening of the coulomb interactions and the quantum-physical effects like Pauli-blocking. Here, the Jacobi-Padé approximation has been applied to a carbon plasma consisting of six-fold and five-fold carbon atoms and electrons. An almost analytical analysis has been performed to estimate the kinetic energy contribution to the relative energy level shifts as well as the influence of angular momentum quantum number l on these shifts. Further, relative energy shifts of the bound states of five-fold ionized carbon are numerically obtained as function of the Mott parameter of the plasma. The relative shifts increase with increasing Mott parameter, but approaching the merging of the energy levels with the continuum, the growth of shifts becomes weaker. The present Padé approximation may be further developed taking into account new results on Pauli blocking and increasing the accuracy of the general Padé expression.

Bibliography

[1] N. K. Glendenning: *After the Beginning*, Imperial College Press, 2004.

[2] K. Zioutas, D. H. H. Hoffmann, K. Dennerl and T. Papaevangelou: *What is dark matter made of ?*, Science, **306**(5701):1485–1488, 2004.

[3] D. H. H. Hoffmann, V. E. Fortov, M. Kuster, V. Mintsev, B. Y. Sharkov, N. A. Tahir, S. Udrea, D. Varentsov and K. Weyrich: *High energy density physics generated by intense heavy ion beams*, Astrophysics and Space Science, **322**(1-4):167–177, 2009.

[4] B. A. Remington, D. Arnet, R. P. Drake and H. Takabe: *Modeling astrophysical phenomena in the laboratory with intense lasers*, Science, **284**(5419):1488–1493, 1999.

[5] J. Nuckolls, L. Wood, A. Thiessen and G. Zimmerman: *Laser compression of matter to super-high densities: Thermonuclear (CTR) applications*, Nature, **239**:139–142, 1972.

[6] N. A. Tahir, A. R. Piriz, G. Wouchuk, A. Shutov, I. V. Lomonosov, V. E. Fortov, C. Deutsch and D. H. H. Hoffmann: *Laboratory planetary science studies using intense heavy ion beams at FAIR: The HEDgeHOB collaboration*, Nuclear Instruments and Methods in Physics Research A, **606**(1-2):177–185, 2009.

[7] P. K. Patel, A. J. Mackinnon, M. H. Key, T. E. Cowan, M. E. Foord, M. Allen, D. F. Price, H. Ruhl, P. Springer and R. Stephens: *Isochoric heating of solid-density matter with an ultrafast proton beam*, Physical Review Letters, **91**(12):125004–8, 2003.

[8] J. J. MacFarlane, J. E. Bailey, G. A. Chandler, C. Deeney, M. R. Douglas, D. Jobe, P. Lake, T. J. Nash, D. S. Nielsen, R. B. Spielman, P. Wang and P. Woodruff: *X-ray absorption spectroscopy measurements of thin foil heating by Z-pinch radiation*, Physical Review E, **66**(4):046416–26, 2002.

[9] K. Weyrich, H. Wahl, A. Golubev, A. Kantsyrev, M. Kulish, S. Dudin, D. Hoffmann, B. Sharkov and V. Mintsev: *Influence of the gap-target configuration on the measured energy loss of C-ions in Ar-gas and -plasma*, Nuclear Instruments and Methods in Physics Research Section A: Accelerators, Spectrometers, Detectors and Associated Equipment, **577**(1-2):366 – 370, 2007.

[10] N. Bohr: *Velocity-range relation for fission fragments*, Physical Review, **59**(3):270–275, 1941.

[11] H. Bethe: *Zur Theorie des Durchgangs schneller Korpuskularstrahlen durch Materie.*, Annalen der Physik, **397**(3):325–400, 1930.

[12] F. Bloch: *Zur Bremsung rasch bewegter Teilchen beim Durchgang durch Materie*, Annalen der Physik, **408**(3):285–320, 1933.

[13] D. H. H. Hoffmann, N. A. Tahir, S. Udrea, O. Rosmej, C. V. Meister, D. Varentsov, M. Roth, G. Schaumann, A. Frank, A. Blazevic, J. Ling, A. Hug, J. Menzel, T. Hessling, K. Harres, M. Günther, S. El-Moussati, D. Schumacher and M. Imran: *High energy density physics with heavy ion beams and related interaction phenomena*, Contribution to Plasma Physics, **50**(1):7–15, 2010.

[14] A. Frank, A. Blazevic, P. L. Grande, K. Harres, T. Hessling, D. H. H. Hoffmann, R. Knobloch-Maas, P. G. Kuznetsov, F. Nürnberg, A. Pelka, G. Schaumann, G. Schiwietz, A. Schökel, M. Schollmeier, D. Schumacher, J. Schütrumpf, V. V. Vatulin, O. A. Vinokurov and M. Roth: *Energy loss of argon in a laser-generated carbon plasma*, Physical Review E, **81**(2):026401–6, 2010.

[15] W. Ebeling, W.-D. Kraeft and D. Kremp: *Theory of Bound States and Ionization Equilibrium in Plasmas and Solids*, Akademie-Verlag, Berlin, 1976.

[16] W. Ebeling, C.-V. Meister, R. Sändig and W.-D. Kraeft: *Pressure Ionization in nonideal alkali plasmas*, Annalen der Physik, **36**(5):321–332, 1979.

[17] W. Ebeling, J. Leike and U. Leonhardt: *Bound states and ionization kinetics in dense plasmas*, 1991.

[18] D. V. Fisher, Z. Henis, S. Eliezer and J. Meyer-Ter-Vehn: *Core holes, charge disorder, and transition from metallic properties in ultrashort pulse irradiation of metals*, Laser and Particle Beams, **24**(1):81–91, 2006.

[19] W.-D. Kraeft, D. Kremp, W. Ebeling and G. Röpke: *Quantum Statistics of Charged Particle System*, Plenum Press, 1986.

[20] W.-D. Kraeft, D. Kremp, K. Kilimann and H. E. D. Witt: *Two-body problem in many particle system.*, Physical Review A, **42**(4):2340–2345, 1990.

[21] D. Kremp, M. Schlanges and W.-D. Kraeft: *Quantum Statistics of Non-Ideal Plasmas*, Springer, 2005.

[22] C.-V. Meister: *On the theory of conductivity and thermodynamics of nonideal plasmas*, Ph.D. thesis, University Rostock, 1982.

[23] A. Rubenchik and S. Witkowski: *Physics of Laser Plasma*, North-Holland, 1991.

[24] P. Mulser, R. Siegel and S. Witkowski: *Plasma Production by Laser*, Physics Report C, **6**(3):187–239, 1973.

[25] V. P. Ageev, A. A. Gorbunov, V. P. Danilov, V. I. Konov, P. I. Nikitin and A. M. Prokhor: *Plasma-formation threshold conditions for the interaction of pulsed ultraviolet radiation with solid targets*, Soviet Journal of Quantum Electronics, **13**(12):1595, 1983.

[26] D. I. Rosen and G. Weyl: *Laser-induced breakdown in nitrogen and the rare gases at 0.53 and 0.357* μm, Journal of Physics D: Applied Physics, **20**(10), 1987.

[27] P. Mulser and D. Bauer: *High Power Laser-Matter Interaction*, Springer, 2010.

[28] S. Atzeni and J. Meyer-Ter-Vehn: *The Physics of Inertial Fusion*, Claredon Press-Oxford, 2004.

[29] T. Hessling: *Charakterisierung lasererzeugter Hohlraumstrahlung für die experimentelle Untersuchung der Wechselwirkung von Schwerionen mit Plasmen*, Ph.D. thesis, Technische Universität Darmstadt, 2010.

[30] N. A. Krall and A. W. Trivelpiece: *Principles of Plasma Physics*, San Francisco Press Inc, 1986.

[31] D. W. Forslund, J. M. Kindel, K. Lee, E. L. Lindmann and R. L. Morse: *Theory and simulation of resonant absorption in a hot plasma*, Physical Review A, **11**:679–683, 1975.

[32] D. H. H. Hoffmann, K. Weyrich, H. Wahl, T. Peter, J. M. ter Vehn, J. Jacoby, R. Bimbot, D. Gardes, M. Dumail, C. Fleurier, A. Sanba, C. Deutsch, G. Maynard, R. Noll, R. Haas, R. Arnold and S. Maurmann: *Experimental observation of enhanced stopping of heavy ions in a hydrogen plasma*, Zeitschrift für Physik A - Atomic Nuclei, **30**(3):339–340, 1988.

[33] K.-G. Dietrich, D. H. H. Hoffmann, H. Wahl, R. Haa, W. Brandenburg and R. Noll: *Eenergy loss of heavy ions in a dense hydrogen plasma*, Zeitschrift Physik D - Atoms, Molecules and Clusters, **16**(4):229–230, 1990.

[34] M. Roth, C. Stöckle, W. Süss, O. Iwase, D. O. Gericke, R. Bock, D. H. H. Hoffmann, M. Geissel and W. Seelig: *Energy loss of heavy ions in laser-produced plasmas*, Europhysics Letters, **50**(1):28–34, 2000.

[35] T. Peter: *Energieverlust von Schwerionenstrahlen in dichten Plasmen*, Ph.D. thesis, MPQ, 1988.

[36] L. C. Northcliffe: *Passage of heavy ions through matter*, Annual Review of nuclear and particle science, **13**, 1963.

[37] A. Frank: *Energieverlust von Schweionenstrahlen in lasererzeugten Plasmen*, Master's thesis, Technische Universität Darmstadt, 2008.

[38] A. Pelka: *Bestimmung der Elektrondichte in lasererzeugten Plasmen mittels Laserinterferometrie*, Master's thesis, Technische Universität Darmstadt, 2005.

[39] I. H. Hutchinson: *Principles of Plasma Diagnostics*, second edition, Cambridge University Press, 2002.

[40] P. C. Souers: *Hydrogen Properties for fusion Energy*, University of California Press, 1986.

[41] M. L. Klein and J. A. Venables: *Rare gas solids*, volume I+II, Academic Press, 1977.

[42] `http://encyclopedia.airliquide.com/encyclopedia.asp`.

[43] J. Menzel: *Aufbau und Inbetriebnahme einer Kryoanlage zur Targeterzeugung für Experimente mit Hochenergielasern und Schwerionenstrahlen*, Ph.D. thesis, Technische Universität Darmstadt, 2010.

[44] K. A. Jackson, D. R. Uhlmann and J. D. Hunt: *On the nature of crystal growth from the melt*, Journal of Crystal Growth, **1**(1):1–36, 1967.

[45] M. H. Kramer: *Epitaxial growth of rare gas solids*, Journal of Crystal Growth, **33**(1):65–76, 1976.

[46] `http://www-inj.gsi.de/index.php?section=3`.

[47] D. Schumacher: *Chraketerisierung laserinduzierter Hohlraumstrahlung*, Master's thesis, Technische Universität Darmstadt, 2007.

[48] `http://www.gsi.de/forschung/phelix/Anlagen/index.htm`.

[49] `http://www.datasheetcatalog.org/datasheet/hamamatsu/C2830.pdf`.

[50] Uwe Denzer, Hamamatsu Photonics Deutschland GmbH: *Personal Communication.* 2010 – Figure.

[51] A. Frank: *Personal Communication.* 2010 – Figure.

[52] J. F. Ziegler: *SRIM: The Stopping and Range of Ions in Matter*, `http://www.srim.org`, 2003/2008.

[53] R. Knobloch-Maas: *Measurement of the energy loss of heavy ions in laser-produced plasmas*, Ph.D. thesis, Technische Universität Darmstadt, 2009.

[54] T. Heßling: *Personal Communication.* 2010 – Figure.

[55] Operation manual: SRDK-415 Cryocooler, Sumitomo heavy industries Ltd. Japan.

[56] Temperature measurement and control catalog: Lake Shore Cryotronics, Inc.

[57] E. R. Koresheva, I. E. Osipov and I. V. Aleksandrova: *Free standing target technologies for inertial fusion energy: Target fabrication, characterization and delivery*, Laser and Particle Beams, **23**:563–571, 2005.

[58] W. G. Lawrence and V. A. Apkarian: *Infrared studies in free standing crystals:* N_2O – doped Xe and Ar, The Journal of Chemical Physics, **97**(4):2224–2228, 1992.

[59] E. Gregoryanz, M. J. Clouter and H. Kiefte: *A method for the growth and cooling of strain-free single crystals of cryogenic solids.*, Review of Scientific Instrument, **70**(8):3495–3496, 1999.

[60] J. Menzel et. al. GSI scientific report 2009.

[61] W. Ebeling, A. Förster, H. Hess and M. U. Romanovsky: *Thermodynamic and kinetic properties of hot nonideal plasmas*, Plasma Physics and Controlled Fusion, **38**(12A):A31–A47, 1996.

[62] `http://astropp.physik.tu-darmstadt.de/media/plasma/plasma-parameter.jpg`.

[63] K. Kilimann, W.-D. Kraeft and D. Kremp: *Lifetime and level shift of bound states in plasmas*, Physics Letters A, (6):393–395, 1977.

[64] W. Ebeling and K. Kilimann: *Ionization energy and level shifts of multiply charged ions in nonideal plasmas.*, Zeitschrift für Naturforschung, **44a**:519–523, 1989.

[65] F. J. Rogers, H. G. Graboske and D. J. Harwood: *Bound eigenstates of the static screened coulomb potential*, Physical Review A, **1**(6):1577–1586, 1970.

[66] W. Ebeling and K. Kilimann: *Energy gap and line shifts for H-like ions in dense plasmas.*, Zeitschrift für Naturforschung, **45a**, 1990.

[67] T. Bornath, W. Ebeling, W.-D. Kraeft, D. Kremp and K. Kilimann: *Preprint Humboldt-Universität zu Berlin*, 1990.

[68] M. Abramowitz and I. A. Stegun: *Handbook of Mathematical Functions with Formulas, Graphs and Mathematical Tables*, Dover Publications, 1970.

[69] I. S. Gradshteyn and I. M. Ryzhik: *Table of integrals, Series and Products*, Academic Press, 1994.

[70] C.-V. Meister, M. Imran and D. H. H. Hoffmann: *Relative energy level shifts of hydrogen-like carbon bound-states in dense matter*, Laser and Particle Beams, accepted for publication, 2010.

Acknowledgements

I would like to thank all those people who helped and encouraged me to accomplish this work.

I am deeply indebted and wish my utmost gratitude to Professor Dr. Dr. h.c./RUS Dieter H.H. Hoffmann for his encouragement, support and valuable suggestions to complete this work. Besides academic support, his kind and friendly attitude has always been a source of inspiration and vigour for me throughout the studies.

I am also thankful to Prof. Dr. Norbert Pietralla for co-refereeing this thesis.

I would like to thank Dr. Serban Udrea. As a co-supervisor he guided and helped me in a variety of ways to accomplish the experimental work. I have benefited a lot from his supervision. I express my sincere gratitude to Dr. Habil. Claudia-Veronika Meister for her guidance and devotion of time which has been the basic instrument in realizing the aims and objectives of the theoretical part of the dissertation. She was always available to discuss obstacles and progress of the work and helped to complete the writing of the thesis. Gratitude is also offered to Dr. Jurij Menzel for his generous help and coordination to develop the cryogenic system and to perform experiments at the Z6. The experimental part of the thesis is greatly indebted to his efforts.

I am also thankful to Professor Dr. Thomas Stöhlker, Professor Dr. Markus Roth and Dr. Abel Blažević for providing the opportunity to perform experiments at the Z6 experimental area. I am also obliged to entire plasma physics group at GSI, Strahlen und Kernphysik group at TU Darmstad for excellent working atmosphere and always offering every sort of assistance.

I would like to thank Dr. N. A. Tahir for his guidance and motivation to complete the studies.

I acknowledge the financial support from Higher Education Commission (HEC) Pakistan and Deutscher Akademischer Austausch Dienst (DAAD).

I would like to take this opportunity to express gratitude to my parents for their ever-lasting guidance and kind wishes for me. Last but not least I would like to thank my wife Sobia Zahra and my daughter Roya Zahra for their support and patience.

Curriculum Vitae

Name	Muhammad Imran
Born	10.12.1980 in Hafizabad (Pakistan)
Nationality	Pakistani
Marital status	Married

Education

March 1992-1994	Secondary School Certificate (S. S. C.), Government High School 1, Hafizabad (Pakistan)
September 1994-1996	Higher Secondary School Certificate (H. S. S. C.), Government Islamia College Civil Lines, Lahore (Pakistan)
November 1996-1999	Bachelors of Science (B. Sc) in Maths and Physics, The University of Punjab Lahore (Pakistan)
September 2000-2002	Masters in Physics (M. Sc), University of Engineering and Technology Lahore (Pakistan)
March 2003-2006	Masters in Philosophy (M. Phil.), University of Engineering and Technology, Lahore (Pakistan)
April 2007	Doctoral student at Institut für Kernphysik, Technische Universität Darmstadt, (Germany)

Erklärung zur Dissertation

Hiermit versichere ich, die vorliegende Dissertation ohne Hilfe Dritter nur mit den angegebenen Quellen und Hilfsmitteln angefertigt zu haben. Alle Stellen, die aus Quellen entnommen wurden, sind als solche kenntlich gemacht. Diese Arbeit hat in gleicher oder ähnlicher Form noch keiner Prüfungsbehörde vorgelegen.

Darmstadt, den 10. Dezember 2010

(Muhammad Imran)